Sinusoidal Anti-coupling Symmetric Strip Waveguides on a Silicon-on-insulator Platform

by

Fan Zhang

B.A.Sc., The University of British Columbia, 2012

A THESIS SUBMITTED IN PARTIAL FULFILLMENT OF
THE REQUIREMENTS FOR THE DEGREE OF

MASTER OF APPLIED SCIENCE

in

The Faculty of Graduate and Postdoctoral Studies

(Electrical and Computer Engineering)

THE UNIVERSITY OF BRITISH COLUMBIA

(Vancouver)

August 2017

Abstract

Sinusoidal anti-coupling (AC) symmetric waveguides provide a means to design dense waveguide arrays that have minimal inter-waveguide crosstalk for high-density integration of photonic circuits. Also, the polarization sensitivity of sinusoidal AC symmetric waveguides and the reduction of wavelength dependence that is achieved by the sinusoidal waveguides can be used to design broadband polarization beam splitters (PBSs) for polarization diversity systems. In this thesis, I demonstrate the use of sinusoidal bends to suppress the optical power exchange between pairs of symmetric strip waveguides for both transverse-electric (TE) and transverse-magnetic (TM) modes as well as to separate the TE and TM modes into two output symmetric strip waveguides on a silicon-on-insulator platform. I design, model, simulate, and analyze sinusoidal AC symmetric waveguide pairs for both the TE and TM modes. Then, based on the TE sinusoidal AC waveguide structure, I design, simulate, and analyze a PBS using a symmetric directional coupler (DC) with sinusoidal bends. I also compare the modal dispersions of the sinusoidally-bent symmetric DC, which is used in the PBS, with the modal dispersions of an equivalent straight symmetric DC. I measure the fabricated test devices and evaluate their performances.

The TE sinusoidal AC device, which has a gap width of 200 nm, has an average crosstalk suppression ratio (SR) of 38.2 dB, and the TM sinusoidal

AC device, which has a gap width of 600 nm, has an average crosstalk SR of 34.9 dB over an operational bandwidth of 35 nm. The PBS has a small coupler length of 8.55 μm, has average extinction ratios of 12.0 dB for the TE mode and of 20.1 dB for the TM mode, and has average polarization isolations of 20.6 dB for the through port (the TE mode over the TM mode) and of 11.5 dB for the cross port (the TM mode over the TE mode) over a broad operational bandwidth of 100 nm. All of my devices are easy to fabricate and compatible with complementary metal-oxide-semiconductor technologies.

Lay Summary

In modern communications systems, light is often used to carry information via optical waveguides in photonic circuits. When straight symmetric waveguides are placed near each other, light will transfer, or couple, between the waveguides. In this thesis, I present sinusoidal anti-coupling symmetric silicon waveguide pairs that eliminate this coupling. Without the coupling, the footprints of photonic circuits can be reduced.

There are two light propagation modes in the waveguides with rectangular cross-sections that are often used in photonic circuits: transverse-electric and transverse-magnetic modes. Sinusoidal anti-coupling symmetric waveguides can be used to either separate or combine these two types of modes. Hence, in this thesis, I also present a silicon polarization beam-splitter/combiner using sinusoidal anti-coupling symmetric waveguides. This device can be utilized to enhance the information-carrying capacity of optical communications systems.

Preface

I am the main author of a journal paper, "Compact broadband polarization beam splitter using a symmetric directional coupler with sinusoidal bends [1], and a conference paper, "Sinusoidal anti-coupling SOI strip waveguide" [2]. I presented a sinusoidal anti-coupling (AC) symmetric strip waveguide pair for transverse-electric mode and a polarization beam splitter (PBS) using a symmetric strip waveguide directional coupler (DC) with sinusoidal bends on an SOI platform.

I calculated the design parameters for my devices using an analytical model and a finite-difference eigenmode solver (MODE Solutions from Lumerical Solutions, Inc.). For the PBS, I also derived the modal dispersion to analyze the wavelength dependence of a sinusoidally-bent symmetric DC, which was used in the PBS. I optimized the design parameters for fabrication using a finite-difference time-domain solver (FDTD Solutions from Lumerical Solutions, Inc.). Then, I drew the test devices on mask layouts. In order to evaluate the performance of the TE sinusoidal AC device, I added a straight symmetric DC and a straight AC asymmetric waveguide pair, which had the same gap width and coupler length as the TE sinusoidal AC device, to the mask layouts. The test devices were fabricated using electron-beam lithography at the University of Washington. I measured the fabricated test devices using an automated probe station, which was developed by Han Yun, Jonas Flückiger, Charlie Lin, Stephen Lin, and Michael Caverley, in our lab at the University of British Columbia. Finally, I evaluated the performances of those devices using the simulation and measurement data.

In this thesis, Section 1.2.2 of Chapter 1, Sections 2.1, 2.3, 2.4 and 2.5 of Chapter 2, Section 3.5 of Chapter 3, Sections 4.1, 4.2, and 4.3.3 of Chapter 4, and Section 5.3 of Chapter 5 are based on the work in the paper [1]. Also in this thesis, Section 1.2.1 of Chapter 1, Sections 2.1 and 2.4 of Chapter 2, Section 3.3 of Chapter 3, and Sections 4.1, 4.2, and 4.3.1 of Chapter 4 are based on the work in the paper [2].

My supervisor, Dr. Nicolas A. F. Jaeger, provided me with essential guidance, advice, and support for my research and helped me write and edit my papers. Dr. Lukas Chrostowski provided me with valuable insights regarding design and fabrication issues and useful suggestions to help me improve my papers. My colleague, Han Yun, also helped me edit my papers.

Here is a copyright notice for the contents that are reproduced in this thesis with permissions from my papers [1, 2]:

Here is a list of my publications as the main author:

1. Fan Zhang, Han Yun, Yun Wang, Zeqin Lu, Lukas Chrostowski, and Nicolas A. F. Jaeger. Compact broadband polarization beam splitter using a symmetric directional coupler with sinusoidal bends. Optics Letters, 42(2):235-238, Optical Society of America, 2017.

2. Fan Zhang, Han Yun, Valentina Donzella, Zeqin Lu, Yun Wang, Zhitian Chen, Lukas Chrostowski, and Nicolas A. F. Jaeger. Sinusoidal

anti-coupling SOI strip waveguides. In CLEO: Science and Innovations, pages SM1I-7. Optical Society of America, 2015.

During my Master's studies, I participated in various research projects. In these projects, I worked with my colleagues to design, analyze, and measure various optical devices, including broadband couplers, photonic crystals, optical pulse shaping devices, polarization beam splitters, Bragg grating filters, and sub-wavelength grating couplers. A list of publications for the projects is given in Appendix B.

Table of Contents

Appendices

List of Tables

List of Figures

List of Abbreviations

AC	anti-coupling
CMOS	complementary metal-oxide-semiconductor
DC	directional coupler
ER	extinction ratio
E-Beam	electron-beam
FDE	finite-difference eigenmode
FDTD	finite-difference time-domain
IC	integrated circuit
PI	polarization isolation
PBS	polarization beam splitter
SEM	scanning-electron-microscope
SOI	silicon-on-insulator
SR	suppression ratio
SWGC	sub-wavelength grating coupler

TE transverse-electric

TM transverse-magnetic

1-D one-dimensional

2-D two-dimensional

3-D three-dimensional

Acknowledgements

I would like to thank my parents for encouraging me throughout my undergraduate and graduate studies. They are my role models who taught me to dream big and work hard. Thank you so much for always believing in me and supporting me.

I would like to express my sincere gratitude to my supervisor, Dr. Nicolas A. F. Jaeger, for guiding my research, suggesting my projects, and helping me write and edit my papers. I am very thankful to Dr. Lukas Chrostowski for providing help and advice regarding my projects and papers.

I greatly appreciate the help for my research from my current and former colleagues in the Electrical Engineering and Computer Engineering Department of University of British Columbia, in particular Drs Yun Wang, Xu Wang, Jonas Flückiger, Valentina Donzella, Miguel Ángel Guillén Torres, Wei Shi, Robert Boeck, Sahba Talebi Fard, and Mikael C. Rechtsman as well as Han Yun, Zeqin Lu, Zhitian Chen, Minglei Ma, Charlie Lin, Stephen Lin, and Michael Caverley.

I would like to acknowledge Natural Sciences and Engineering Research Council of Canada and CMC Microsystems for their financial support. I would like to acknowledge Han Yun, Jonas Flückiger, Charlie Lin, Stephen Lin, and Michael Caverley for the development of automated probe stations in our lab. I would like to acknowledge Richard J. Bojko and N. Shane

Patrick at the Washington Nanofabrication Facility at the University of Washington, a part of the National Nanotechnology Infrastructure Network supported by National Science Foundation, for the fabrication of my devices. I also would like to acknowledge Lumerical, Inc., MathWorks, Inc., and Mentor Graphics, Inc. for making their design software available to me.

Dedication

To my mother, Guozhen Liu, and to my father, Jianmin Zhang, I am very grateful for your unconditional love, continuous support, and hearty encouragement that help me fulfill my dreams, complete my studies, and overcome challenges in my life.

Chapter 1

Introduction

1.1 Silicon Photonics in Optical Communications

Silicon photonics continues to evolve and to have a huge impact on the advancement of optical communications technologies. Silicon has many unique attributes that make it a versatile material for both photonics and electronics. For example, silicon optical waveguides have a wide, low-loss transmission window within the infrared spectrum, specifically, from 1100 nm to 8600 nm according to Ref. [3]. Furthermore, silicon, the second most abundant element in the crust of the Earth, is a semiconductor that has been used by electronics industry for decades. Existing complementary metal-oxide-semiconductor (CMOS) design tools and fabrication processes can be used to build photonic integrated circuits (ICs) on silicon-on-insulator (SOI) platforms, and high quality SOI wafers are available at low prices. Moreover, high refractive index contrast between silicon waveguide cores and silicon dioxide or air claddings on an SOI platform allows compact waveguides and waveguide bends with small radii to have good optical confinement for single-mode operation and, therefore, SOI optical components can have small feature sizes and low propagation losses. As a result, the footprints of SOI ICs can be greatly reduced as compared to other photonic ICs, e.g., indium-phosphide-based ICs.

The integration of silicon photonic and microelectronic circuits is crucial for numerous applications of silicon photonics in optical communications. Using mature hybrid integration techniques, many leading semiconductor and telecommunications companies, such as Luxtera, Finisar, Cisco, and Intel, have introduced optical transceiver modules that are based on silicon photonics, with a wide range of data rates up to 200 Gbps, for optical interconnects in data centers according to Refs. [4–7]. In last few years, there have also been important technological breakthroughs for the monolithic integration of photonic and electronic circuits on SOI platforms. In 2015, a large-scale integration of silicon photonic and electronic circuits on a single chip was demonstrated using 45-nm CMOS fabrication processes in Ref. [8]. In 2016, a quantum dot laser, which was directly grown on a silicon substrate, was demonstrated using standard CMOS fabrication processes in Ref. [9]. In 2016, IBM demonstrated a multichannel 56 Gbps silicon photonic transmitter by integrating a silicon optical modulator and CMOS driver circuits on a single chip using 90-nm CMOS fabrication processes in Ref. [10]. The continuously advancing silicon photonics and microelectronics fabrication technologies lay the foundation for next generation optical communications systems with wide operational bandwidths and low power consumptions.

Fundamental building blocks of silicon photonics include passive components (such as ring resonators, multi-mode interference couplers, directional couplers, Bragg grating filters, and grating couplers) and active components (such as modulators, photodetectors, and lasers). There are numerous demonstrations of these photonic devices in Refs. [11–19] on SOI platforms within standard telecommunications bands, from 1260 nm to 1675 nm.

1.2 Thesis Motivation and Objective

1.2.1 Sinusoidal Anti-coupling Symmetric Waveguides

SOI platforms allow us to integrate large-scale photonic circuits and realize various functionalities on a single chip. In SOI ICs, we use routing waveguides to connect photonic components. Nevertheless, we need to keep routing waveguides far apart to minimize undesired inter-waveguide crosstalk. However, the use of large gaps between routing waveguides can increase the footprints of SOI photonic circuits and limit the number of devices that can be integrated on a chip.

In order to use on-chip real estate more efficiently, we can design special waveguide structures to suppress inter-waveguide crosstalk (see Ref. [2]). Stefano proposed to suppress the crosstalk using sinusoidal symmetric waveguides on a titanium lithium-niobate platform in Refs. [20, 21] and demonstrated sinusoidal anti-coupling (AC) symmetric waveguides on an erbium-ytterbium phosphate platform in Ref. [22]. Nicolas demonstrated a Mach-Zehnder modulator using sinusoidal AC symmetric waveguides on a titanium lithium-niobate platform in Ref. [23]. As an alternative AC waveguide structure, straight asymmetric waveguides were demonstrated on SOI platforms in Refs. [24, 25].

In this thesis, I present sinusoidal AC symmetric waveguide pairs on an SOI platform for transverse-electric (TE) or transverse-magnetic (TM) modes, each with design, model, simulation, analysis, and demonstration. The demonstrated devices provide large crosstalk suppressions for both the TE and TM modes over the entire C-band. They are also compatible with CMOS fabrication processes and easy to fabricate. Therefore, they can be used to design high-density routing waveguides in photonic circuits.

1.2.2 Polarization Beam Splitter Using a Symmetric Directional Coupler with Sinusoidal Bends

In optical communications systems based on silicon photonics, light is usually transmitted between photonic chips via optical fibres (see Ref. [1]). However, the polarization states of optical signals at the outputs of optical fibres can change randomly according to Ref. [26]. Due to geometric birefringence, optical signals in SOI waveguides are prone to undesired polarization-dependent modal dispersion, central wavelength shift, and phase shift according to Refs. [27–29]. Polarization beam splitters (PBSs) are essential components in polarization management systems to solve the problems caused by the polarization dependence of SOI waveguides (see Ref. [1]).

There are many different configurations of PBSs that have been demonstrated on SOI platforms, including arrayed waveguide gratings, directional couplers (DCs), Mach-Zehnder interferometers, photonic crystals, two-mode interference couplers, and multi-mode interference couplers in Refs. [28, 30–40]. Zeqin demonstrated a broadband PBS using point-symmetric cascaded couplers in Ref. [40], but it has a relatively long coupler length of 87.4 μm. Jian demonstrated a compact PBS using an asymmetric DC in Ref. [36], but it has strong wavelength dependencies for both the TE and TM modes.

In this thesis, I present the design, simulation, analysis, and demonstration of a PBS using a symmetric DC with sinusoidal bends on an SOI platform. The device has a small coupler length of 8.55 μm and a broad operational bandwidth for both TE operation and TM operation. It is also compatible with CMOS fabrication processes and easy to fabricate. Therefore, it can be used for polarization management in optical communications systems.

1.3 Thesis Organization

This thesis consists of the following five chapters and one appendix:

In Chapter 1, I review the development of silicon photonics in optical communications. I also describe the motivation, objective, and organization of this thesis.

In Chapter 2, I present the design and model of a straight symmetric DC and a sinusoidally-bent symmetric DC. I also derive the modal dispersion between the supermodes of the sinusoidally-bent symmetric DC in order to compare its wavelength dependence with an equivalent straight symmetric DC (which has the same gap width and coupler length as the bent symmetric DC).

In Chapter 3, I present the simulation and analysis of a single straight waveguide, straight symmetric DCs, sinusoidal AC symmetric waveguide pairs, and a PBS using a symmetric DC with sinusoidal bends for TE and/or TM operation on an SOI platform. I compare the wavelength dependencies of the sinusoidally-bent symmetric DC, which is used in the PBS, with an equivalent straight symmetric DC for the TE and TM modes.

In Chapter 4, I present the fabrication, measurement, and demonstration of sinusoidal AC symmetric waveguide pairs and a PBS using a symmetric DC with sinusoidal bends for TE and/or TM operation on an SOI platform. I compare the sinusoidal AC symmetric waveguide pairs with the straight symmetric DCs and straight AC asymmetric waveguide pairs (which have the same gap widths and couplers lengths as the sinusoidal AC devices), each for the TE and TM modes. I also evaluate the performance of the PBS.

In Chapter 5, I summarize and conclude my thesis. I also provide suggestions for future research on sinusoidal symmetric SOI waveguides.

In Appendix A, I present a derivation of the propagation constant difference of a sinusoidally-bent symmetric DC in terms of the propagation constant difference of an equivalent straight symmetric DC.

Chapter 2

Design and Theory

In this chapter, I design and model a symmetric DC with sinusoidal bends for TE and/or TM operation on an SOI platform. I describe the waveguide structures and the principles of operation for my devices. I derive an analytical model of a straight symmetric DC and use the analytical model to obtain the optical transmissions of symmetric DCs as well as obtaining the formulas of essential design parameters for my devices. I also derive the modal dispersions between the supermodes of a symmetric DC in order to study the wavelength dependence of the device.

2.1 Design Overview

As shown in Fig. 2.1, each of my devices consists of a pair of parallel symmetric strip waveguides that are separated by a gap of width, G, and have the same width, W, and height, H. Since a sinusoidally-bent symmetric waveguide pair has the same cross-sectional structure as a straight symmetric DC, I can also refer to it as a symmetric DC with sinusoidal bends. Each sinusoidal bend is defined as a function of z, $f_x(z)$ (see Fig. 2.2), as in Ref. [1]:

$$f_x(z) = A \cos\left(\frac{2\pi}{\Lambda} z\right), \tag{2.1}$$

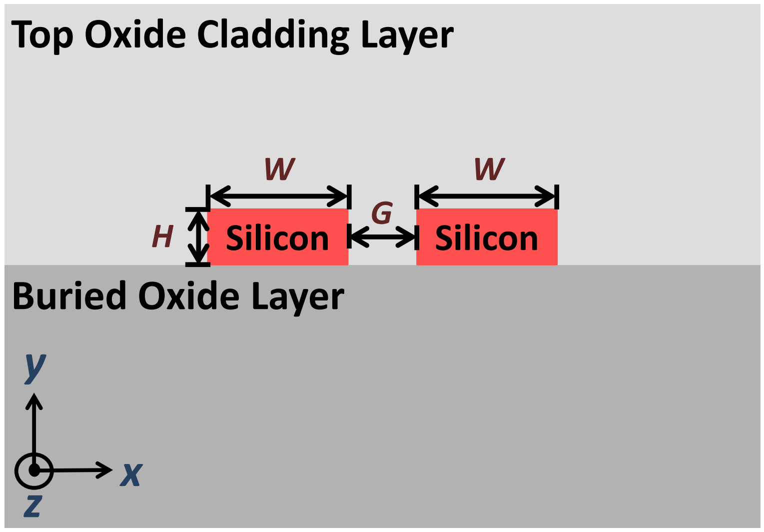

Figure 2.1: Cross-sectional view of a pair of parallel symmetric strip waveguides on an SOI platform. Adapted with permission from Ref. [1], ©2017 Optical Society of America.

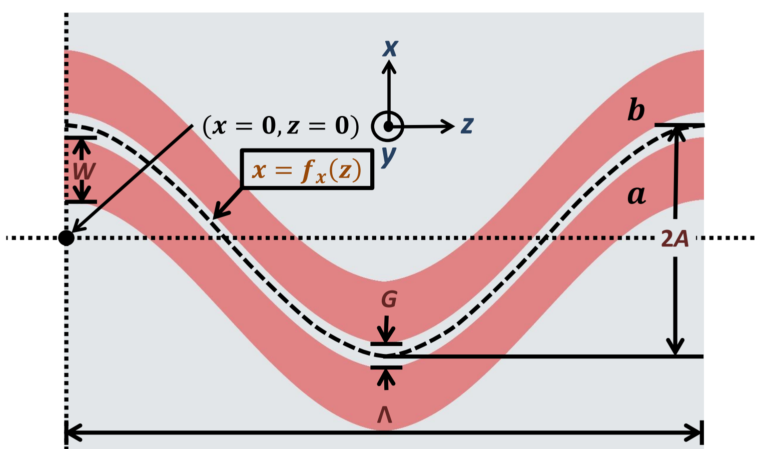

Figure 2.2: Top view of a full period of a symmetric DC with sinusoidal bends. Adapted with permission from Ref. [1], ©2017 Optical Society of America.

where A and Λ are the amplitude and period of a sinusoid. The choices of Gs depend on design requirements and constraints.

The use of sinusoidal bends in parallel symmetric waveguides can suppress the optical power exchange between the waveguides for either TE or TM operation. Therefore, I can design sinusoidal AC symmetric waveguide pairs. Based on this idea, I have demonstrated a sinusoidal AC symmetric SOI strip waveguide pair for TE operation in Ref. [2], and I demonstrate a sinusoidal AC symmetric SOI strip waveguide pair for TM operation in this thesis. Compact routing waveguides and dense waveguide buses are two of the potential applications of sinusoidal AC symmetric waveguides.

Sinusoidal AC symmetric waveguides can also be used to design a PBS. In a sinusoidal AC symmetric waveguide pair that is designed for TE operation, optical power exchange between the waveguides still occurs for TM operation. Such a device can be regarded as an "anti-coupler" for TE operation and as a coupler for TM operation. The device can have a small gap width and a small coupler length. The sinusoidal bends can also allow a symmetric DC to have broadband performances for both TE operation and TM operation. Based on these ideas, I have designed a compact broadband PBS using a symmetric DC with sinusoidal bends for both TE operation and TM operation on an SOI platform in Ref. [1].

2.2 Analytical Model of a Straight Symmetric DC

A straight symmetric DC consists of a pair of parallel identical waveguides which are close to each other. According to Refs. [41, 42], the device can be analyzed in terms of even (symmetric) and odd (anti-symmetric) supermodes. When light is injected into one of the waveguide cores, it excites one even supermode and one odd supermode in the two-waveguide structure. The supermodes propagating in the DC each travel at their own speeds. The difference in their speeds causes the optical power to oscillate from one waveguide core to the other along the length of the device, L.

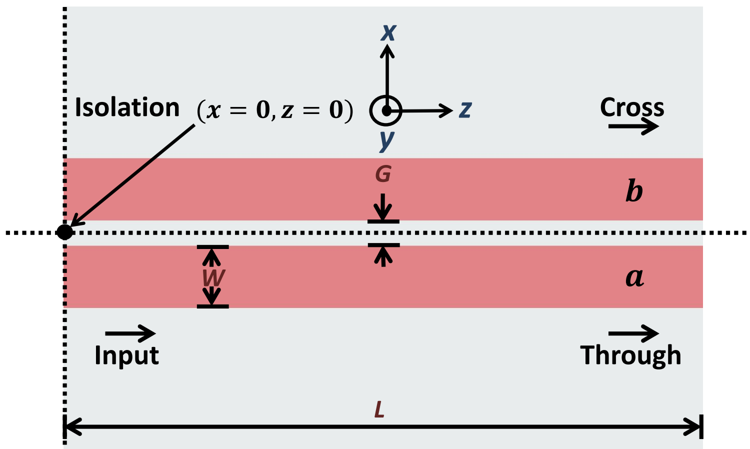

Figure 2.3: Top view of a straight symmetric DC.

As shown in Fig. 2.3, I have labelled the waveguide cores $\boldsymbol{a}$ and $\boldsymbol{b}$ and the input, isolation, through, and cross ports, which I will use to model a straight symmetric DC. I assume that the DC is lossless, that the electromagnetic fields propagating in the device are time-harmonic, and that the transverse field distributions for the even and odd supermodes (in the $x - y$ plane) are invariant along the propagation direction (along the z axis). Based on these assumptions, the electric field distributions for the even and odd supermodes in the device, $\Psi_e(x, y, z)$ and $\Psi_o(x, y, z)$, can be represented in terms of their respective transverse field amplitudes at $z = 0$, A_e and A_o, their respective normalized transverse field distributions at $z = 0$, $\psi_e(x, y)$ and $\psi_o(x, y)$, and their respective propagation constants, β_e and β_o. I can use

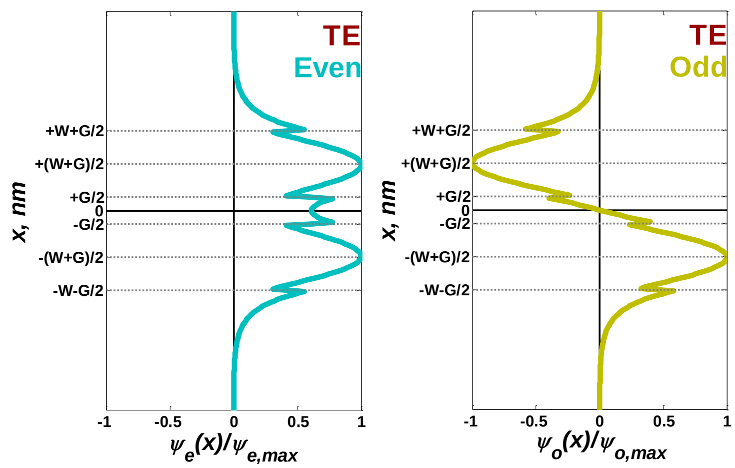

Figure 2.4: 1-D normalized transverse field distributions for the even TE supermode (left) and odd TE supermode (right), $\psi_e(x)$ and $\psi_o(x)$, over their respective maximum values, $\psi_{e,max}$ and $\psi_{o,max}$.

the effective index method to collapse the two-dimensional (2-D) transverse field distribution into an one-dimensional (1-D) one, so that $\psi_e(x, y)$ and $\psi_o(x, y)$ become $\psi_e(x)$ and $\psi_o(x)$ (see Figs. 2.4 and 2.5), respectively, and, as a result, $\Psi_e(x, y, z)$ and $\Psi_o(x, y, z)$ become $\Psi_e(x, z)$ and $\Psi_o(x, z)$, also respectively. Therefore, when light is injected into only waveguide core $\boldsymbol{a}$, $\Psi_e(x, z)$ can be expressed as:

$$\Psi_e(x, z) = A_e \psi_e(x) e^{-j\beta_e z}, \tag{2.2}$$

and $\Psi_o(x, z)$ can also be expressed as:

$$\Psi_o(x, z) = A_o \psi_o(x) e^{-j\beta_o z}, \tag{2.3}$$

where $\psi_e(x)$ and $\psi_o(x)$ are normalized such that $\int_{-\infty}^{+\infty} |\psi_e(x)|^2 dx + \int_{-\infty}^{+\infty} |\psi_o(x)|^2 dx = 1$. As the superposition of the even and odd supermodes, the 2-D

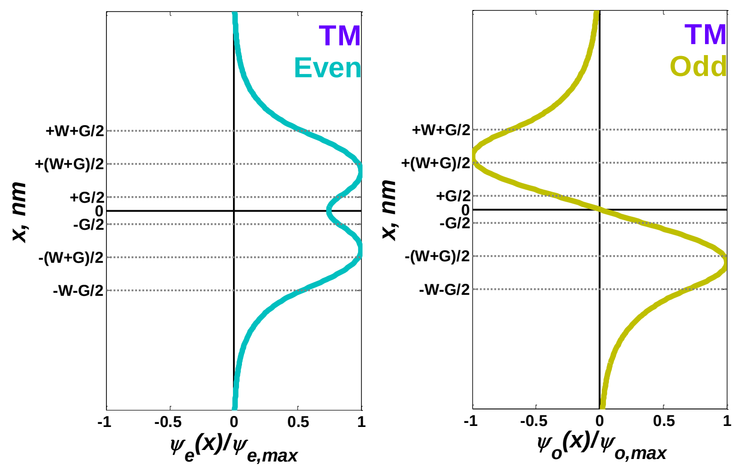

Figure 2.5: 1-D normalized transverse field distributions for the even TM supermode (left) and odd TM supermode (right), $\psi_e(x)$ and $\psi_o(x)$, over their respective maximum values, $\psi_{e,max}$ and $\psi_{o,max}$.

electric field distribution of a straight symmetric DC, $\Psi_{DC}(x, z)$, can be obtained as:

$$\Psi_{DC}(x, z) = \Psi_e(x, z) + \Psi_o(x, z) = A_e \psi_e(x) e^{-j\beta_e z} + A_o \psi_o(x) e^{-j\beta_o z}, \quad (2.4)$$

which shows the overall interference between the even and odd supermodes along the device.

In order to study the local interference for the even and odd supermodes in waveguide cores $\boldsymbol{a}$ and $\boldsymbol{b}$, I will also analyze the local normal modes. According to Refs. [21, 41, 42], the model of the DC that is based on the supermodes and the one that is based on the coupled modes are correlated, so that I can express the 2-D electric field distributions for local normal modes in waveguide cores $\boldsymbol{a}$ and $\boldsymbol{b}$, $\Psi_a(x, z)$ and $\Psi_b(x, z)$, in terms of their respective z-dependent transverse field amplitudes, $A_a(z)$ and $A_b(z)$, their

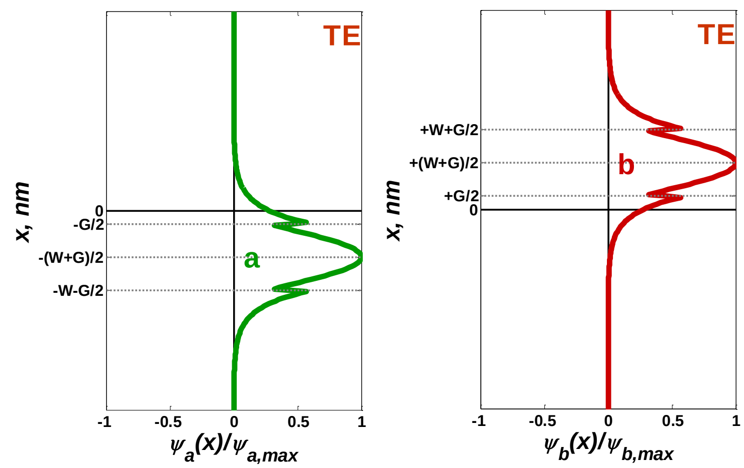

Figure 2.6: 1-D normalized transverse field distributions for the TE local normal modes in waveguide cores $\boldsymbol{a}$ (left) and waveguide core $\boldsymbol{b}$ (right), $\psi_a(x)$ and $\psi_b(x)$, over their respective maximum values, $\psi_{a,max}$ and $\psi_{b,max}$.

respective 1-D normalized transverse field distributions, $\psi_a(x)$ and $\psi_b(x)$ (see Figs. 2.6 and 2.7), and their respective propagation constants, β_a and β_b. Therefore, $\Psi_a(x,z)$ can be expressed as:

$$\Psi_a(x,z) = A_a(z)\psi_a(x)e^{-j\beta_a z}, \tag{2.5}$$

and $\Psi_b(x,z)$, can be also be expressed as:

$$\Psi_b(x,z) = A_b(z)\psi_b(x)e^{-j\beta_b z}. \tag{2.6}$$

where $\psi_a(x)$ is normalized such that $\int_{-\infty}^{+\infty} |\psi_a(x)|^2 dx = 1$, and $\psi_b(x)$ is normalized such that $\int_{-\infty}^{+\infty} |\psi_b(x)|^2 dx = 1$. Here, referring to Eq. 2.4, $\Psi_{DC}(x,z)$ can be rewritten as:

$$\Psi_{DC}(x,z) = \left[A_e\psi_e(x)e^{-j\frac{\Delta\beta}{2}z} + A_o\psi_o(x)e^{j\frac{\Delta\beta}{2}z}\right]e^{-j\frac{\Sigma\beta}{2}z}, \tag{2.7}$$

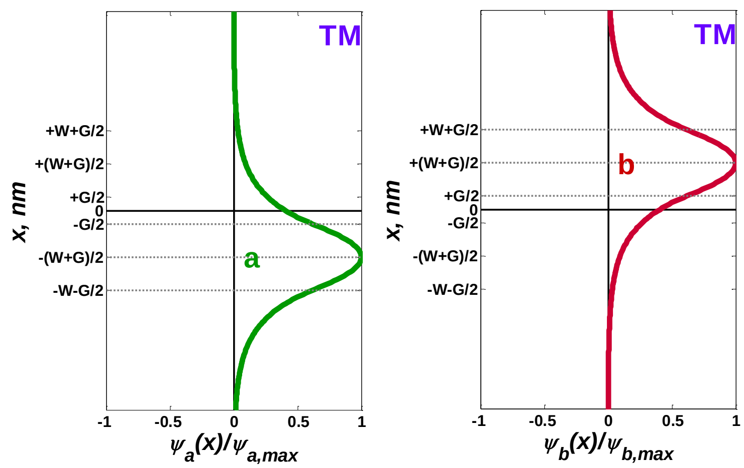

Figure 2.7: 1-D normalized transverse field distributions for the TM local normal modes in waveguide core ***a*** (left) and waveguide core ***b*** (right), $\psi_a(x)$ and $\psi_b(x)$, over their respective maximum values, $\psi_{a,max}$ and $\psi_{b,max}$.

where $\Delta\beta = \beta_e - \beta_o$ and $\Sigma\beta = \beta_e + \beta_o$ are the difference and the sum of β_e and β_o, respectively.

For an arbitrary integer, n, when $\Delta\beta z = 2n\pi$, light is localized in waveguide core ***a***, $|A_a(z)|$ reaches its maximum magnitude, $A_{a,M}$, at $z = \frac{2n\pi}{\Delta\beta}$, and $\Psi_{DC}\left(x, \frac{2n\pi}{\Delta\beta}\right) = \pm[A_e\psi_e(x) + A_o\psi_o(x)]e^{-j\frac{n\pi}{\Delta\beta}\Sigma\beta}$. Thus, referring to Eqs. 2.5 and 2.7, the correlation among $\psi_a(x)$, $\psi_e(x)$, and $\psi_o(x)$ at $z = \frac{2n\pi}{\Delta\beta}$ can be given as:

$$A_{a,M}\psi_a(x) = A_e\psi_e(x) + A_o\psi_o(x), \tag{2.8}$$

and, when $\Delta\beta z = (2n+1)\pi$, light is localized in waveguide core ***b***, $|A_b(z)|$ reaches its maximum magnitude, $A_{b,M}$, at $z = \frac{(2n+1)\pi}{\Delta\beta}$, and $\Psi_{DC}\left[x, \frac{(2n+1)\pi}{\Delta\beta}\right] = \pm(-j)[A_e\psi_e(x) - A_o\psi_o(x)]e^{-j\frac{(n+\frac{1}{2})\pi}{\Delta\beta}\Sigma\beta}$. Thus, referring to Eqs. 2.6 and 2.7, the correlation among $\psi_b(x)$, $\psi_e(x)$, and $\psi_o(x)$

at $z = \frac{(2n+1)\pi}{\Delta\beta}$ can be given as:

$$A_{b,M}\psi_b(x) = A_e\psi_e(x) - A_o\psi_o(x). \tag{2.9}$$

Then, adding Eqs. 2.8 and 2.9, $\psi_e(x)$ can be expressed, in terms of $\psi_a(x)$ and $\psi_b(x)$, as:

$$\psi_e(x) = \frac{A_{a,M}\psi_a(x) + A_{b,M}\psi_b(x)}{2A_e}, \tag{2.10}$$

and, subtracting Eq. 2.9 from Eq. 2.8, $\psi_o(x)$ can also be expressed, in terms of $\psi_a(x)$ and $\psi_b(x)$, as:

$$\psi_o(x) = \frac{A_{a,M}\psi_a(x) - A_{b,M}\psi_b(x)}{2A_o}. \tag{2.11}$$

Subsequently, substituting Eqs. 2.10 and 2.11 into Eq. 2.7, $\Psi_{DC}(x,z)$ can be rewritten, in terms of $\psi_a(x)$ and $\psi_b(x)$, as:

$$\Psi_{DC}(x,z) = \left[A_{a,max}\left(\frac{e^{-j\frac{\Delta\beta}{2}z} + e^{j\frac{\Delta\beta}{2}z}}{2}\right)\psi_a(x) + A_{b,max}\left(\frac{e^{-j\frac{\Delta\beta}{2}z} - e^{j\frac{\Delta\beta}{2}z}}{2}\right)\psi_b(x)\right]e^{-j\frac{\Sigma\beta}{2}z}. \tag{2.12}$$

Since, in a lossless symmetric DC, $A_{a,M} = A_{b,M} = A_M$, β_{wg} is the propagation constant of a single straight strip waveguide with the cross-sectional dimensions (W and H), and $\frac{\Sigma\beta}{2} \approx \beta_a = \beta_b = \beta_{wg}$, referring to Eq. 2.12, $\Psi_a(x,z)$ can be given as:

$$\Psi_a(x,z) = A_M\left(\frac{e^{-j\frac{\Delta\beta}{2}z} + e^{j\frac{\Delta\beta}{2}z}}{2}\right)\psi_a(x)e^{-j\frac{\Sigma\beta}{2}z} = A_M\cos\left(\frac{\Delta\beta}{2}z\right)\psi_a(x)e^{-j\beta_{wg}z}, \tag{2.13}$$

and, also referring to Eq. 2.12, $\Psi_b(x,z)$ can be given as:

$$\Psi_b(x,z) = A_M\left(\frac{e^{-j\frac{\Delta\beta}{2}z} - e^{j\frac{\Delta\beta}{2}z}}{2}\right)\psi_b(x)e^{-j\frac{\Sigma\beta}{2}z} = -jA_M\sin\left(\frac{\Delta\beta}{2}z\right)\psi_b(x)e^{-j\beta_{wg}z}. \tag{2.14}$$

From now on, the subscript, wg, is used to indicate that a particular variable is related to a single straight waveguide. Hence, referring to Eqs. 2.5 and

2.13, $A_a(z)$ can be represented as:

$$A_a(z) = A_M \cos\left(\frac{\Delta\beta}{2}z\right), \tag{2.15}$$

and, referring to Eqs. 2.6 and 2.14, $A_b(z)$ can also be represented as:

$$A_b(z) = -jA_M \cos\left(\frac{\Delta\beta}{2}z\right). \tag{2.16}$$

Subsequently, referring to Eq. 2.13, the 1-D local electric field distributions at the input port, $\Psi_{input}(x)$, in waveguide core $\boldsymbol{a}$ at $z = 0$ can be solved as:

$$\Psi_{input}(x) = \Psi_a(x, 0) = A_M \psi_a(x), \tag{2.17}$$

referring to Eq. 2.14, the 1-D local electric field distribution at the isolation port, $\Psi_{isolation}(x)$, in waveguide core $\boldsymbol{b}$ at $z = 0$ can be solved as:

$$\Psi_{isolation}(x) = \Psi_b(x, 0) = 0, \tag{2.18}$$

referring to Eq. 2.13, the 1-D local electric field distribution at the through port, $\Psi_{through}(x)$, in waveguide core $\boldsymbol{a}$ at $z = L$ can be solved as:

$$\Psi_{through}(x) = \Psi_a(x, L) = A_M \cos\left(\frac{\Delta\beta}{2}L\right)\psi_a(x)e^{-j\beta_{wg}L}, \tag{2.19}$$

and, referring to Eq. 2.14, the 1-D local electric field distribution at the cross port, $\Psi_{cross}(x)$, in waveguide core $\boldsymbol{b}$ at $z = L$ can be solved as:

$$\Psi_{cross}(x) = \Psi_b(x, L) = -jA_M \sin\left(\frac{\Delta\beta}{2}L\right)\psi_b(x)e^{-j\beta_{wg}L}. \tag{2.20}$$

As the value of L varies, $\Psi_{through}(x, z)$ and $\Psi_{cross}(x, z)$ change sinusoidally in the waveguide cores.

2.3 Optical Transmissions of a Symmetric DC

Now, referring to Eqs. 2.17 and 2.19, the optical transmission to the through port of a symmetric DC, $T_{through}$, can be obtained as in Ref. [1]:

$$T_{through} = \frac{P_{through}}{P_{input}} \propto \frac{\int_{-\infty}^{+\infty} \Psi_{through}(x)\Psi^*_{through}(x)dx}{\int_{-\infty}^{+\infty} \Psi_{input}(x)\Psi^*_{input}(x)dx} = cos^2\left(\frac{\Delta\beta}{2}L\right), \tag{2.21}$$

and, referring to Eqs. 2.17 and 2.20, the optical transmission to the cross port of the DC, T_{cross}, can also be obtained as in Ref. [1]:

$$T_{cross} = \frac{P_{cross}}{P_{input}} \propto \frac{\int_{-\infty}^{+\infty} \Psi_{cross}(x)\Psi^*_{cross}(x)dx}{\int_{-\infty}^{+\infty} \Psi_{input}(x)\Psi^*_{input}(x)dx} = sin^2\left(\frac{\Delta\beta}{2}L\right), \tag{2.22}$$

where P_{input}, $P_{through}$, and P_{cross} are the optical powers at the input, through, and cross ports of the device, respectively. When light is injected into only one waveguide of the device, referring to Eq. 2.22, the smallest value of cross-over length that allows the maximum optical power transfer to an adjacent waveguide, $L_{c,min}$, at a given wavelength in vacuum, λ_0, can be given as:

$$L_{c,min} = \frac{\pi}{\Delta\beta}. \tag{2.23}$$

I will use Eq. 2.23 to calculate the $L_{c,min}$ of a straight symmetric DC for either TE or TM operation.

2.4 Sinusoidal AC Bends for a Symmetric Waveguide Pair

According to Refs. [20, 21, 43], the $\Delta\beta$ of a sinusoidally-bent symmetric DC, $\Delta\beta_{bent}$, can be given (see Appendix A) as in Ref. [1]:

$$\Delta\beta_{bent} \cong \Delta\beta_{straight} J_0\left[\frac{2\pi A(W+G)}{\Lambda}\beta_{wg}\right], \tag{2.24}$$

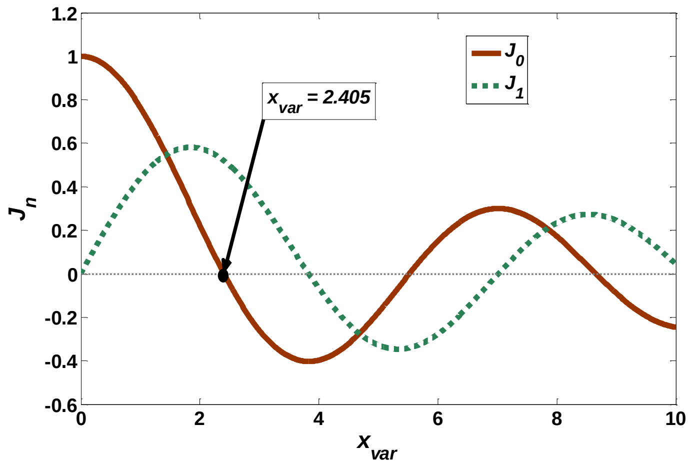

Figure 2.8: Bessel functions of the first kind of orders 0 and 1 with respect to a variable, x_{var}, ranging from 0 to 10.

where J_0 is the Bessel function of the first kind of order 0 (see Fig. 2.8). When W, H, G, Λ, and β_{wg} have been determined, I can find a value of A to obtain the first positive root of J_0 and to set the $\Delta\beta_{bent}$ and T_{cross} of the sinusoidally-bent symmetric DC to be zero (see Refs. [1, 2]). As shown in Fig. 2.8, the value of this root is approximately 2.405 and, therefore, the smallest value of A, A_{min}, that can suppress the optical power exchange between the sinusoidal waveguides can be given as in Refs. [1, 2]:

$$A_{min} \cong \frac{2.405\Lambda}{2\pi(W+G)\beta_{wg}}. \tag{2.25}$$

Since the derivation of $\Delta\beta_{bent}$ does not depend on mode type (either the TE or TM mode), Eqs. 2.24 and 2.25 can be used with either mode type. Thus, I will use Eq. 2.25 to calculate the A_{min} of a sinusoidal AC symmetric waveguide pair for either TE or TM operation. I will also use Eq. 2.24 to analyze bent and straight symmetric DCs.

2.5 Modal Dispersions between the Supermodes of Symmetric DCs

In order to study the wavelength dependence of a symmetric DC with sinusoidal bends, I will derive the modal dispersions between the even and odd supermodes of a symmetric DC. The phase velocity for the even supermode, $v_{p,e}$, can be defined as:

$$v_{p,e} = \frac{2\pi c}{\lambda_0 \beta_e}, \tag{2.26}$$

the phase velocity for the odd supermode, $v_{p,o}$, can also be defined as:

$$v_{p,o} = \frac{2\pi c}{\lambda_0 \beta_o}, \tag{2.27}$$

where $c = 299.8$ μm/ps is the speed of light in vacuum. The arrival time for the even supermode, τ_e, can be defined as:

$$\tau_e = \frac{L}{v_{p,e}}, \tag{2.28}$$

and the arrival time for the odd supermode, τ_o, can also be defined as:

$$\tau_o = \frac{L}{v_{p,o}}. \tag{2.29}$$

Then, substituting Eqs. 2.26 and 2.27 into Eqs. 2.28 and 2.29, respectively, I can write the difference between τ_o and τ_e, $\Delta\tau$, as in Ref. [1]:

$$\Delta\tau = \tau_o - \tau_e = \frac{-L\lambda_0}{2\pi c}\Delta\beta, \tag{2.30}$$

and, therefore, I can obtain the modal dispersion of a symmetric DC, $\mathbb{D}$, as in Ref. [1]:

$$\mathbb{D} = \frac{1}{L}\frac{d\Delta\tau}{d\lambda_0} = \frac{-1}{2\pi c}\left(\Delta\beta + \lambda_0 \frac{d\Delta\beta}{d\lambda_0}\right). \tag{2.31}$$

Subsequently, the $\mathbb{D}$ of a straight symmetric DC, $\mathbb{D}_{straight}$, can be given as:

$$\mathbb{D}_{straight} = \frac{-1}{2\pi c}\left(\Delta\beta_{straight} + \lambda_0 \frac{d\Delta\beta_{straight}}{d\lambda_0}\right), \tag{2.32}$$

and the $\mathbb{D}$ of a sinusoidally-bent symmetric DC, $\mathbb{D}_{bent}$, can also be given as:

$$\mathbb{D}_{bent} = \frac{-1}{2\pi c}\left(\Delta\beta_{bent} + \lambda_0 \frac{d\Delta\beta_{bent}}{d\lambda_0}\right). \tag{2.33}$$

Hence, substituting Eq. 2.24 into Eq. 2.33, I can rewrite $\mathbb{D}_{bent}$, in terms of $\Delta\beta_{straight}$, as:

$$\mathbb{D}_{bent} = \frac{-1}{2\pi c}\left[\left(\Delta\beta_{straight}+\lambda_0 \frac{d\Delta\beta_{straight}}{d\lambda_0}\right) J_0\Big(K\beta_{wg}\Big)+\left(\frac{2\pi}{\lambda_0}K n_{g,wg}\right)\Delta\beta_{straight} J_1\Big(K\beta_{wg}\Big)\right], \tag{2.34}$$

where $K = \frac{2\pi A(W+G)}{\Lambda}$, J_1 is the Bessel function of the first kind of order 1 (see Fig. 2.8), and $n_{g,wg}$ is the group index of a straight strip waveguide with the cross-sectional dimensions (W and H). Then, referring to Eqs. 2.32 and 2.34, I can express the absolute value of the ratio between $\mathbb{D}_{bent}$ and $\mathbb{D}_{straight}$ as in Ref. [1]:

$$\left|\frac{\mathbb{D}_{bent}}{\mathbb{D}_{straight}}\right| = J_0\Big(K\beta_{wg}\Big) + \frac{\left(\frac{2\pi}{\lambda_0}K n_{g,wg}\right)\Delta\beta_{straight} J_1\Big(K\beta_{wg}\Big)}{\Delta\beta_{straight} + \lambda_0 \frac{d\Delta\beta_{straight}}{d\lambda_0}}. \tag{2.35}$$

I will use Eq. 2.35 to calculate the $\left|\frac{\mathbb{D}_{bent}}{\mathbb{D}_{straight}}\right|$ at λ_0 and use the result to evaluate the wavelength dependency of a sinusoidally-bent symmetric DC as compared to an equivalent straight symmetric DC, which has the same W, H, G and L, for either the TE or TM mode.

2.6 Summary

In this chapter, the design and modelling methods for a straight symmetric DC and for a sinusoidally-bent symmetric DC were presented. The modal dispersion was also derived to study the wavelength dependence of the sinusoidally-bent symmetric DC and the equivalent straight symmetric DC.

Chapter 3

Simulation and Analysis

In this chapter, I simulate and analyze a single straight waveguide, straight symmetric DCs, and sinusoidal AC symmetric waveguide pairs. All of my simulations and analyses are based on the assumption that an SOI platform is being used for those devices. Using a finite-difference eigemode (FDE) solver, I simulate a single straight waveguide for both the fundamental TE and TM modes and simulate straight symmetric waveguide pairs, which are separated by gaps of different widths, for both the TE and TM supermodes. Referring to the formulas which have been derived from the previous chapter, I calculate the design parameters of the straight symmetric DCs and sinusoidal AC waveguide pairs for both TE operation and TM operation. Using a finite-difference time-domain (FDTD) solver, I optimize the designs of straight symmetric DCs and sinusoidal AC symmetric waveguide pairs. Then, I optimize the design of a PBS using a symmetric DC with sinusoidal bends using the FDTD solver, in which the suppression of optical power exchange between the waveguides is optimal only for TE operation but not for TM operation. Subsequently, using the simulation data that have been collected, I analyze the wavelength dependencies of the sinusoidally-bent symmetric DC, which is used in the PBS, for both the TE and TM modes.

3.1 Simulation and Analysis Overview

Table 3.1: Simulation parameters.

Parameters	**Names**
λ_0, nm	Wavelength in vacuum
n_{eff}	Effective refractive index at λ_0
$n_{eff,wg}$	The n_{eff} of a single straight waveguide
$n_{eff,wg}^{TE}$	The $n_{eff,wg}$ for the fundamental TE mode
$n_{eff,wg}^{TM}$	The $n_{eff,wg}$ for the fundamental TM mode
$n_{eff,e}$	The n_{eff} of a pair of straight symmetric waveguides for the even supermode
$n_{eff,e}^{TE}$	The $n_{eff,e}$ for the TE supermode
$n_{eff,e}^{TM}$	The $n_{eff,e}$ for the TM supermode
$n_{eff,o}$	The n_{eff} of a pair of straight symmetric waveguides for the odd supermode
$n_{eff,o}^{TE}$	The $n_{eff,o}$ for the TE supermode
$n_{eff,o}^{TM}$	The $n_{eff,o}$ for the TM supermode

Both the FDE and FDTD solvers (MODE Solutions and FDTD Solutions, respectively, from Lumerical Solutions, Inc.) use the finite-difference method for simulation, the FDE solver simulates optical modes on a cross-section of a waveguide structure by solving Maxwell's equations on a 2-D planar mesh according to Ref. [44], and the FDTD solver simulates the propagation of optical modes in a waveguide structure by solving Maxwell's equations in a 3-D cuboidal mesh with respect to both space and time according to Ref. [45]. The ambient temperature in my simulations is assumed

Table 3.2: Analysis parameters.

Parameters	**Names**
n_g	Group index at λ_0
$n_{g,wg}$	The n_g of a single straight waveguide
$n_{g,wg}^{TE}$	The $n_{g,wg}$ for the fundamental TE mode
$n_{g,wg}^{TM}$	The $n_{g,wg}$ for the fundamental TM mode
β, nm^{-1}	Propagation constant at λ_0
β_{wg}, nm^{-1}	The β of a single straight waveguide
β_{wg}^{TE}, nm^{-1}	The β_{wg} for the fundamental TE mode
β_{wg}^{TM}, nm^{-1}	The β_{wg} for the fundamental TM mode
β_e, nm^{-1}	The β of a pair of straight symmetric waveguides for the even supermode
β_e^{TE}, nm^{-1}	The β_e for the TE supermode
β_e^{TM}, nm^{-1}	The β_e for the TM supermode
β_o, nm^{-1}	The β of a pair of straight symmetric waveguides for the odd supermode
β_o^{TE}, nm^{-1}	The β_o for the TE supermode
β_o^{TM}, nm^{-1}	The β_o for the TM supermode
$\mathbb{D}$, ps$\cdot\mu$m$^{-1}\cdot$nm^{-1}	Modal dispersion at λ_0
$\mathbb{D}_{straight}$, ps$\cdot\mu$m$^{-1}\cdot$nm^{-1}	The $\mathbb{D}$ of a straight symmetric DC
$\mathbb{D}_{straight}^{TE}$, ps$\cdot\mu$m$^{-1}\cdot$nm^{-1}	The $\mathbb{D}_{straight}$ for the TE mode
$\mathbb{D}_{straight}^{TM}$, ps$\cdot\mu$m$^{-1}\cdot$nm^{-1}	The $\mathbb{D}_{straight}$ for the TM mode
$\mathbb{D}_{bent}$, ps$\cdot\mu$m$^{-1}\cdot$nm^{-1}	The $\mathbb{D}$ of a sinusoidal symmetric DC
$\mathbb{D}_{bent}^{TE}$, ps$\cdot\mu$m$^{-1}\cdot$nm^{-1}	The $\mathbb{D}_{bent}$ for the TE mode
$\mathbb{D}_{bent}^{TM}$, ps$\cdot\mu$m$^{-1}\cdot$nm^{-1}	The $\mathbb{D}_{bent}$ for the TM mode

Table 3.3: Design parameters.

Parameters	**Names**
G, nm	Gap width
W, nm	Waveguide width
H, nm	Waveguide height
L, μm	Length of a device
$L_{c,min}$, μm	The smallest cross-over L of a straight symmetric DC that is optimized for the operation at λ_0
$L_{c,min}^{TE}$, μm	The $L_{c,min}$ for TE operation
$L_{c,min}^{TM}$, μm	The $L_{c,min}$ for TM operation
Λ, μm	Period of a sinusoid
A, nm	Amplitude of a sinusoid
A_{min}, nm	The smallest A of a sinusoidal AC symmetric waveguide pair that is optimized for the operation at λ_0
A_{min}^{TE}, nm	The A_{min} for TE operation
A_{min}^{TM}, nm	The A_{min} for TM operation

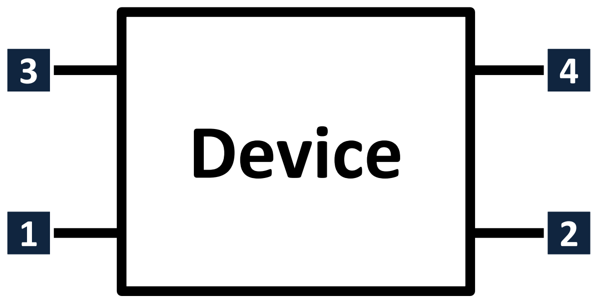

Figure 3.1: Port configuration in my simulations.

to be at 25 °C, and the central wavelength of operation for each device is chosen to be at 1550 nm. In Tables 3.1, 3.2, and 3.3, I list the parameters that will be used for my simulations, analyses, and designs. In my simulations, Ports 1, 2, 3, and 4 are defined as in Fig. 3.1 to indicate the inputs and outputs of each device. In my simulations, Port 1 is used as the default input port, unless another port is specified to be used as an input port.

3.2 Single Straight Waveguide

As shown in Fig. 3.2, the SOI strip waveguides, which are used in my devices, are surrounded by silicon dioxide, and all of these waveguides have the same cross-sectional dimensions, W = 500 nm and H = 220 nm, and support both single-mode TE operation and single-mode TM operation.

Using the FDE solver to simulate the cross-section of the single straight waveguide, I can obtain the $n_{eff,wg}$ for the waveguide structure. Hereafter,

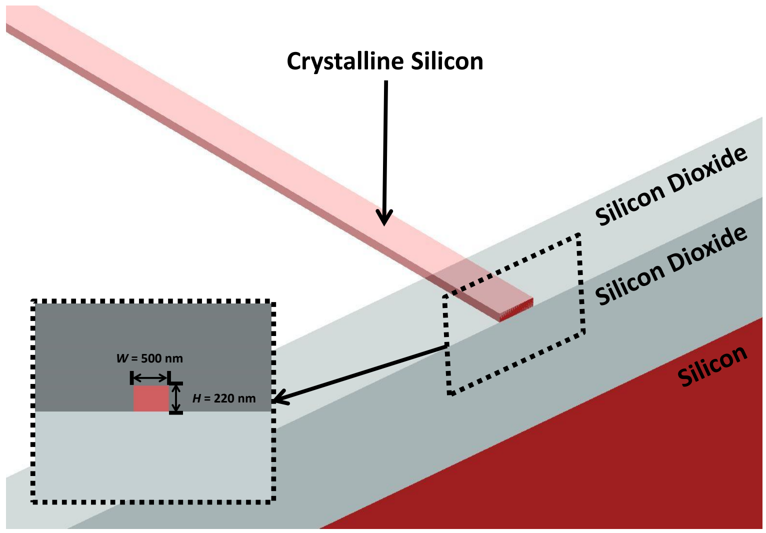

Figure 3.2: Perspective and cross-sectional views of a single straight waveguide, which has W = 500 nm and H = 220 nm.

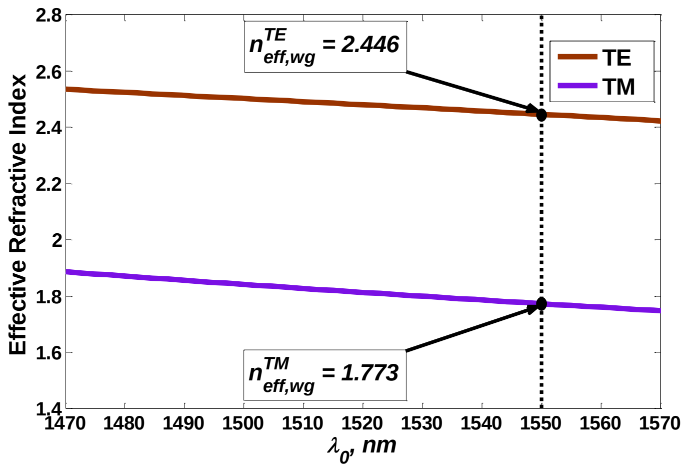

Figure 3.3: Simulated wavelength-dependent effective refractive indices for both the fundamental TE and TM modes of the single straight waveguide.

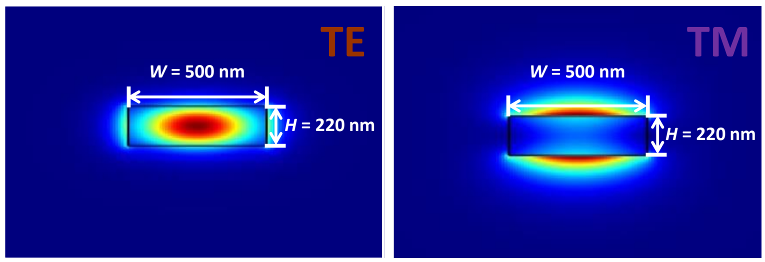

Figure 3.4: Simulated 2-D mode profiles for the fundamental TE mode (left) and the fundamental TM mode (right) at $\lambda_0 = 1550$ nm of the single straight waveguide, which has $W = 500$ nm and $H = 220$ nm.

Table 3.4: Simulated and calculated values of the $n_{eff,wg}$s, $n_{g,wg}$s, and β_{wg}s for both mode types at $\lambda_0 = 1550$ nm of the single straight waveguide.

Modes	**TE**	**TM**
$n_{eff,wg}$	2.446	1.773
$n_{g,wg}$	4.209	3.763
β_{wg}, nm^{-1}	0.009916	0.007188

the subscript, wg, is used when I intend to indicate that a particular variable is related to the single straight waveguide. Subsequently, $n_{g,wg}$ can be calculated, with respect to $n_{eff,wg}$, as:

$$n_{g,wg} = n_{eff,wg} - \lambda_0 \frac{dn_{eff,wg}}{d\lambda_0}, \tag{3.1}$$

and β_{wg} can also be calculated, with respect to $n_{eff,wg}$, as:

$$\beta_{wg} = \frac{2\pi}{\lambda_0} n_{eff,wg}. \tag{3.2}$$

Figure 3.3 shows the wavelength-dependent effective refractive indices for both the fundamental TE and TM modes of the single straight waveguide, and, referring to Eqs. 3.1 and 3.2 and Fig. 3.3, the values of the $n_{eff,wg}$s, $n_{g,wg}$s, and β_{wg}s for both mode types at $\lambda_0 = 1550$ nm of the waveguide structure are obtained and listed in Table 3.4. As shown in Fig. 3.4, the fundamental TE mode is better confined to the waveguide core than the fundamental TM mode at $\lambda_0 = 1550$ nm. Due to stronger confinement for the fundamental TE mode than for the fundamental TM mode to the waveguide core, the $n^{TE}_{eff,wg}$ is greater than the $n^{TM}_{eff,wg}$ at $\lambda_0 = 1550$ nm (see Fig. 3.3 and Table 3.4).

3.3 Coupling and AC Devices for TE Operation

Based on a symmetric two-waveguide structure, a straight symmetric DC and a sinusoidal AC symmetric waveguide pair can be designed for TE operation. The TE straight coupling device can be used as a reference to evaluate the performance of the TE sinusoidal AC device.

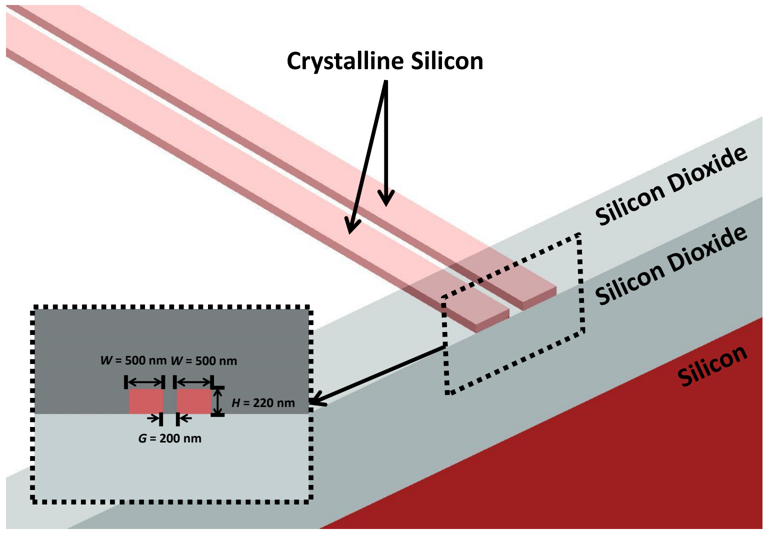

Figure 3.5: Perspective and cross-sectional views of a straight symmetric waveguide pair, which has $W = 500$ nm, $H = 220$ nm, and $G = 200$ nm.

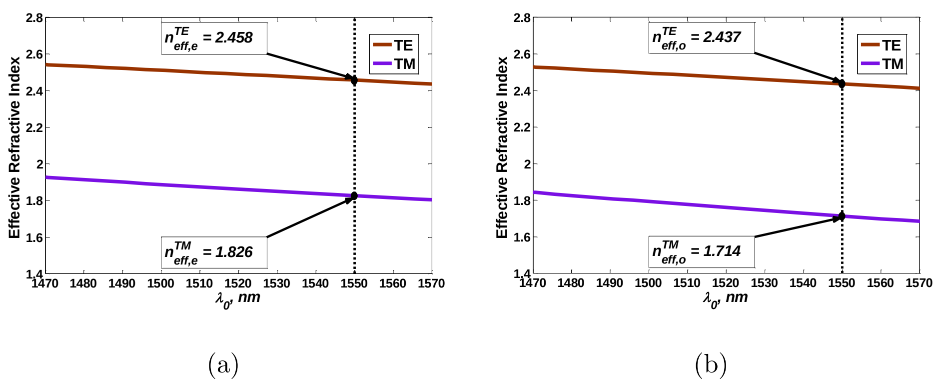

Figure 3.6: Simulated wavelength-dependent effective refractive indices for (a) the even TE and TM supermodes and (b) the odd TE and TM supermodes of the straight symmetric waveguide pair, which has $G = 200$ nm.

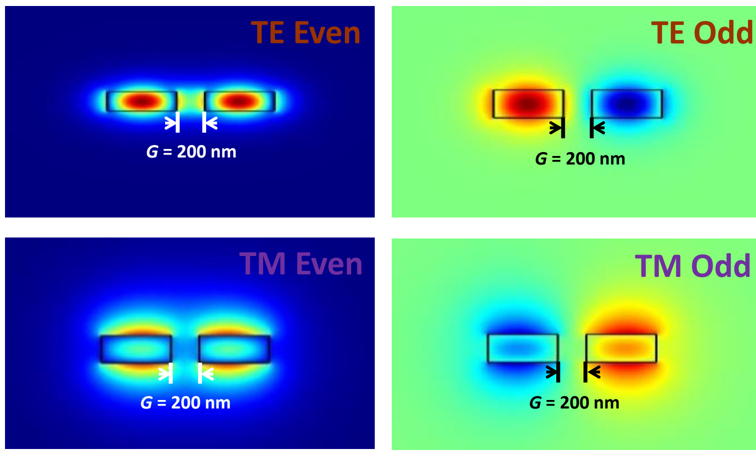

Figure 3.7: Simulated 2-D mode profiles for the even and odd TE supermodes (upper left and right, respectively) and the even and odd TM supermodes (lower left and right, respectively) at $\lambda_0 = 1550$ nm of the straight symmetric waveguide pair, which has $G = 200$ nm.

Table 3.5: Simulated and calculated values of the n_{eff}s and βs for both the TE and TM supermodes at $\lambda_0 = 1550$ nm of the straight symmetric waveguide pair, which has $G = 200$ nm.

Modes	**TE**	**TM**
$n_{eff,e}$	2.458	1.826
$n_{eff,o}$	2.437	1.714
β_e, nm^{-1}	0.009963	0.007404
β_o, nm^{-1}	0.009879	0.006948

3.3.1 TE Straight Symmetric DC

The value of G is chosen to be 200 nm for the TE straight symmetric DC. Using the FDE solver to simulate the cross-section of a straight symmetric waveguide pair, which has $W = 500$ nm, $H = 220$ nm, and $G = 200$ nm (see Fig. 3.5), I can obtain the $n_{eff,e}$ and $n_{eff,o}$ for the waveguide structure. Subsequently, β_e can be calculated, with respect to $n_{eff,e}$, as:

$$\beta_e = \frac{2\pi}{\lambda_0} n_{eff,e}, \tag{3.3}$$

and β_o can be calculated, with respect to $n_{eff,o}$, as:

$$\beta_o = \frac{2\pi}{\lambda_0} n_{eff,o}. \tag{3.4}$$

Figures 3.6a and 3.6b show the wavelength-dependent effective refractive indices for both the TE and TM supermodes of the straight symmetric waveguide pair. Referring to Eqs. 3.3 and 3.4 and Figs. 3.6a and 3.6b, the values of the $n_{eff,e}$s, $n_{eff,o}$s, β_es, and β_os for both the TE and TM supermodes at $\lambda_0 = 1550$ nm of the waveguide structure are obtained and listed in Table 3.5. As shown in Fig. 3.7, the even and odd TE supermodes are better confined to the waveguide cores than the TM even and odd supermodes at $\lambda_0 = 1550$ nm. Due to stronger confinement for the TE supermodes than for the TM supermodes to the waveguide cores, the $n^{TE}_{eff,e}$ and $n^{TE}_{eff,o}$ are greater than the $n^{TM}_{eff,e}$ and $n^{TM}_{eff,o}$, respectively, at $\lambda_0 = 1550$ nm (see Figs. 3.6a and 3.6b and Table 3.5).

Referring to Eq. 2.23 ($L_{c,min} = \frac{\pi}{\Delta\beta}$), I can calculate the $L_{c,min}$ to allow the maximum optical power transfer to the cross port of a straight symmetric DC for either TE or TM operation. Thus, referring to Eq. 2.23 and Table 3.5, I calculate the $L^{TE}_{c,min} = 37.40$ μm for the operation at $\lambda_0 = 1550$ nm of the DC, which has $G = 200$ nm. Since the circularly-bent branches are used

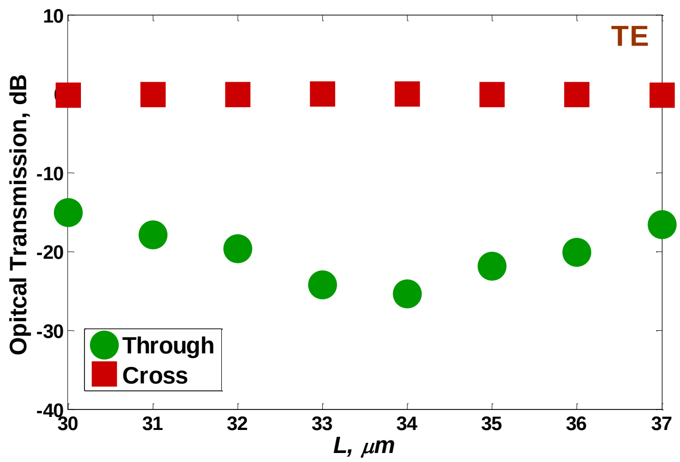

Figure 3.8: Simulated optical transmissions of the cross and through ports as functions with respect to L for TE operation at $\lambda_0 = 1550$ nm of straight symmetric DCs, which have $G = 200$ nm.

in my devices either to bring the waveguides closer or to separate them, from now on, my simulations include the coupling and insertion losses that are caused by the bifurcating branches. Then, using the FDTD solver, I simulate straight symmetric DCs, which have $G = 200$ nm, for TE operation and obtain an optimized value of the $L_{c,min}^{TE}$ to be 32.88 μm (see Fig. 3.8 and Ref. [2]). Figure 3.9 shows the 2-D power distribution profile for the operation at $\lambda_0 = 1550$ nm of the TE straight symmetric DC, which has $G = 200$ nm and $L = L_{c,min}^{TE} = 32.88$ μm, and TE optical power crosses over to the adjacent waveguide in the TE coupling device, when a fundamental TE mode is launched into Port 1 of the device.

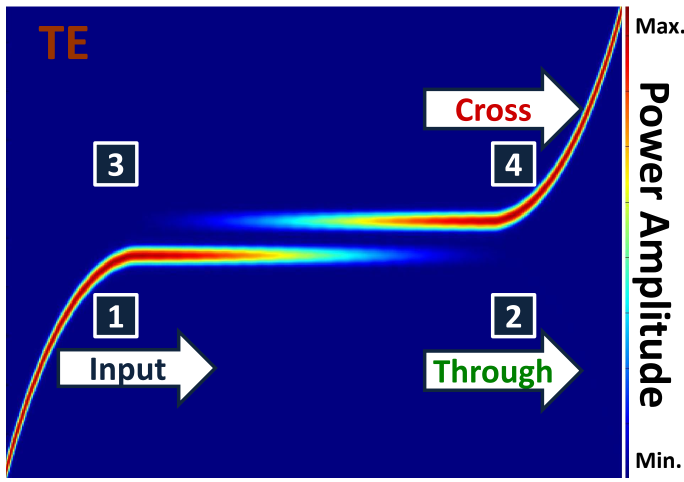

Figure 3.9: Simulated 2-D power distribution profile for the operation at $\lambda_0 = 1550$ nm of the straight symmetric DC, which has $G = 200$ nm and $L = 32.88$ μm, when a fundamental TE mode is launched into Port 1 of the device.

3.3.2 TE Sinusoidal AC Symmetric Waveguide Pair

Referring to Eq. 2.25 ($A_{min} \cong \frac{2.405\Lambda}{2\pi(W+G)\beta_{wg}}$), I can calculate the A_{min} to suppress the optical power exchange between the waveguides of a sinusoidal AC device for either TE or TM operation. I choose a value of the Λ to be 16.44 μm (by default, I choose $\Lambda = \frac{L_{c,min}}{2}$ for my sinusoidal AC devices) and, referring to Eq. 2.25 and Table 3.4, calculate the $A_{min}^{TE} = 906$ nm for the operation at $\lambda_0 = 1550$ nm of the sinusoidal AC device, which has $G = 200$ nm and $\Lambda = 16.44$ μm. Then, using the FDTD solver, I simulate sinusoidal symmetric waveguide pairs, which have $G = 200$ nm and $\Lambda = 16.44$ μm, for TE operation and obtain an optimized value of the A_{min}^{TE} to be 932 nm (see Fig. 3.10 and Ref. [2]). Figures 3.11a and 3.11b show the 2-D power distribution profiles for the operation at $\lambda_0 = 1550$ nm of

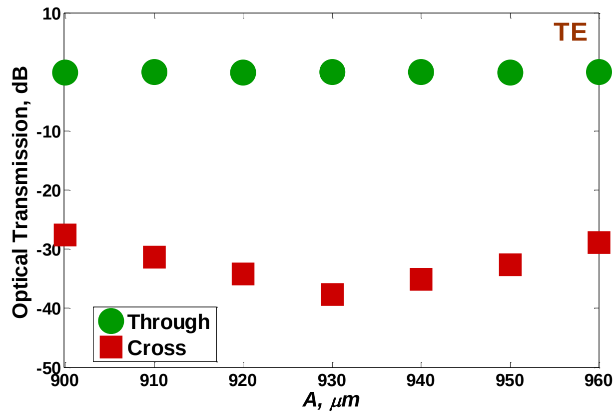

Figure 3.10: Simulated optical transmissions of the cross and through ports as functions with respect to A for TE operation at $\lambda_0 = 1550$ nm of sinusoidal symmetric waveguide pairs, which have the $G = 200$ nm and $\Lambda = 16.44$ μm.

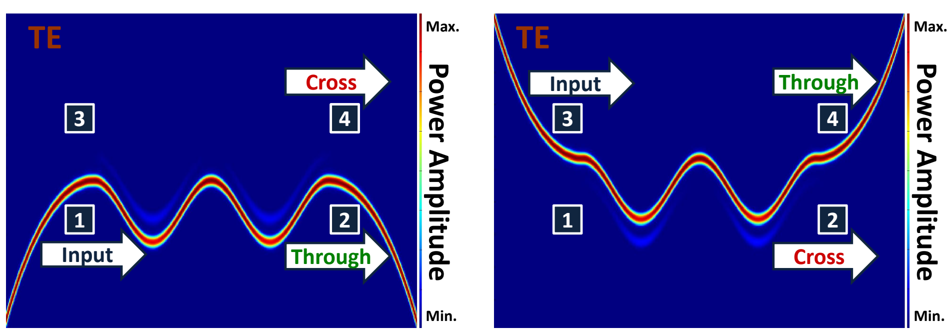

(a) (b)

Figure 3.11: Simulated 2-D power distribution profiles for the operation at $\lambda_0 = 1550$ nm of the sinusoidal AC symmetric waveguide pair, which has $G = 200$ nm, $L = 32.88$ μm, and $A = 932$ nm, when a fundamental TE mode is launched into each of (a) Port 1 and (b) Port 3 of the same device. Adapted with permission from Ref. [2], ©2015 Optical Society of America.

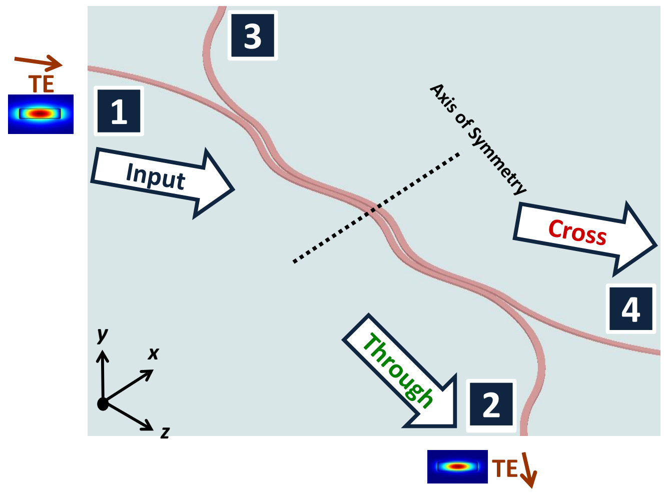

Figure 3.12: Perspective view of the TE sinusoidal AC device. Adapted with permission from Ref. [2], ©2015 Optical Society of America.

the TE sinusoidal AC symmetric waveguide pair, which has $G = 200$ nm, $L = 2\Lambda = L_{c,min}^{TE} = 32.88\ \mu$m, and $A = A_{min}^{TE} = 932$ nm, when a fundamental TE mode are launched into each of Ports 1 and 3 of the same device. In comparison with the equivalent TE straight symmetric DC (see Figs. 3.9), Fig. 3.11a illustrates that TE optical power exchange between the waveguides is suppressed and that TE optical power transfers from an input port to an output port along the same waveguide in the TE AC device, when a fundamental TE mode is launched into Port 1 of each device. As shown in Fig. 3.12, the device is symmetric with respect to the x axis, the injection of an optical signal into Port 1 is equivalent to that into Port 2, and the injection of an optical signal into Port 3 is equivalent to that into Port 4. Thus, the TE sinusoidal AC device can work as a four-port device.

3.3.3 Study for TM Operation

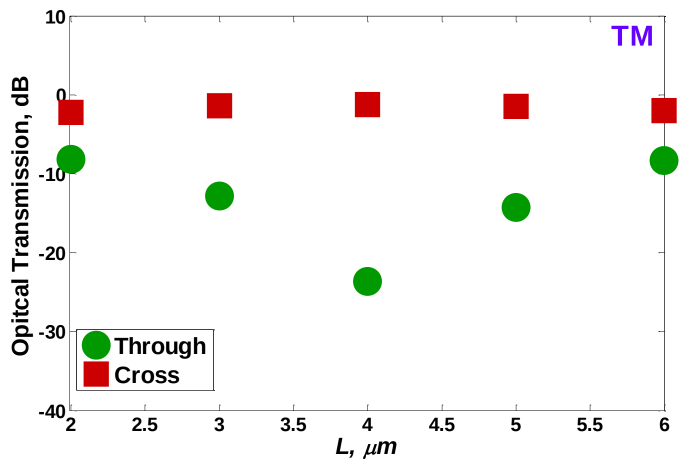

Figure 3.13: Simulated optical transmissions of the cross and through ports as functions with respect to L for TM operation at $\lambda_0 = 1550$ nm of straight symmetric DCs, which have $G = 200$ nm.

Here, I study the TE coupling and AC devices, which were studied above, for TM operation. Referring to Eq. 2.23 and Table 3.5, I calculate the value of $L_{c,min}^{TM}$ for the operation at $\lambda_0 = 1550$ nm of a straight symmetric DC, which has $G = 200$ nm (see Table 3.6). Then, using the FDTD solver, I simulate straight symmetric DCs, which have $G = 200$ nm, for TM operation and obtain an optimized value of the $L_{c,min}^{TM}$ (see Fig. 3.13 and Table 3.6). The calculated and optimized values of the $L_{c,min}^{TE}$s are also listed in Table 3.6. Due to weaker confinement for the TM supermodes than for the TE supermodes to the waveguide cores, TM optical power can transfer to the adjacent waveguide in a shorter length, the $L_{c,min}$, than TE optical power. As shown in Fig. 3.14, when a fundamental TM mode is launched into Port 1

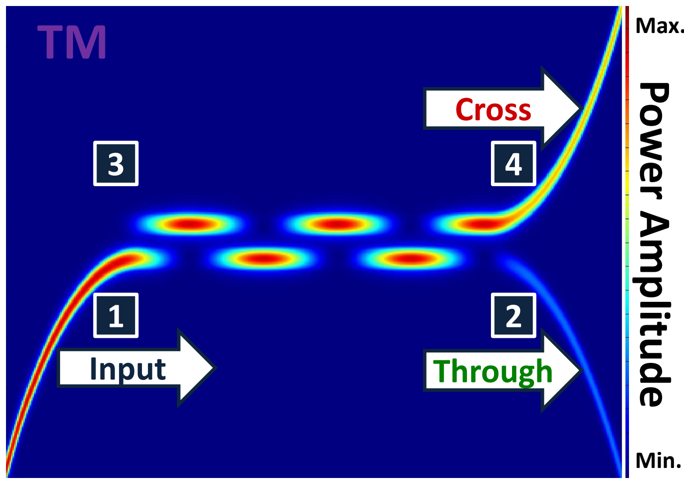

Figure 3.14: Simulated 2-D power distribution profile for the operation at λ_0 = 1550 nm of the TE straight symmetric DC, which has G = 200 nm and L = 32.88 μm, when a fundamental TM mode is launched into Port 1 of the device.

Table 3.6: Calculated and optimized values of the $L_{c,min}$s for both TE operation and TM operation at λ_0 = 1550 nm of the straight symmetric DCs, which have the same G = 200 nm (see Ref. [2]).

Operation		**TE**	**TM**
$L_{c,min}$, μm	**Calculated**	37.40	6.89
	Optimized	32.88	4

of the TE straight symmetric DC ($G = 200$ nm and $L = 32.88$ μm), which was studied above, the optical power crosses over between the waveguides in a much shorter length than when a fundamental TE mode is launched into Port 1 of the same device (see Fig. 3.9).

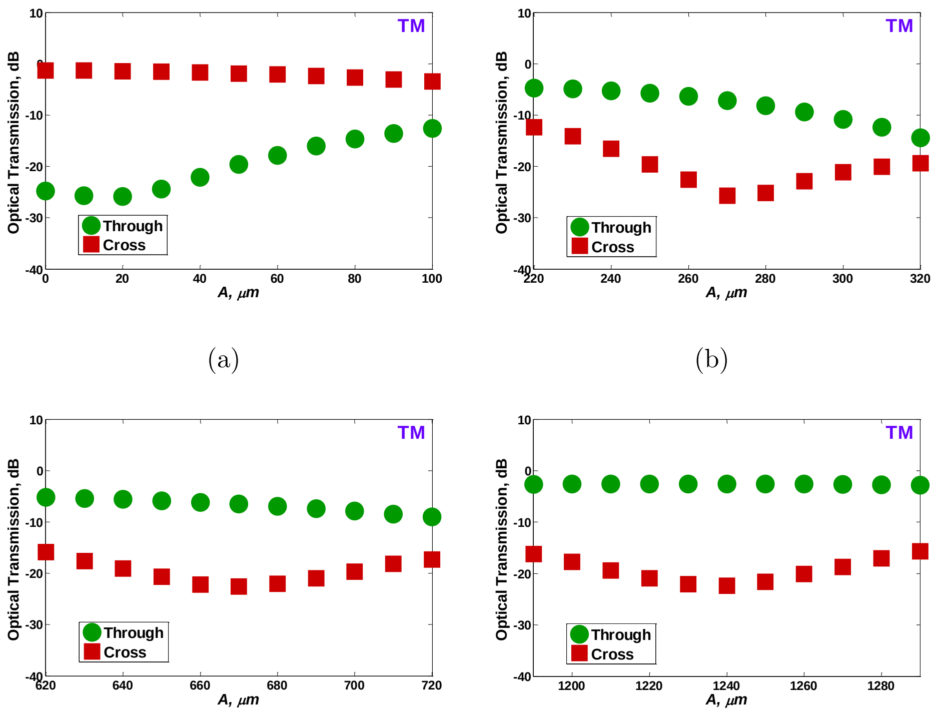

(a) (b)

(c) (d)

Figure 3.15: Simulated optical transmissions of the cross and through ports as functions with respect to A for TM operation at $\lambda_0 = 1550$ nm of sinusoidal symmetric waveguide pairs, which have $G = 200$ nm and have (a) $\Lambda = 2$ μm, (b) $\Lambda = 4$ μm, (c) $\Lambda = 8$ μm, and (d) $\Lambda = 16.44$ μm.

Thus, I choose the values of the Λs to be 2 μm, 4 μm, 8 μm, and 16.44 μm. Referring to Eq. 2.25 and Table 3.4, I calculate the values of the

Table 3.7: Calculated values of the A^{TM}_{min}s and optimized $A^{TM}_{cross,min}$s for the operation at $\lambda_0 = 1550$ nm of the sinusoidal symmetric waveguide pairs, which have $G = 200$ nm and different Λs.

Λ, μm		2	4	8	16.44
A^{TM}_{min}, nm	**Calculated**	152	304	608	1250
	Optimized	-	270	670	1240

A_{min}s of the sinusoidal symmetric waveguide pairs, which have $G = 200$ nm and different Λs (see Table 3.7). Then, using the FDTD solver, I simulate the sinusoidal symmetric waveguide pairs, which have $G = 200$ nm and different Λs, and obtain the optimized values of the A_{min}s (see Figs. 3.15a, 3.15b, 3.15c, and 3.15d, and Table 3.7).

As shown in Figs. 3.15a, the bending amplitudes that are near the calculated A^{TM}_{min} for $\Lambda = 2$ μm yield larger optical transmissions to the cross ports than the optical transmissions to the through ports. Thus, there is no practical A^{TM}_{min} for the sinusoidal AC device, which has $G = 200$ nm and $\Lambda = 2$ μm. Figures 3.16a, 3.16b, and 3.16c show the 2-D power distribution profiles for the operation at $\lambda_0 = 1550$ nm of the TM sinusoidal symmetric waveguide pairs, which have $G = 200$ nm, different Λs, and $L = 2\Lambda = L^{TM}_{c,min}$, when a fundamental TM mode is launched into Port 1 of each device. As shown in Figs. 3.15b, 3.15c, 3.15d, 3.16a, 3.16b, and 3.16c, those sinusoidal devices suffer from significant insertion losses and inter-waveguide crosstalk. The crosstalk is also becoming more intensive as the bending periods increase in those devices. As a result, there is no practical A^{TM}_{min} for those sinusoidal devices, which have $G = 200$ nm and various Λs.

Therefore, the sinusoidal bends need to have a Λ that is smaller than

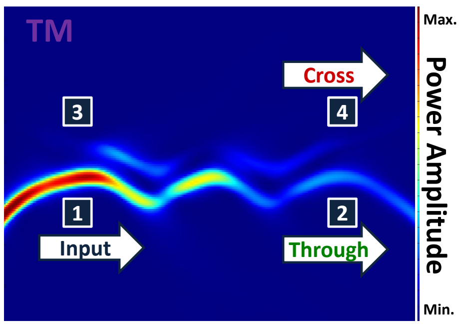

(a)

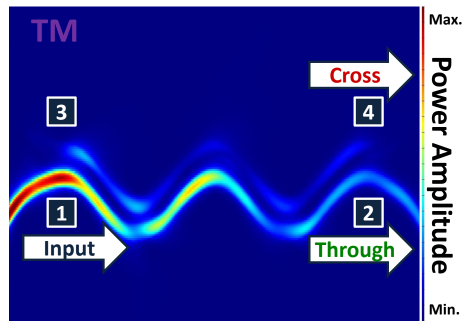

(b)

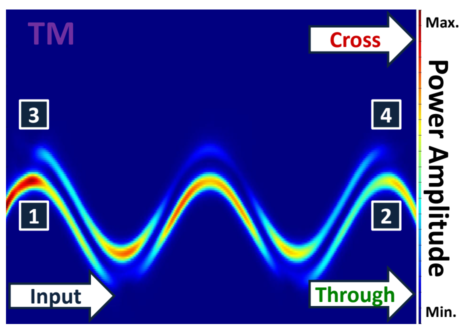

(c)

Figure 3.16: Simulated 2-D power distribution profiles for the operation at $\lambda_0 = 1550$ nm of the sinusoidal symmetric waveguide pairs, which have $G = 200$ nm and have (a) $\Lambda = 4$ μm, (b) $\Lambda = 8$ μm, and (c) $\Lambda = 16.44$ μm, when a fundamental TM mode is launched into Port 1 of each device.

or equal to the $L_{c,min}$ to allow for the suppression of optical power exchange between the waveguides. Meanwhile, due to weak confinement to the waveguide cores, the TM modes are much more susceptible to bending losses than the TE modes. Bending losses is proportional to bending curvature according to Ref. [46], and the bending curvature of a sinusoid is inversely proportional to the Λ (when the A remains the same). Thus, I need to choose an appropriate G for the TM sinusoidal AC device, which allows for sufficiently large $L_{c,min}^{TM}$ and Λ, so that the sinusoidal AC bends can be designed to have low insertion loss.

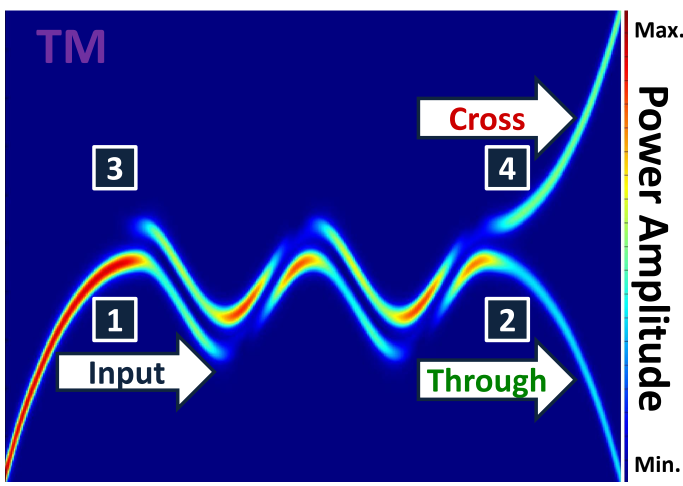

Figure 3.17: Simulated 2-D power distribution profile for the operation at λ_0 = 1550 nm of the TE sinusoidal AC symmetric waveguide pair, which has G = 200 nm, Λ = 16.44 μm, A = 932 nm, and L = 32.88 μm, when a fundamental TM mode is launched into Port 1 of the device.

As shown in Fig. 3.17, when a fundamental TM mode is launched into Port 1 of the TE sinusoidal AC symmetric waveguide pair (G = 200 nm, Λ = 16.44 μm, A = 932 nm, and L = 32.88 μm), which was also studied above, TM optical power exchange still takes place between the waveguides of the device. Hence, the AC effect of sinusoidal bends is sensitive to the polarization.

3.4 Coupling and AC Devices for TM Operation

Also based on a symmetric two-waveguide structure, a straight symmetric DC and a sinusoidal AC symmetric waveguide pair can be designed for TM operation. The TM straight coupling device can be used as a reference to evaluate the performance of the TM sinusoidal AC device. According to the study above, the selection of gap width for the TM sinusoidal AC device requires further investigation.

3.4.1 Selection of Gap Width

Table 3.8: Simulated and calculated values of the n_{eff}s and βs for both the even and odd TM supermodes at $\lambda_0 = 1550$ nm of the straight symmetric waveguide pairs, which have different Gs.

G, nm	300	400	500	600
$n_{eff,e}^{TM}$	1.806	1.794	1.786	1.781
$n_{eff,o}^{TM}$	1.736	1.750	1.759	1.764
β_e^{TM}, nm^{-1}	0.007320	0.007270	0.007240	0.007221
β_o^{TM}, nm^{-1}	0.007039	0.007096	0.007131	0.007153

Using the FDE solver to simulate the cross-sections of straight symmetric waveguide pairs, which have different Gs of 300 nm, 400 nm, 500 nm, and 600 nm, I can obtain the $n_{eff,e}$ and $n_{eff,o}$ for each of them. Figures 3.18a,

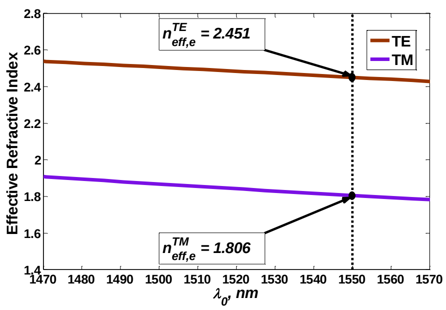

(a)

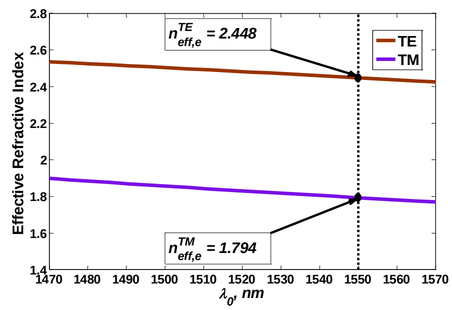

(b)

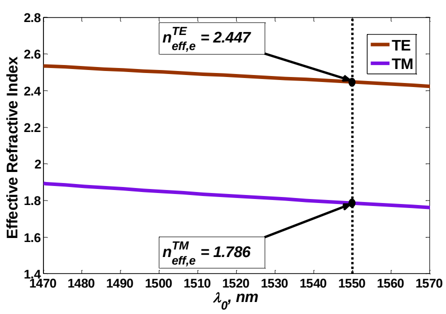

(c)

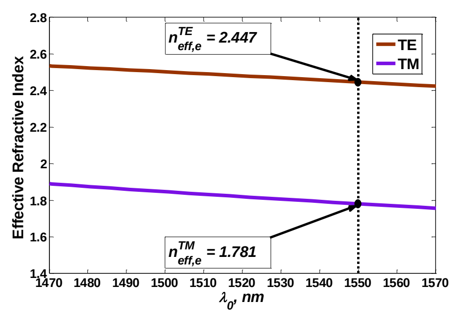

(d)

Figure 3.18: Simulated wavelength-dependent effective refractive indices for both the even TE and TM supermodes of the straight symmetric waveguide pairs, which have (a) $G = 300$ nm, (b) $G = 400$ nm, (c) $G = 500$ nm, and (d) $G = 600$ nm.

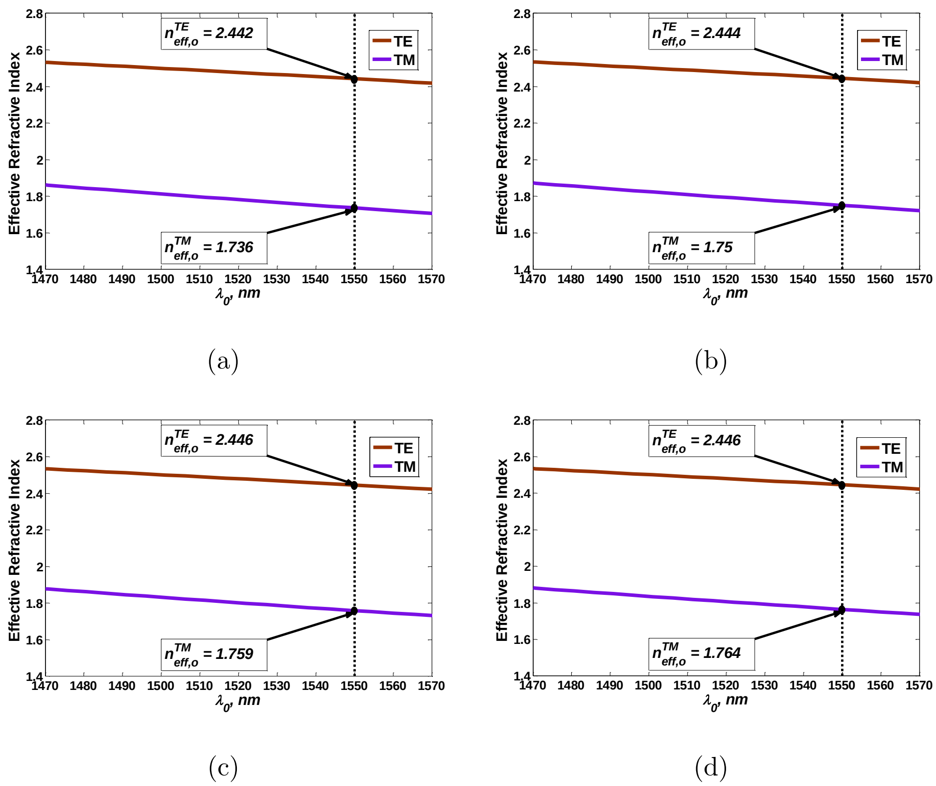

Figure 3.19: Simulated wavelength-dependent effective refractive indices for both the odd TE and TM supermodes of the straight symmetric waveguide pairs, which have (a) G = 300 nm, (b) G = 400 nm, (c) G = 500 nm, and (d) G = 600 nm.

3.18b, 3.18c, 3.18d, 3.19a, 3.19b, 3.19c, and 3.19d show the wavelength-dependent effective refractive indices for both the TE and TM supermodes of those straight symmetric waveguide pairs. Referring to Eqs. 3.3 and 3.4 and Figs. 3.18a, 3.18b, 3.18c, 3.18d, 3.19a, 3.19b, 3.19c, and 3.19d, the values of the $n_{eff,e}$s, $n_{eff,o}$s, β_es, and β_os for both the even and odd TM supermodes at $\lambda_0 = 1550$ nm of the waveguide structures are obtained and listed in Table 3.8.

Table 3.9: Calculated and optimized values of the $L^{TM}_{c,min}$s for the operation at $\lambda_0 = 1550$ nm of the straight symmetric DCs, which have different Gs.

G, nm		300	400	500	600
$L^{TM}_{c,min}$, μm	**Calculated**	11.18	18.06	28.82	46.20
	Optimized	8	14	24	39.72

Referring to Eq. 2.23 and Table 3.8, I calculate the values of the $L^{TM}_{c,min}$s for the operation at $\lambda_0 = 1550$ nm of the straight symmetric DCs, which have different Gs (see Table 3.9). Then, using the FDTD solver, I simulate straight symmetric DCs, which have different Gs, for TM operation and obtain the optimized values of the $L^{TM}_{c,min}$s (see Figs. 3.20a, 3.20b, 3.20c, and 3.20d and Table 3.9).

The chosen values of the Λs and the calculated values of the A^{TM}_{min}s (referring to Eq. 2.25 and Table 3.4) are listed in Table 3.10. Then, using the FDTD solver, I simulate the sinusoidal symmetric waveguide pairs, which have different Gs, for TM operation and obtain the optimized values of the A^{TM}_{min}s (see Table 3.10). Figures 3.22a, 3.22b, 3.22c, and 3.22d show the 2-D power distribution profiles for the operation at $\lambda_0 = 1550$ nm of the TM sinusoidal AC symmetric waveguide pairs, which have different Gs, Λs, and

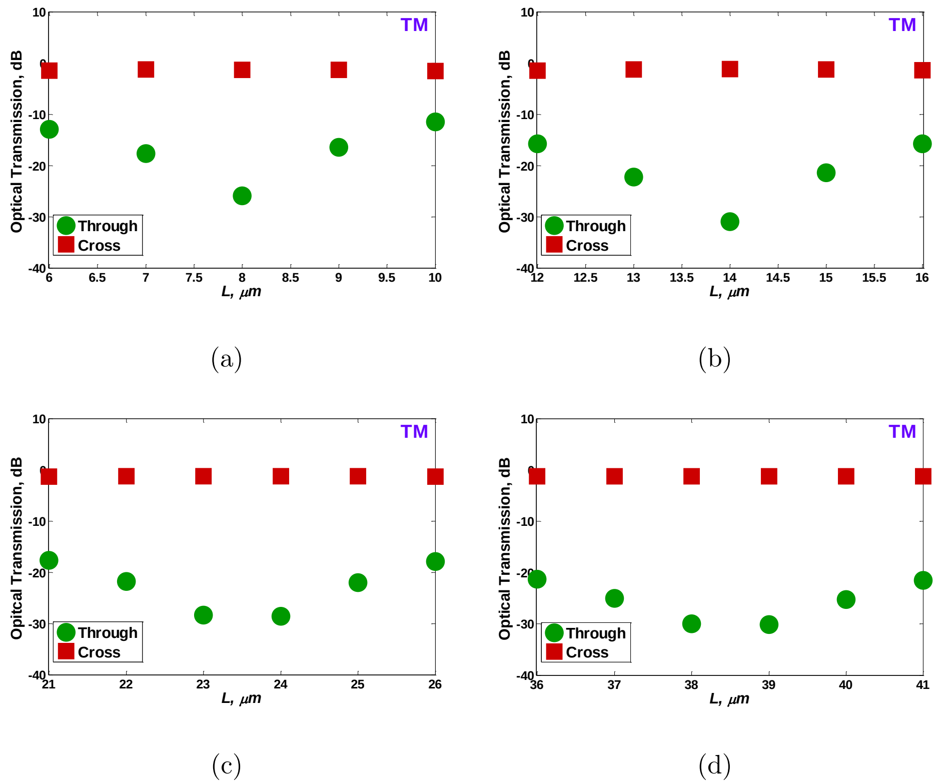

Figure 3.20: Simulated optical transmissions of the cross and through ports as functions with respect to L for TM operation at $\lambda_0 = 1550$ nm of straight symmetric DCs, which have (a) $G = 300$ nm, (b) $G = 400$ nm, (c) $G = 500$ nm, and (d) $G = 600$ nm.

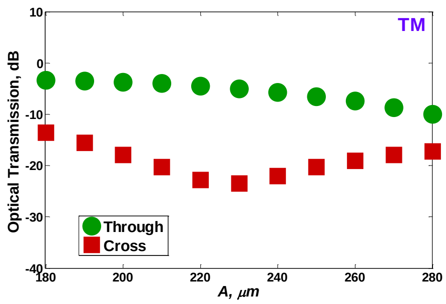

(a)

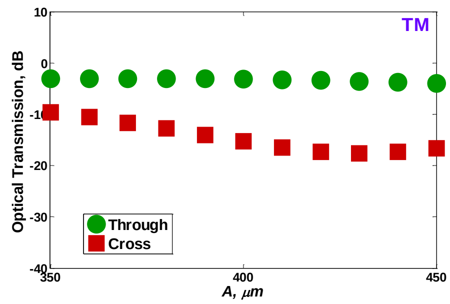

(b)

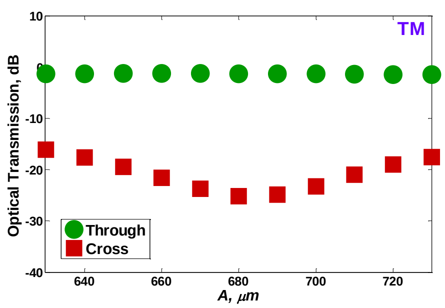

(c)

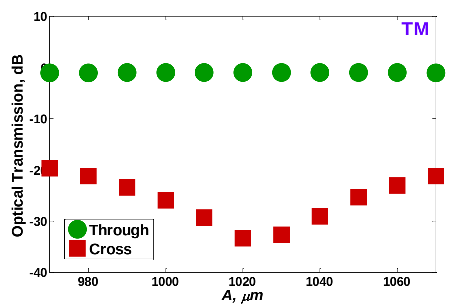

(d)

Figure 3.21: Simulated optical transmissions of the cross and through ports as functions with respect to A for TM operation at $\lambda_0 = 1550$ nm of sinusoidal symmetric waveguide pairs, which have (a) $G = 300$ nm, (b) $G = 400$ nm, (c) $G = 500$ nm, and (d) $G = 600$ nm.

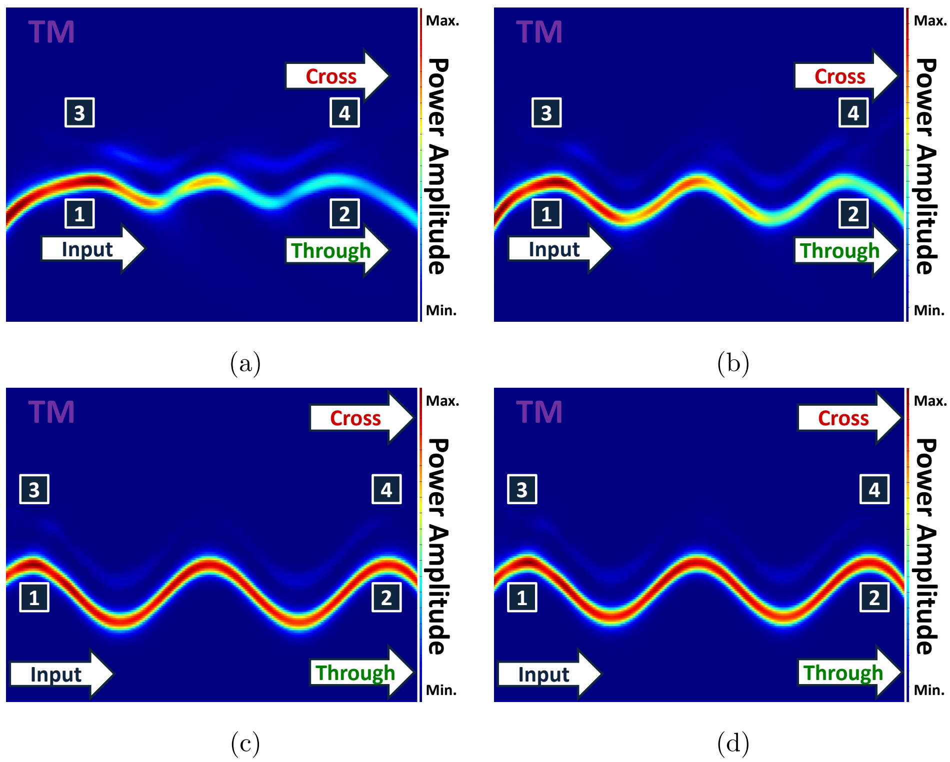

Figure 3.22: Simulated 2-D power distribution profiles for the operation at $\lambda_0 = 1550$ nm of the sinusoidal AC symmetric waveguide pairs, which have (a) $G = 300$ nm, (b) $G = 400$ nm, (c) $G = 500$ nm, and (d) $G = 600$ nm, when a fundamental TM mode is launched into Port 1 of each device.

Table 3.10: Calculated and optimized values of the A_{min}^{TM}s for the operation at $\lambda_0 = 1550$ nm of the sinusoidal AC symmetric waveguide pairs, which have different Gs.

G, nm		300	400	500	600
Λ, μm		4	7	12	19.86
A_{min}^{TM}, nm	**Calculated**	266	414	639	961
	Optimized	230	430	680	1025

$L = 2\Lambda = L_{c,min}^{TM}$, when a fundamental TM mode is launched into Port 1 of each device. As shown in Figs. 3.21a, 3.21b, 3.21c, 3.21d, 3.22a, 3.22b, 3.22c, and 3.22d, the insertion losses are getting closer to 0 dB and the crosstalk suppressions are getting larger as the values of Gs increase from 300 nm to 600 nm for those devices.

A larger G results in a larger $L_{c,min}^{TM}$, a larger Λ, and a larger device footprint. As shown in Figs. 3.21c, 3.21d, 3.22c, and 3.22d, there is little improvement in either the insertion loss or the crosstalk suppression for the TM sinusoidal AC devices when the Gs increase from 500 nm to 600 nm. Hence, I choose $G = 600$ nm, which allows the TM sinusoidal AC device to have a compact device footprint, a large crosstalk suppression, and a low insertion loss.

3.4.2 TM Straight Symmetric DC

As shown in Fig. 3.23, the even and odd TM supermodes of a straight symmetric waveguide pair, which has $W = 500$ nm, $H = 220$ nm, and $G = 600$ nm (see Fig. 3.24), are less confined to the waveguide cores than the even and odd TE supermodes at $\lambda_0 = 1550$ nm. Due to weaker confine-

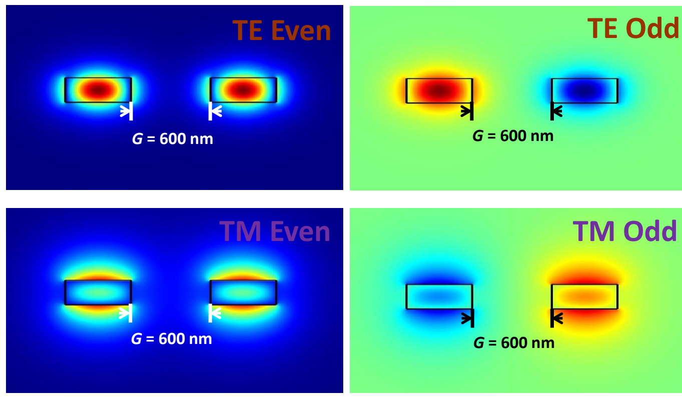

Figure 3.23: Simulated 2-D mode profiles for the even and odd TE supermodes (upper left and right, respectively) and the even and odd TM supermodes (lower left and right, respectively) at $\lambda_0 = 1550$ nm of the straight symmetric waveguide pair, which has $G = 600$ nm.

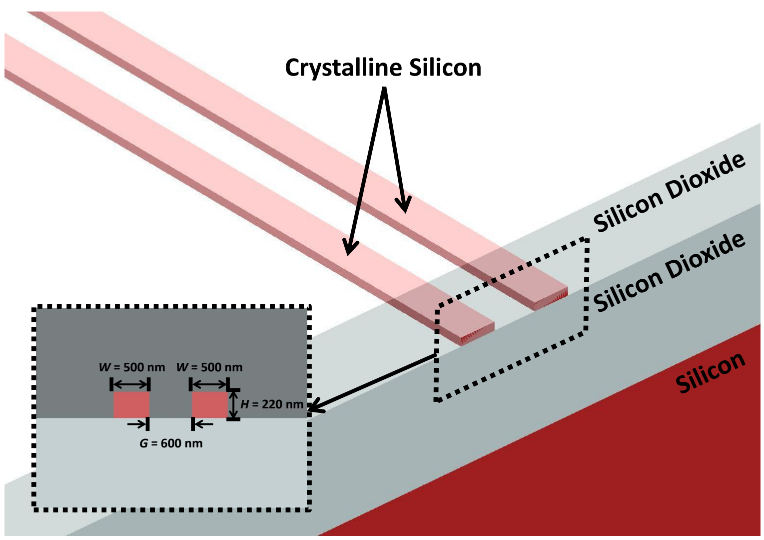

Figure 3.24: Perspective and cross-sectional views of a straight symmetric waveguide pair, which has $W = 500$ nm, $H = 220$ nm, and $G = 600$ nm.

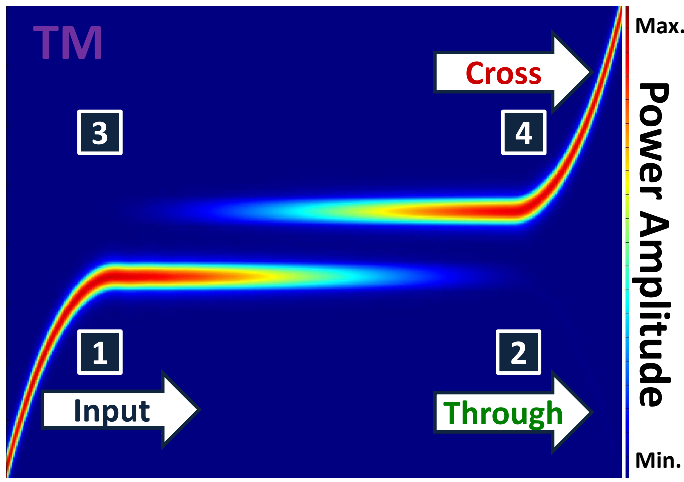

Figure 3.25: Simulated 2-D power distribution profile for the operation at $\lambda_0 = 1550$ nm of the straight symmetric DC, which has $G = 600$ nm and $L = 39.72$ μm, when a fundamental TM mode is launched into Port 1 of the device.

ment for the TM supermodes than for the TE supermodes to the waveguide cores, the $n_{eff,e}^{TM}$ and $n_{eff,o}^{TM}$ are smaller than the $n_{eff,e}^{TE}$ and $n_{eff,o}^{TE}$, respectively, at $\lambda_0 = 1550$ nm (see Figs. 3.18d and 3.19d and Table 3.8). Figure 3.25 shows the 2-D power distribution profile for the operation at $\lambda_0 = 1550$ nm of the TM straight symmetric DC, which has $G = 600$ nm and $L = L_{c,min}^{TM} = 39.72$ μm (see Table 3.9), and TM optical power crosses over to the adjacent waveguide in the TM coupling device, when a fundamental TM mode is launched into Port 1 of the device.

3.4.3 TM Sinusoidal AC Symmetric Waveguide Pair

Figures 3.26a and 3.26b show the 2-D power distribution profiles for the operation at $\lambda_0 = 1550$ nm of the TM sinusoidal AC symmetric waveguide pair,

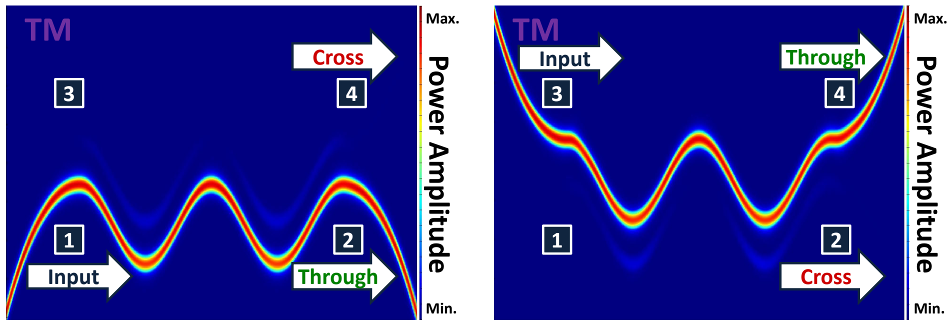

(a) (b)

Figure 3.26: Simulated 2-D power distribution profiles for the operation at $\lambda_0 = 1550$ nm of the sinusoidal AC symmetric waveguide pair, which has , $\Lambda = 19.86\ \mu$m, $A_{min}^{TM} = 1025$ nm, and $L = 39.72\ \mu$m, when a fundamental TM mode is launched into each of (a) Port 1 and (b) Port 3 of the same device.

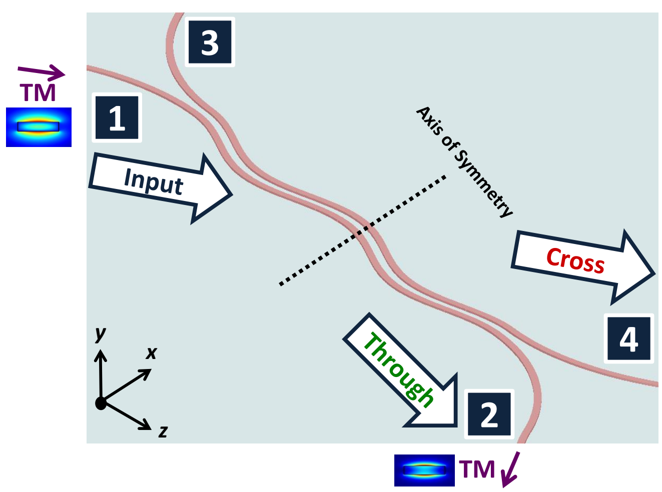

Figure 3.27: Perspective view of the TM sinusoidal AC device.

which has $G = 600$ nm, $L = L_{c,min}^{TM} = 39.72$ μm, and $A = A_{min}^{TM} = 1025$ nm (see Tables 3.9 and 3.7), when a fundamental TM modes is launched into each of Ports 1 and 3 of the same device. In comparison with the equivalent TM straight symmetric DC (see Fig. 3.25), Fig. 3.26a illustrates that TM optical power exchange between the waveguides is suppressed and that TM optical power transfers from an input port to an output port along the same waveguide in the TM AC device, when a fundamental TM mode is launched into Port 1 of the device. As shown in Fig. 3.27, the device is symmetric with respect to the x axis. Thus, the TM sinusoidal AC symmetric waveguide pair can work as a four-port device.

3.5 PBS using a Symmetric DC with Sinusoidal Bends

The polarization sensitivity of the sinusoidal AC bends can be used to design polarization selective devices (eg. a PBS). In the TE sinusoidal AC device, TE optical power propagates along the same waveguide (Fig. 3.11a), and TM optical power can transfer to the adjacent waveguide in a relatively short length (see Fig. 3.17). Therefore, I can design a compact PBS using the TE sinusoidal AC symmetric waveguide structure ($G = 200$ nm, $\Lambda = 16.44$ μm, and $A = 932$ nm), which was studied above.

3.5.1 Optimization

Using the FDTD solver, I simulate symmetric DCs with sinusoidal bends and the optimize the L of the devices, so that the maximum TM optical power transfer to the adjacent waveguide is allowed and TE optical power

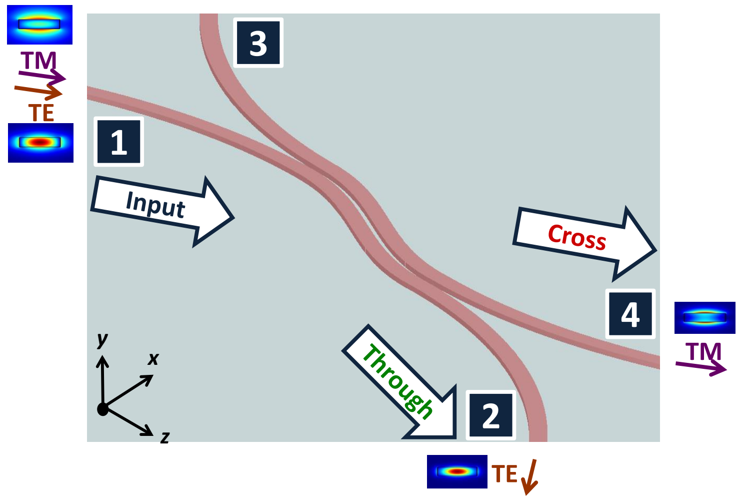

Figure 3.28: Perspective view of the PBS. Adapted with permission from Ref. [1], ©2017 Optical Society of America.

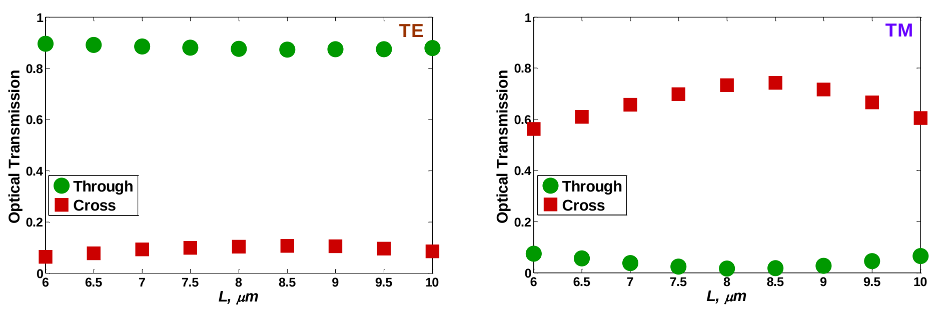

(a)

(b)

Figure 3.29: Simulated optical transmissions (on a linear scale) of the cross and through ports as functions with respect to L for (a) TE operation and (b) TM operation at $\lambda_0 = 1550$ nm of symmetric DCs with sinusoidal bends, which have $G = 200$ nm, $\Lambda = 16.44$ μm, and $A = 932$ nm. Adapted with permission from Ref. [1], ©2017 Optical Society of America.

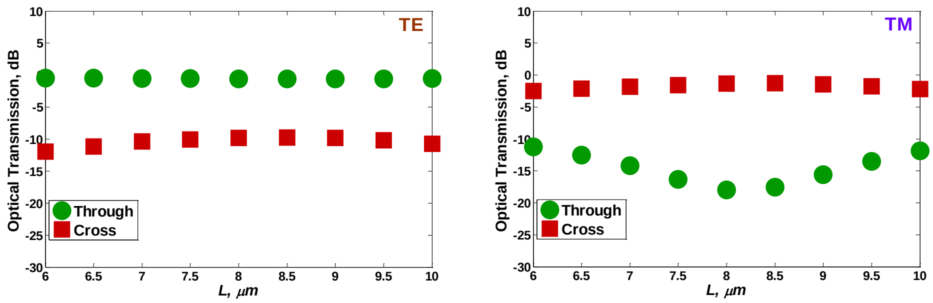

(a) (b)

Figure 3.30: Simulated optical transmissions (on a logarithmic scale) of the cross and through ports as functions with respect to L for (a) TE operation and (b) TM operation at $\lambda_0 = 1550$ nm of symmetric DCs with sinusoidal bends, which have $G = 200$ nm, $\Lambda = 16.44$ μm, and $A = 932$ nm. Adapted with permission from Ref. [1], ©2017 Optical Society of America.

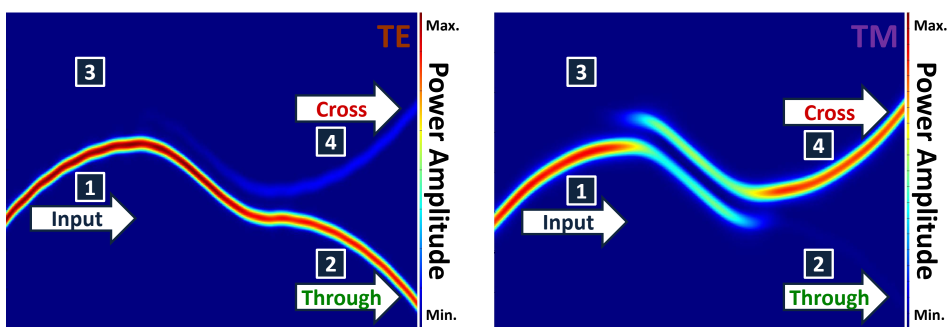

(a) (b)

Figure 3.31: Simulated 2-D power distribution profiles for the operation at $\lambda_0 = 1550$ nm of the PBS, when (a) a fundamental TE mode and (b) a fundamental TM mode are launched into Port 1 of the same device. Adapted with permission from Ref. [1], ©2017 Optical Society of America.

exchange between the waveguides is suppressed in the device (see Fig. 3.28). Referring to Figs. 3.29a, 3.29b, 3.30a, and 3.30b, I choose $L = 8.55$ μm for my PBS (see Ref. [1]). Figures 3.31a and 3.31b show the 2-D power distribution profiles for the operation at $\lambda_0 = 1550$ nm of the PBS, and the TE and TM modes diverge into two different waveguides in the device, when both the fundamental TE and TM modes are launched into Port 1 of the same device.

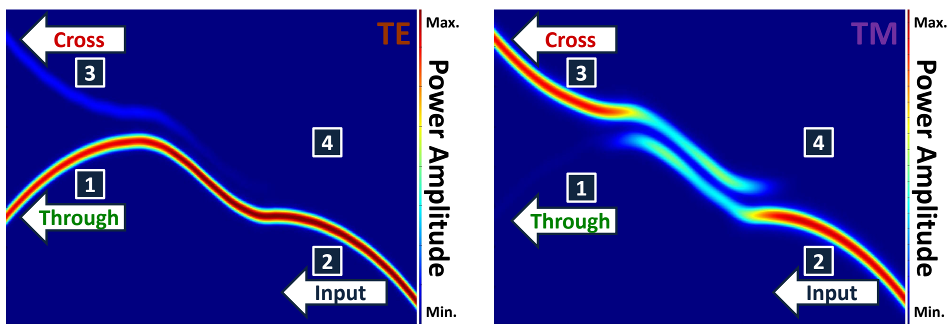

(a) (b)

Figure 3.32: Simulated 2-D power distribution profiles for the operation at $\lambda_0 = 1550$ nm of the PBS, when (a) a fundamental TE mode and (b) a fundamental TM mode are launched into Port 2 of the same device.

In addition, Figs. 3.32a, 3.32b, 3.33a, 3.33b, 3.34a, and 3.34b also illustrate that the fundamental TE and TM are separated into two different ports of the device, when both of the fundamental modes are launched into each of Ports 2, 3, and 4 of the same device. Hence, the PBS using a symmetric DC with sinusoidal bends can work as a four-port device and can also work as a polarization beam combiner.

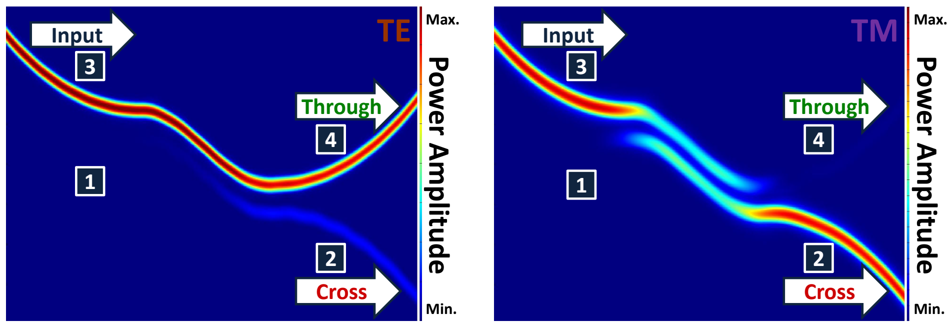

(a) (b)

Figure 3.33: Simulated 2-D power distribution profiles for the operation at λ_0 = 1550 nm of the PBS, when (a) a fundamental TE mode and (b) a fundamental TM mode are launched into Port 3 of the same device.

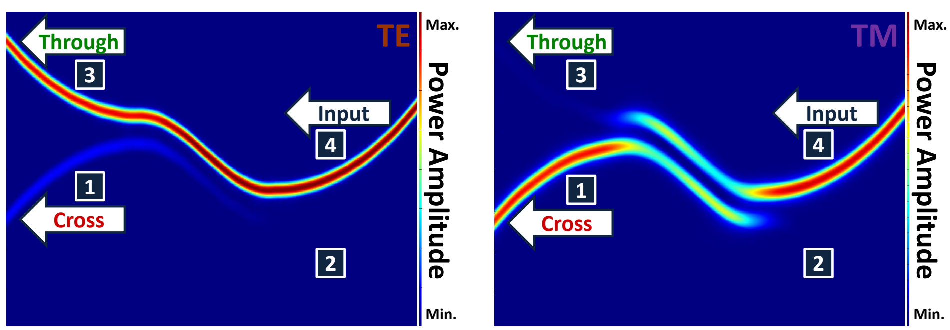

(a) (b)

Figure 3.34: Simulated 2-D power distribution profiles for TM operation at λ_0 = 1550 nm of the PBS, when (a) a fundamental TE mode and (b) a fundamental TM mode are launched into Port 4 of the same device.

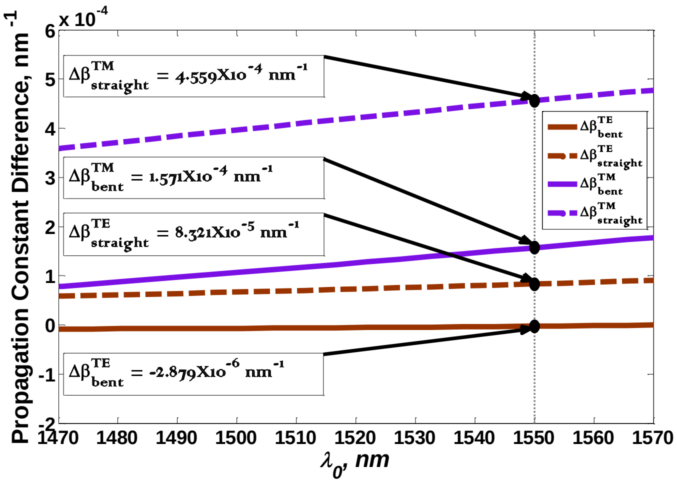

Figure 3.35: Calculated wavelength-dependent propagation constant differences for both the TE and TM modes of the sinusoidally-bent and straight symmetric DCs, which have $G = 200$ nm.

Table 3.11: Calculated values of the $\Delta\beta_{bent}$s and $\Delta\beta_{straight}$s and absolute values of their ratios for both mode types at $\lambda_0 = 1550$ nm of the bent and straight DCs.

Modes	**TE**	**TM**
$\Delta\beta_{bent}$, nm^{-1}	-2.879×10^{-6}	1.571×10^{-4}
$\Delta\beta_{straight}$, nm^{-1}	8.321×10^{-5}	4.559×10^{-4}
$\lvert\frac{\Delta\beta_{bent}}{\Delta\beta_{straight}}\rvert$	0.03460	0.3446

3.5.2 Modal Dispersion

Referring to Eqs. 3.3, and 3.4 and Figs. 3.3, 3.6a, and 3.6b, the wavelength-dependent propagation constant differences for both the TE and TM modes of a straight symmetric DC, which has G = 200 nm, are calculated and shown in Fig. 3.35. Then, referring to Eq. 2.24 ($\Delta\beta_{bent} \cong \Delta\beta_{straight} J_0\big[\frac{2\pi A(W+G)}{\Lambda}\beta_{wg}\big]$) and 3.2 and Figs. 2.8, 3.3, and 3.35, the wavelength-dependent propagation constant differences for both the TE and TM modes of the sinusoidally-bent symmetric DC, which is used in my PBS, are calculated and shown in Fig. 3.35. Therefore, referring to Fig. 3.35, the values of the $\Delta\beta_{bent}$s and $\Delta\beta_{straights}$s and the absolute values of their ratios for both mode types at λ_0 = 1550 nm of the bent and straight DCs are obtained and listed in Table 3.11. Referring to Fig. 3.35 and Table 3.11, the sinusoidal bends reduce TE coupling between the waveguides by approximately 96.5 % and reduce TM coupling between the waveguides by approximately 65.5 % for the bent DC as compared to the equivalent straight DC, thus, the sinusoidally-bent symmetric DC in my PBS only allows TM optical power to cross over to the adjacent waveguide and has a cross-over length that is greater than the equivalent straight DC for TM operation (see Ref. [1]).

Table 3.12: Calculated values of the $\mathbb{D}_{bent}$s and $\mathbb{D}_{straight}$s and absolute values of their ratios for both mode types at λ_0 = 1550 nm of the bent and straight DCs.

Modes	**TE**	**TM**
$\mathbb{D}_{bent}$, ps·μm^{-1}·nm^{-1}	-8.257×10^{-8}	-9.321×10^{-7}
$\mathbb{D}_{straight}$, ps·μm^{-1}·nm^{-1}	-3.491×10^{-7}	-1.153×10^{-6}
$\lvert\frac{\mathbb{D}_{bent}}{\mathbb{D}_{straight}}\rvert$	0.2365	0.8084

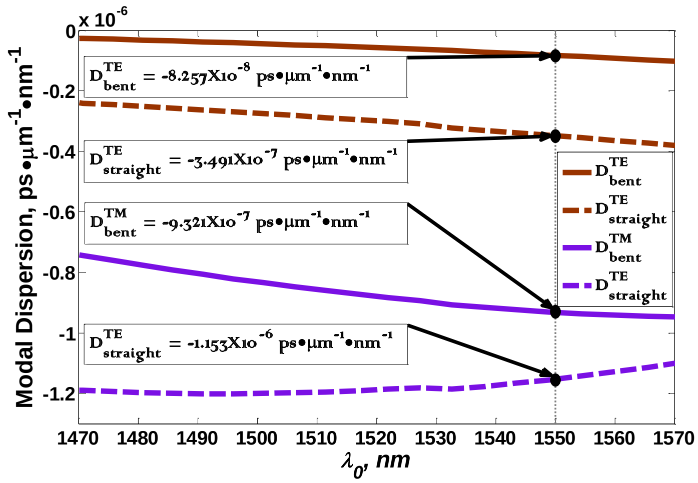

Figure 3.36: Calculated wavelength-dependent modal dispersions for both the TE and TM modes of the sinusoidally-bent and straight symmetric DCs, which have $G = 200$ nm.

Referring to Eq. 2.31 ($\mathbb{D} = \frac{-1}{2\pi c}\left(\Delta\beta + \lambda_0 \frac{d\Delta\beta}{d\lambda_0}\right)$) and Fig. 3.35, the wavelength-dependent modal dispersions for both the TE and TM modes of the bent and straight DCs are calculated and shown in Fig. 3.36. The values of the $\mathbb{D}_{bent}$s and $\mathbb{D}_{straight}$s and the absolute values of their ratios for both mode types at $\lambda_0 = 1550$ nm of the bent and straight devices are obtained and listed in Table 3.12. Referring to Fig. 3.36 and Table 3.12, the sinusoidally-bent symmetric DC in my PBS has lower wavelength dependencies and better broadband performances than the equivalent straight symmetric DC for both the TE and TM modes (see Ref. [1]).

3.6 Summary

In this chapter, a single straight waveguide, straight symmetric DCs, sinusoidal AC symmetric waveguide pairs, and a PBS using a symmetric DC with sinusoidal bends were simulated for TE and/or TM operation on an SOI platform. The design parameters for the sinusoidal AC devices and the PBS were optimized using the simulation data. The wavelength dependencies of the sinusoidally-bent symmetric DC, which was used in the PBS, were also compared with the equivalent straight symmetric DC for the TE and TM modes.

Chapter 4

Fabrication, Measurement, and Demonstration

In this Chapter, I present the fabrication, measurement, and demonstration of the TE and TM sinusoidal AC symmetric waveguide pairs and a PBS using a symmetric DC with sinusoidal bends. Using the optimized design parameters that I obtained from the previous chapter, I created the mask layouts for the fabrication of those devices. I also added the straight symmetric DCs and straight AC asymmetric waveguides to the mask layouts in order to evaluate the performances of the sinusoidal AC devices. All of the devices were fabricated using electron-beam (E-Beam) lithography on an SOI platform. Using an automated optical fibre probe station in our lab, I measured the fabricated test devices. Then, using the measurement data, I demonstrate a sinusoidal AC waveguide pair for TE operation, a sinusoidal AC waveguide pair for TM operation, and a PBS using a symmetric DC with sinusoidal bends for both TE operation and TM operation. I also evaluate their performances accordingly.[1]

[1]Sections 4.1, 4.2, and 4.3.3 are based on the work in the published paper [1], and Sections 4.1, 4.2, and 4.3.1 are based on the work in the published paper [2].

4.1 Fabrication

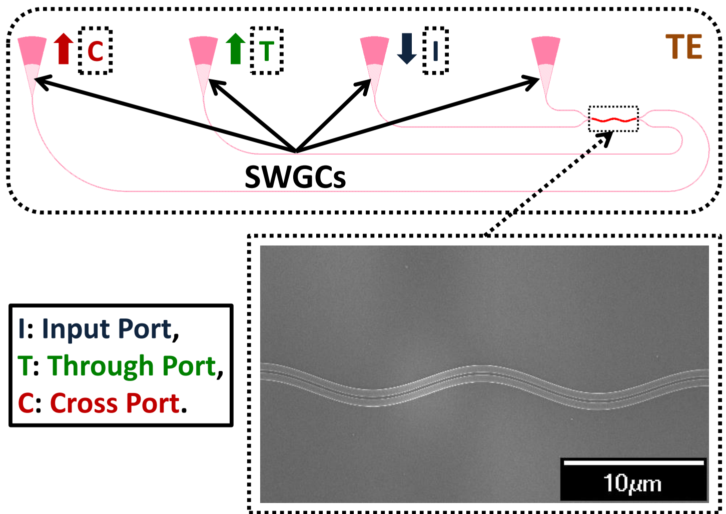

Figure 4.1: Design layout (left) of the TE sinusoidal AC symmetric waveguide pair with an SEM image (right) of the sinusoidal symmetric waveguide structure in the device.

The mask layouts of my test devices (see Figs. 4.1, 4.2, and 4.3) were drawn using Pyxis layout editor (from Mentor Graphics, Inc.). The test devices were fabricated on a 220-nm-thick crystalline silicon layer of an SOI wafer (see Fig. 4.4) using E-Beam lithography, and a layer of 2-μm-thick silicon dioxide were deposited over the devices at the University of Washington. As shown in Fig. 4.4, the wafer also consists of a 3-μm-thick silicon dioxide layer and a 675-μm-thick silicon layer. The fabrication processes are compatible with CMOS technologies. Scanning-electron-microscope (SEM) images in Figs. 4.1, 4.2, and 4.3 show the sinusoidal symmetric waveguide structures of the fabricated test devices (the TE sinusoidal AC device in Ref. [2] and the PBS in Ref. [1]).

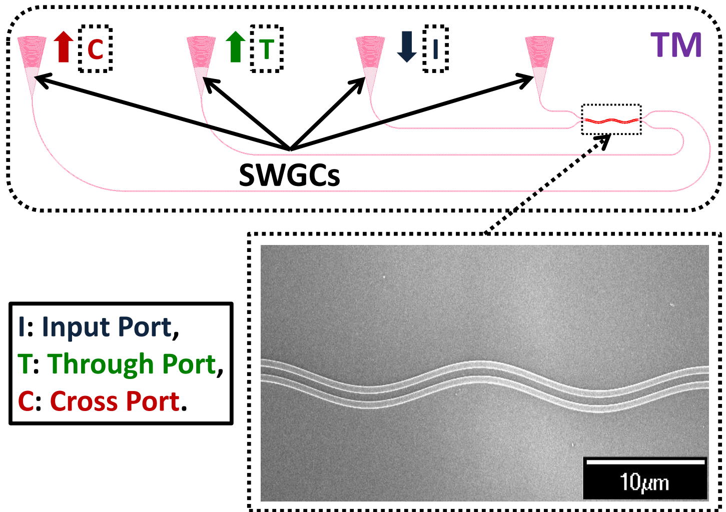

Figure 4.2: Design layout (left) of the TM sinusoidal AC symmetric waveguide pair with an SEM image (right) of the sinusoidal symmetric waveguide structure in the device.

4.2 Measurement

As shown in Figs. 4.1, 4.2, and 4.3, sub-wavelength grating couplers (SWGCs) in Refs. [47, 48] were used to couple light in and out of each of the test devices. A reference device is a pair of SWGCs, which are directly connected to each other by a waveguide, for either TE or TM operation. There is one reference device, near each of the test devices, and its spectral response can be used to normalize the measurement data of the test device for the corresponding mode type (see Refs. [1, 2]). Figure 4.5 shows the TE reference device for the TE sinusoidal AC device, as well as one of the TE SWGCs that were used in these devices. Figure 4.6 shows the reference device for the PBS for TE operation, as well as one of the TE SWGCs that were used in these devices. Figure 4.7 shows the reference device for the TM sinusoidal

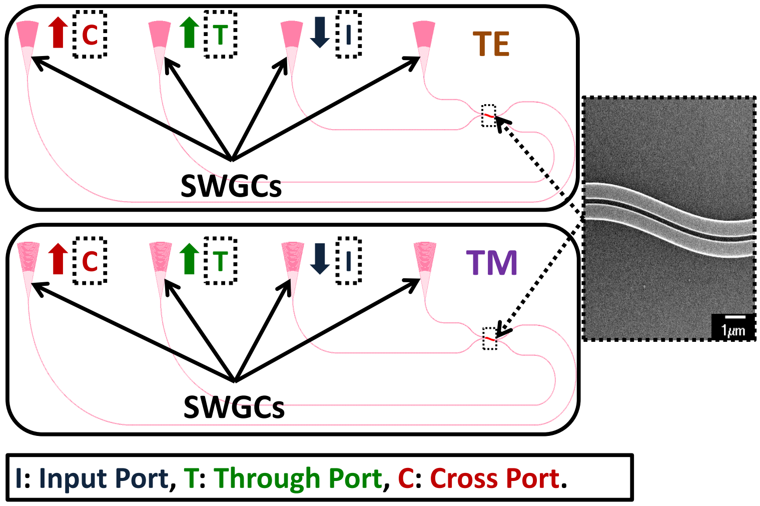

Figure 4.3: Design layouts of the PBSs for TE operation (upper left) and TM operation (lower left) with an SEM image (right) of the sinusoidal symmetric waveguide structure in one of the devices. Adapted with permission from Ref. [1], ©2017 Optical Society of America.

Figure 4.4: Schematic of an SOI Platform.

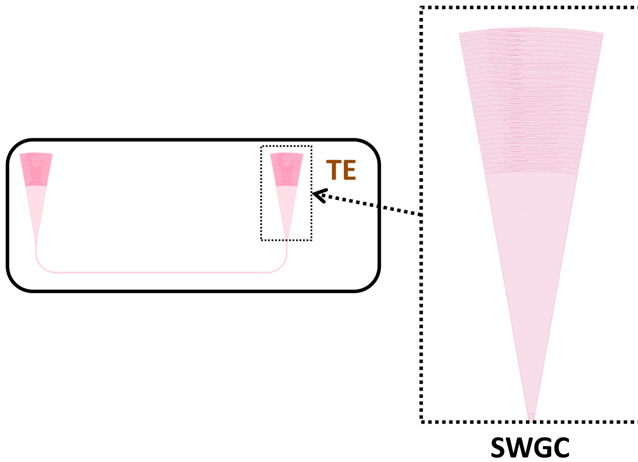

Figure 4.5: Design layout (left) of the TE reference device with a close-up view (right) of one of the TE SWGCs that were used in the TE reference device and the TE sinusoidal AC device.

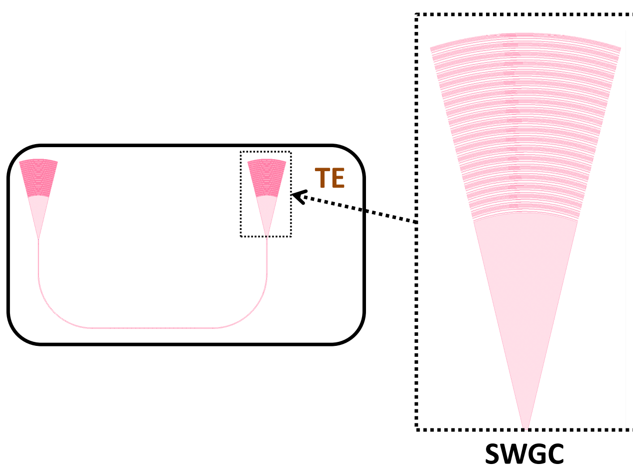

Figure 4.6: Design layout (left) of the TE reference device with a close-up view (right) of one of the TE SWGCs that were used in the TE reference device and the PBS for TE operation.

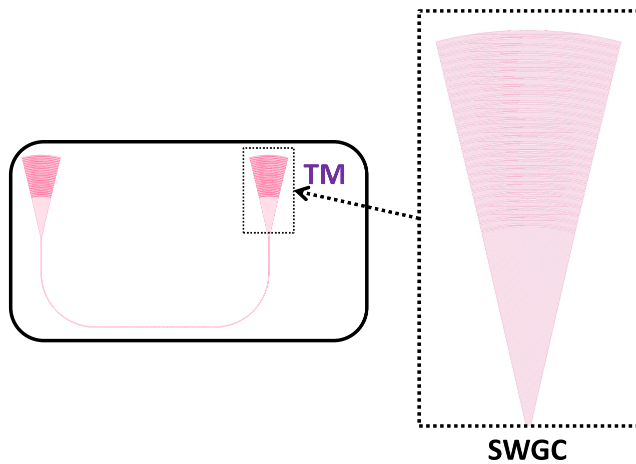

Figure 4.7: Design layout (left) of the TM reference device with a close-up view (right) of one of the TM SWGCs that were used in the TM reference device, the TM sinusoidal AC device, and the PBS for TM operation.

AC device and the PBS for TM operation, as well as one of the TM SWGCs that were used in these devices.

The fabricated test devices were measured using an automated optical fibre probe station in our lab (see Ref. [49]). As shown in Fig. 4.8, the probe station consists of a laser and detector mainframe (Agilent 8164A), a tunable laser source module (Agilent 81682A), a dual optical power sensor module (Agilent 81635A), polarization-maintaining fibres (from PLC Connections, LLC. and OZ Optics, Ltd.), an optical fibre array (from PLC Connections, LLC.), a motor controller (Thorlabs BBD203), a temperature controller (Standford Research Systems LDC501), a metallic stage, a microscope camera (from Tucsen Photonics Co., Ltd.), a microscope lamp (from AmScope/United Scope, LLC.), a desktop computer, and an optical table (Newport RS4000). Since thermal stability is essential for consistent opti-

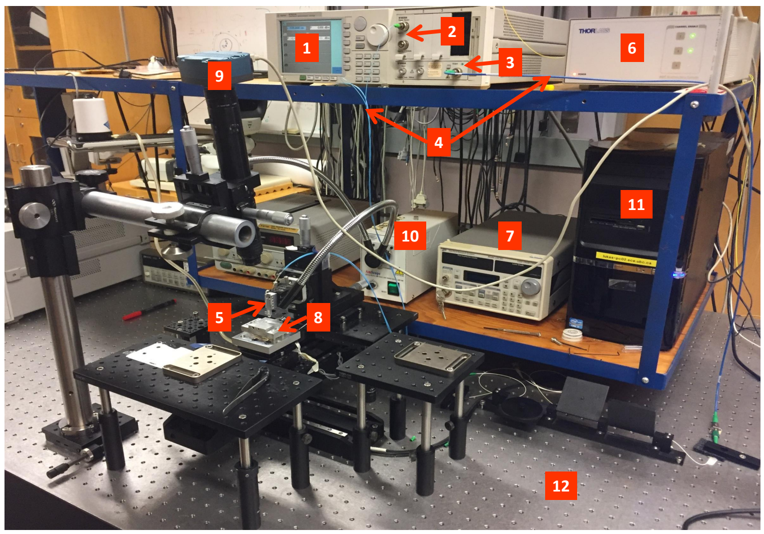

Figure 4.8: Automated optical fibre probe station: 1. Agilent 8164A measurement system; 2. Agilent 81635A dual optical power sensors; 3. Agilent 81682A tunable laser source; 4. PLC Connections and OZ Optics polarization-maintaining fibres; 5. PLC Connections optical fibre array; 6. Thorlabs BBD203 motor controller; 7. Standford Research Systems LDC501 temperature controller; 8. metallic stage; 9. Tucsen microscope camera; 10. AmScope microscope lamp; 11. desktop computer; 12. Newport RS4000 optical table.

cal measurement, a room temperature of 25 °C was maintained during my measurement using the temperature controller.

4.3 Demonstration

Table 4.1: Design parameters of the TE and TM sinusoidal AC symmetric waveguide pairs and a PBS using a symmetric DC with sinuosidal bends (see Refs. [1, 2]).

Devices	**Parameters**					
	W, nm	H, nm	G, nm	Λ, μm	L, μm	A, nm
TE sinusoidal AC [2]	500	220	200	16.44	32.88	932
TM sinusoidal AC	500	220	600	19.86	39.72	1025
PBS [1]	500	220	200	16.44	8.55	932

The TE and TM sinusoidal AC symmetric waveguide pairs and a PBS using a symmetric DC with sinusoidal bends are demonstrated using the measurement data. The design parameters of those devices are listed in Table 4.1.

4.3.1 Sinusoidal AC Symmetric Waveguide Pair for TE Operation

I measured my TE sinusoidal AC test device (see Fig. 4.1) for TE operation over the C-band (a wavelength range from 1530 nm to 1565 nm) and normalized the measurement data using the TE reference device (see Fig. 4.5). A straight AC asymmetric waveguide pair, which consisted of a 450-nm-wide waveguide and a 550-nm-wide waveguide, was also fabricated and measured.

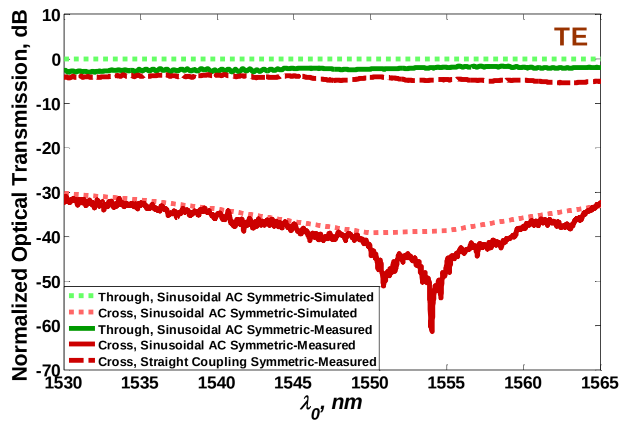

Figure 4.9: Simulated and normalized measured optical transmission spectra for the through and cross ports of the TE sinusoidal AC symmetric waveguide pair as well as normalized measured optical transmission spectrum for the cross port of the equivalent TE straight symmetric DC. Adapted with permission from Ref. [2], ©2015 Optical Society of America.

Table 4.2: Minimum, average, and maximum values of the SRs of both the TE sinusoidal and straight AC devices for TE operation over the C-band (see Ref. [2]).

Devices	**Sinusoidal Symmetric AC**			**Straight Asymmetric AC**		
SR, dB	**Minimum**	**Average**	**Maximum**	**Minimum**	**Average**	**Maximum**
	26.8	38.2	56.5	16.9	17.8	18.6

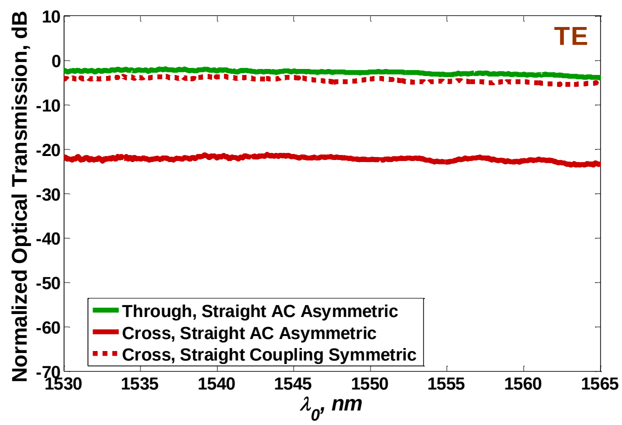

Figure 4.10: Normalized measured optical transmission spectra for the through and cross ports of the TE straight AC asymmetric waveguide pair as well as for the cross port of the equivalent TE straight symmetric DC. Adapted with permission from Ref. [2], ©2015 Optical Society of America.

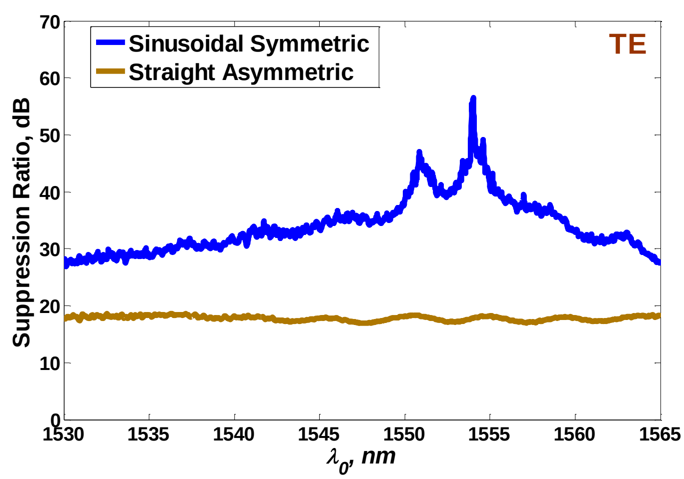

Figure 4.11: SR spectra for both the TE sinusoidal and straight AC devices. Adapted with permission from Ref. [2], ©2015 Optical Society of America.

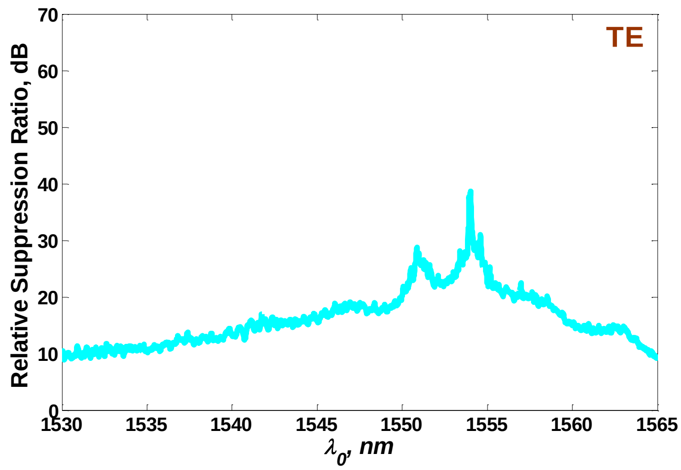

Figure 4.12: Relative SR spectrum of the TE sinusoidal AC device as compared to the equivalent TE straight AC device. Adapted with permission from Ref. [2], ©2015 Optical Society of America.

Each of the two TE AC devices has the same $G = 200$ nm and has the same $L = 32.88$ μm that was chosen to allow for the maximum TE optical power transfer to the cross port of the equivalent TE straight symmetric DC. Figure 4.9 shows the normalized measured optical transmission spectra for both the through and cross ports of the TE sinusoidal AC symmetric waveguide pair as compared to the results from FDTD simulations, and Fig. 4.10 shows the normalized measured optical transmission spectra for both the through and cross ports of the TE straight AC asymmetric waveguide pair. Both of the figures also show the normalized measured optical transmission spectrum for the cross port of the equivalent TE straight symmetric DC.

Each of the AC devices was designed to suppress the optical transmission to the cross port, T^{AC}_{cross}, while the equivalent DC was designed to maximize the optical transmission to the cross port, T^{DC}_{cross}. Therefore, the T^{DC}_{cross} can be used as a reference to evaluate the suppression of inter-waveguide crosstalk that is achieved by each of the AC devices, and I define the suppression ratio (SR) for each of the AC devices as:

$$\mathrm{SR} = 10\log_{10}\left(\frac{T^{DC}_{cross}}{T^{AC}_{cross}}\right). \tag{4.1}$$

Figure 4.11 shows the SR spectra of both the TE sinusoidal and straight AC devices for TE operation over the C-band. The minimum, average, and maximum values of the SRs of the two TE AC devices within the C-band are listed in Table 4.2. In order to compare the crosstalk suppression of the sinusoidal AC device with the straight AC device, I also define the relative SR as the ratio (difference in dB) of the SR of the TE sinusoidal AC device to the SR of the TE straight AC device at each λ_0. As shown in Fig. 4.12, the TE sinusoidal AC device has higher relative SR than the TE straight AC device over the C-band. A minimum value of the relative SR is 8.9 dB, an average value of the relative SR is 20.4 dB, and a maximum value of the relative SR is 38.6 dB (see Ref. [2]). Hence, the TE sinusoidal AC symmetric waveguides provide excellent crosstalk suppression over the entire C-band.

4.3.2 Sinusoidal AC Symmetric Waveguide Pair for TM Operation

I measured my TM sinusoidal AC test device (see Fig. 4.2) for TM operation over the C-band and normalized the measurement data using the TM reference device (see Fig. 4.7). A straight AC asymmetric waveguide pair, which consisted of a 450-nm-wide waveguide and a 550-nm-wide waveguide, was also fabricated and measured. Each of the two AC devices has the same $G = 600$ nm and has the same $L = 39.72$ μm that was chosen to allow for

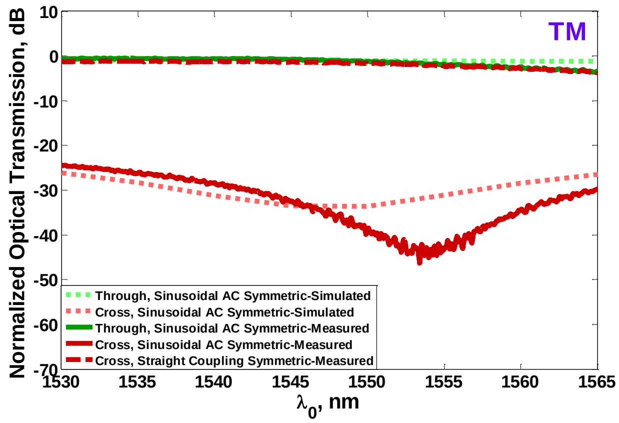

Figure 4.13: Simulated and normalized measured optical transmission spectra for the through and cross ports of the TM sinusoidal AC symmetric waveguide pair as well as normalized measured optical transmission spectrum for the cross port of the equivalent TM straight symmetric DC.

Table 4.3: Minimum, average, and maximum values of the SRs of both the TM sinusoidal and straight AC devices for TM operation over the C-band.

Devices	**Sinusoidal Symmetric**			**Straight Asymmetric**		
SR, dB	**Minimum**	**Average**	**Maximum**	**Minimum**	**Average**	**Maximum**
	23.1	34.9	44.4	28.3	41.1	52.8

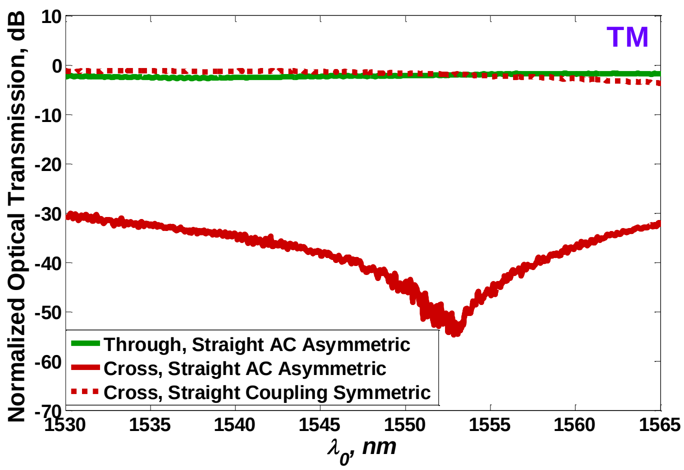

Figure 4.14: Normalized measured optical transmission spectra for the through and cross ports of the TM straight AC asymmetric waveguide pair as well as for the cross port of the equivalent TM straight symmetric DC.

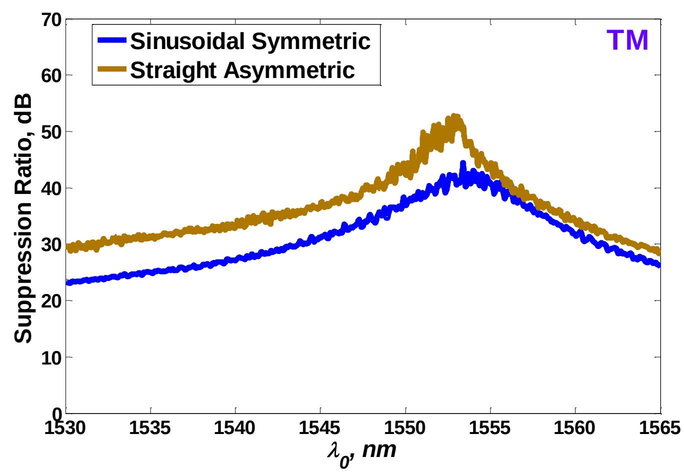

Figure 4.15: SR spectra of both the TM sinusoidal and straight AC devices.

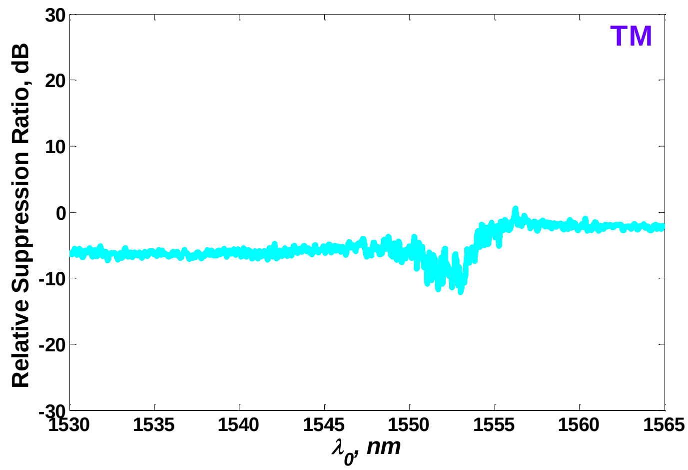

Figure 4.16: Relative SR spectrum of the TM sinusoidal AC device as compared to the equivalent TM straight AC device.

the maximum TM optical power transfer to the cross port of the equivalent TM straight symmetric DC. Figure 4.13 shows the normalized measured optical transmission spectra for both the through and cross ports of the TM sinusoidal AC symmetric waveguide pair as compared to the results from FDTD simulations, and Fig. 4.14 shows the normalized measured optical transmission spectra for the through and cross ports of the TM straight AC asymmetric waveguide pair. Both of the figures also show the normalized measured optical transmission spectrum for the cross port of the equivalent TM straight symmetric DC.

Referring to Eq. 4.1, the SR for each of the TM AC devices can be calculated. Figure 4.15 shows the SR spectra of both the TM sinusoidal and straight AC devices for TM operation over the C-band. The minimum, average, and maximum values of the SRs of the two TM AC devices within the C-band are listed in Table 4.3. Even though the TM sinusoidal AC device has lower relative SR than the TM straight AC device over the C-band, the TM sinusoidal AC symmetric waveguides still provide a large crosstalk suppression over the C-band (see Fig. 4.16).

4.3.3 PBS Using a Symmetric DC with Sinusoidal Bends

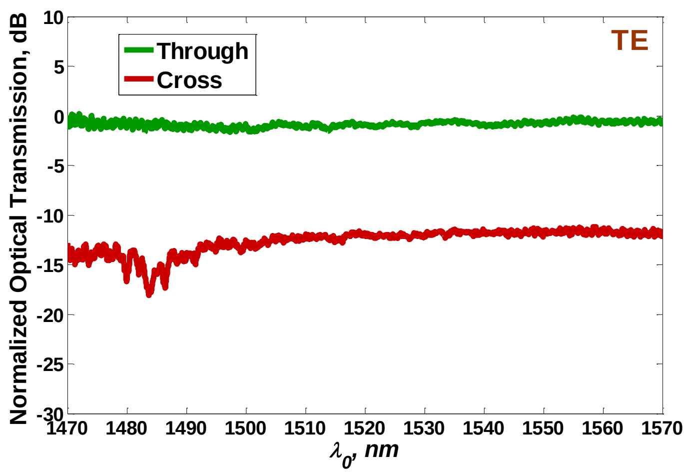

Figure 4.17: Normalized measured optical transmission spectra of the through and cross ports of the PBS for TE operation. Adapted with permission from Ref. [1], ©2017 Optical Society of America.

I measured the test devices of my PBSs (see Fig. 4.3) for both TE operation and TM operation over a wavelength range from 1470 nm to 1570 nm and normalized the measurement data using the TE and TM reference devices (see Figs. 4.6 and 4.7), respectively. Figures 4.17 and 4.18 show the normalized measured optical transmission spectra for the through and cross ports for both TE operation and TM operation. The average excess losses

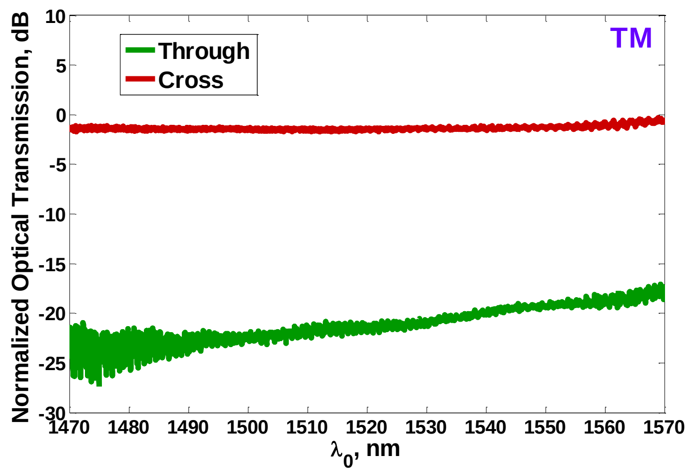

Figure 4.18: Normalized measured optical transmission spectra of the through and cross ports of the PBS for TM operation. Adapted with permission from Ref. [1], ©2017 Optical Society of America..

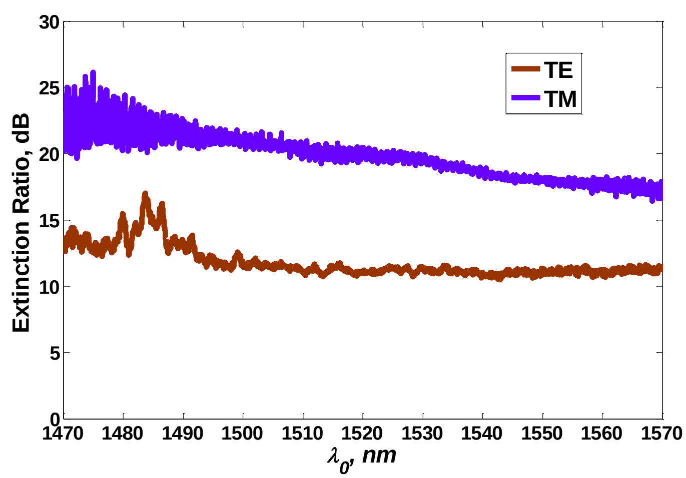

Figure 4.19: ER spectra for both the TE and TM modes. Adapted with permission from Ref. [1], ©2017 Optical Society of America.

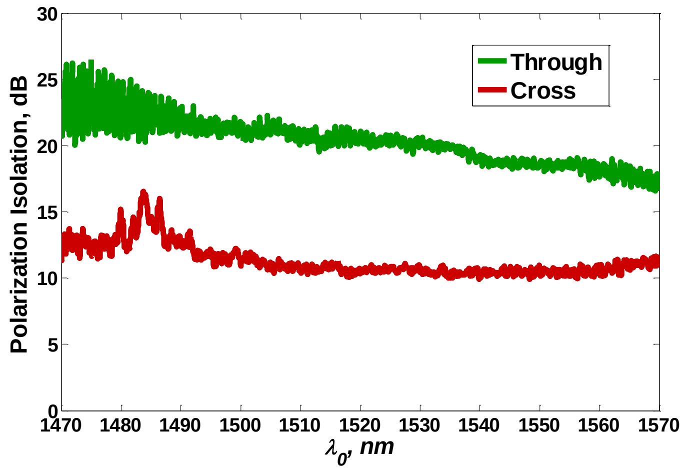

Figure 4.20: PI spectra for both the through and cross ports. Adapted with permission from Ref. [1], ©2017 Optical Society of America.

Table 4.4: Minimum, average, and maximum values of the ERs and PIs of the PBS for both TE operation and TM operation over a wavelength range from 1470 nm to 1570 nm. Adapted with permission from Ref. [1], ©2017 Optical Society of America.

Modes	**TE**			**TM**		
ER, dB	**Minimum**	**Average**	**Maximum**	**Minimum**	**Average**	**Maximum**
	10.5	12.0	17.0	16.4	20.1	26.1
Ports	**Through**			**Cross**		
PI, dB	**Minimum**	**Average**	**Maximum**	**Minimum**	**Average**	**Maximum**
	16.6	20.6	26.5	9.9	11.5	16.5

of the PBS are 0.84 dB for TE operation and 1.33 dB for TM operation (see Ref. [1]).

In my PBS, the $T^{TE}_{through}$ and T^{TE}_{cross} are TE optical transmissions to the through and cross ports, respectively, and the $T^{TM}_{through}$ and T^{TM}_{cross} are TM optical transmissions to the through and cross ports, also respectively. As shown in Figs. 4.17 and 4.18, the $T^{TE}_{through}$ is high as compared to the T^{TE}_{cross} and $T^{TM}_{through}$, while the T^{TM}_{cross} is high as compared to the $T^{TM}_{through}$ and T^{TE}_{cross}. Hence, the extinction ratios (ERs) between the through and cross ports for the TE and TM modes, ER^{TE} and ER^{TM}, respectively, are defined as in Ref. [40]:

$$\mathrm{ER}^{TE} = 10\log_{10}\left(\frac{T^{TE}_{through}}{T^{TE}_{cross}}\right), \tag{4.2a}$$

and

$$\mathrm{ER}^{TM} = 10\log_{10}\left(\frac{T^{TM}_{cross}}{T^{TM}_{through}}\right), \tag{4.2b}$$

which indicate how much TE optical power is transmitted to the through port as compared to the cross port and how much TM optical power is transmitted to the cross port as compared to the through port, respectively. The polarization isolations (PIs) between the TE and TM modes for the through and cross ports, $\mathrm{PI}_{through}$ and PI_{cross}, respectively, are defined as in Ref. [40]:

$$\mathrm{PI}_{through} = 10\log_{10}\left(\frac{T^{TE}_{through}}{T^{TM}_{through}}\right), \tag{4.3a}$$

and

$$\mathrm{PI}_{cross} = 10\log_{10}\left(\frac{T^{TM}_{cross}}{T^{TE}_{cross}}\right), \tag{4.3b}$$

which indicate how well the TE mode is isolated from the TM mode at the through port and how well the TM mode is isolated from the TE mode at the cross port, respectively. Figures. 4.19 and 4.20 show the ER and

PI spectra of the PBS over a wavelength range from 1470 nm to 1570 nm. The minimum, average, and maximum values of the ERs and PIs within the demonstrated wavelength range are listed in Table 4.4. As shown in Figs. 4.19 and 4.20 and Table 4.4, the PBS has broadband performance for both TE operation and TM operation.

4.4 Summary

In this chapter, the sinusoidal AC symmetric waveguide pairs and a PBS using a symmetric DC with sinusoidal bends were demonstrated for TE and/or TM operation on an SOI platform. The fabrication and measurement of the test devices were also described. Each of the sinusoidal AC devices was compared with the straight coupling and AC devices, which had the same gap width and coupler length. The performance of the PBS was also evaluated for both the TE and TM modes.

Chapter 5

Summary, Conclusions, and Suggestions for Future Work

5.1 Summary

I have designed, simulated, analyzed, and demonstrated the TE and TM sinusoidal AC symmetric waveguide pairs and a PBS using a symmetric DC with sinusoidal bends in this thesis. Using the supermodes of a symmetric two-waveguide structure, I derived the optical transmission of a symmetric DC. Using the coupled modes of individual waveguides in the DC, I derived the optical transmission of each waveguide in the device. Based on the analyses for the supermodes and local normal modes of the symmetric DC, I derived the design parameters of sinusoidal bends that suppressed the optical power exchange between a pair of symmetric waveguides.

Using the FDE solver, I simulated the optical modes of single-waveguide and two-waveguide structures and obtained their characterization data for both the TE and TM modes. Then, using the characterization data, I designed the coupling and AC devices, each for TE or TM operation. The TM modes were more sensitive to the bending losses than the TE modes. Therefore, using the FDTD solver, I simulated straight and sinusoidal symmetric devices that had different gap widths and chose an appropriate gap width for the TM sinusoidal AC device. Using the FDTD solver, I optimized the design parameters of the coupling and AC devices and simulated the devices, each for TE or TM operation.

I also designed a PBS using a symmetric DC with sinusoidal bends. The sinusoidal bends suppressed the optical power exchange between the waveguides for TE operation and can still allowed for the maximum optical power transfer to an adjacent waveguide for TM operation. While a sinusoidal AC device was designed to suppress either TE or TM optical power exchange between the waveguides, the PBS was designed to split the TE and TM modes into two output waveguides. I also derived and calculated the modal dispersions of the sinusoidally-bent symmetric DC, which was used in the PBS, and the modal dispersions of the equivalent straight symmetric DC. Then, I compared the wavelength dependencies of the sinusoidally-bent symmetric DC and the wavelength dependencies of the equivalent straight symmetric DC for both the TE and TM modes according to their modal dispersions. Using the FDTD solver, I optimized the design parameters of the PBS and simulated the device for both TE operation and TM operation.

I created the mask layouts of the test devices for fabrication. I also added straight symmetric DCs and straight AC asymmetric waveguide pairs that had the same gap widths and coupler lengths as the sinusoidal AC devices, each for TE or TM operation, to the mask layouts. The test devices were fabricated using E-Beam lithography at the University of Washington and measured using an automatic probe station in our lab. The TE sinusoidal AC symmetric waveguide pair, which had a gap width of 200 nm, had an average crosstalk SR of 38.2 dB and an average improvement in crosstalk SR of 20.4 dB, as compared to the equivalent TE straight AC asymmetric waveguide pair, over the entire C-band. The TM sinusoidal AC symmetric waveguide pair, which had a gap width of 600 nm, had an average crosstalk SR of 34.9 dB over the entire C-band. The PBS, which had a small coupler length of 8.55 μm, had an average ER of 12.0 dB for the TE mode and an average ER of 20.1 dB for the TM mode and had an average PI of 20.6 dB for the through port and an average PI of 11.5 dB for the cross port over a wavelength range from 1470 nm to 1570 nm, which covered the entire C-band.

5.2 Conclusions

In conclusion, I have demonstrated the TE and TM sinusoidal AC waveguide pairs and a PBS using a symmetric DC with sinusoidal bends an SOI platform. My sinusoidal AC symmetric waveguides have large suppression of optical power exchange between the waveguides over the entire C-band. Hence, the sinusoidal waveguides can be used to design compact AC routing waveguides and dense waveguide buses. My PBS has a small coupler length and shows a broad operational bandwidth for both TE operation and TM operation. Hence, the device can be used to separate/combine the TE and TM modes in polarization diversity systems. All of my devices were easy to fabricate and compatible with CMOS technologies.

5.3 Suggestions for Future Works

As shown in Figs. 3.11a, 3.11b, 3.22d, and 3.26b in Chapter 3, small amounts of crosstalk still occurs between the waveguides over half of the bending period. Since the cross-over length is proportional to the gap width of a straight symmetric DC, larger gap widths can be used to design sinusoidal AC symmetric waveguides to achieve larger crosstalk suppression. The bifurcating branches that were used in the AC devices can be further optimized to eliminate the crosstalk that occurs within the branches. Asymmetric waveguides can also be used with sinusoidal bends to enhance crosstalk suppression.

As shown in Fig. 4.20, my PBS has a relatively low PI for the cross port. However, the device is sufficiently compact to allow for several devices to be connected in series in order to obtain better broadband performance than other published broadband PBSs that were based on DCs (see Ref. [1]). Since the PBS is based on the TE sinusoidal AC symmetric waveguide pair, the suggestions for improvements of the sinusoidal AC waveguides above also apply to the improvements of the PBS. Moreover, the operational bandwidth of my PBS is limited by the operational bandwidth of the SWGCs that were used in the test device, and, thus, edge couplers can be used for the PBS to achieve a wider measurable wavelength range than the SWGCs.

There are many potential applications of my sinusoidal AC symmetric waveguides. The sinusoidally-bent AC symmetric waveguide pair can be used to design polarization rotators and splitters, which have been demonstrated using straight and circularly-bent asymmetric waveguides on an SOI platform in Refs. [50, 51]. It has been shown in Chapter 3 that the sinusoidal bends reduced the wavelength dependence of a symmetric DC with sinusoidal bends as compared to an equivalent straight symmetric DC. Therefore, the sinusoidally-bent waveguide pair can also be used to design broadband DCs, which have been proposed and demonstrated using sinusoidally-bent symmetric waveguides on a titanium lithium-niobate platform in Ref. [52] and using circularly-bent symmetric waveguides on an SOI platform in Ref. [53]. Moreover, the optical propagation in a symmetric DC with sinusoidal bends can also be analyzed using a conformal transformation technique as in Refs. [54, 55].

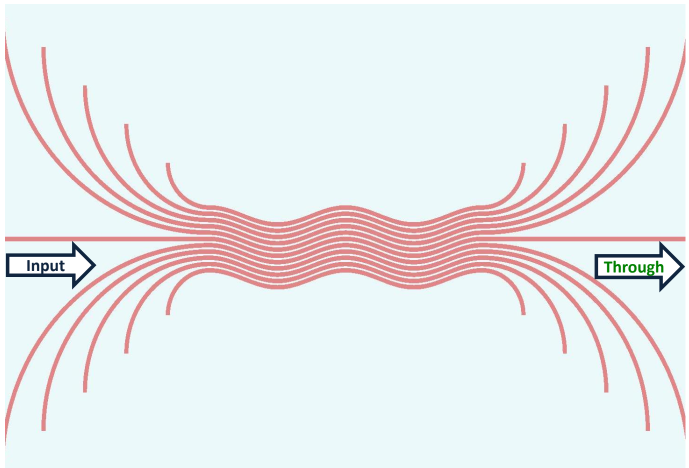

Figure 5.1: Top view of a TE sinusoidal AC symmetric SOI waveguide array, which has $G = 200$ nm.

In addition, multiple sinusoidally-bent symmetric waveguides (see Figs. 5.1 and 5.2) can be used for various applications, such as dense AC waveguide buses and mode-division and polarization-division demultiplexer/multiplexer, which have been demonstrated using straight asymmetric and circularly-bent symmetric waveguides on an SOI platform in Refs. [25, 56, 57]. The sinusoidally-bent symmetric waveguide array can also be used to control the optical propagation in photonic lattices on an SOI platform as suggested in Refs. [58–60]. The sinusoidal AC symmetric waveguides can also be used to design active and thermal optical switches, which have been demonstrated using sinusoidal symmetric waveguides on a titanium lithium-niobate platform as in Ref. [23] and using straight asymmetric waveguides an SOI platform in Ref. [61].

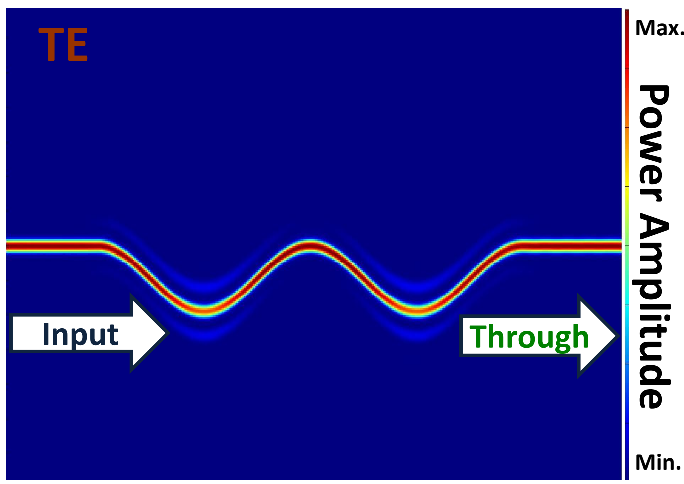

Figure 5.2: Simulated 2-D power distribution profile for the operation at $\lambda_0 = 1550$ nm of the TE sinusoidal AC waveguide array, which has $G = 200$ nm, when a fundamental TE mode is launched into the waveguide in the middle of the array.

Bibliography

[1] Fan Zhang, Han Yun, Yun Wang, Zeqin Lu, Lukas Chrostowski, and Nicolas A. F. Jaeger. Compact broadband polarization beam splitter using a symmetric directional coupler with sinusoidal bends. Optics Letters, 42(2):235–238, Optical Society of America, 2017.

[2] Fan Zhang, Han Yun, Valentina Donzella, Zeqin Lu, Yun Wang, Zhitian Chen, Lukas Chrostowski, and Nicolas A. F. Jaeger. Sinusoidal anti-coupling SOI strip waveguides. In CLEO: Science and Innovations, pages SM1I–7. Optical Society of America, 2015.

[3] Richard Soref. Mid-infrared photonics in silicon and germanium. Nature Photonics, 4(8):495–497, 2010.

[4] Luxtera, Inc. http://www.luxtera.com/luxtera/products (2017-01-02).

[5] Finisar Corporation. https://www.finisar.com/optical-transceivers (2017-01-02).

[6] Cisco Systems, Inc. http://www.cisco.com/c/en/us/solutions/service-provider/100-gigabit-solution/index.html (2017-01-02).

[7] Intel Corporation. http://www.intel.com/content/www/us/en/architecture-and-technology/silicon-photonics/silicon-photonics-overview.html (2017-01-02).

[8] Chen Sun, Mark T. Wade, Yunsup Lee, Jason S. Orcutt, Luca Alloatti, Michael S. Georgas, Andrew S. Waterman, Jeffrey M. Shainline, Rimas R. Avizienis, Sen Lin, et al. Single-chip microprocessor that communicates directly using light. Nature, 528(7583):534–538, 2015.

[9] Siming Chen, Wei Li, Jiang Wu, Qi Jiang, Mingchu Tang, Samuel Shutts, Stella N. Elliott, Angela Sobiesierski, Alwyn J. Seeds, Ian Ross, et al. Electrically pumped continuous-wave III–V quantum dot lasers on silicon. Nature Photonics, 2016.

[10] Chi Xiong, Douglas M. Gill, Jonathan E. Proesel, Jason S. Orcutt, Wilfried Haensch, and William M. J. Green. Monolithic 56 Gb/s silicon photonic pulse-amplitude modulation transmitter. Optica, 3(10):1060–1065, 2016.

[11] Pieter Dumon, Wim Bogaerts, Vincent Wiaux, Johan Wouters, Stephan Beckx, Joris Van Campenhout, Dirk Taillaert, Bert Luyssaert, Peter Bienstman, Dries Van Thourhout, et al. Low-loss SOI photonic wires and ring resonators fabricated with deep UV lithography. IEEE Photonics Technology Letters, 16(5):1328–1330, 2004.

[12] Kimmo Solehmainen, Markku Kapulainen, Mikko Harjanne, and Timo Aalto. Adiabatic and multimode interference couplers on silicon-on-insulator. IEEE Photonics Technology Letters, 18(21):2287–2289, 2006.

[13] Yi Zhang, Shuyu Yang, Andy Eujin Lim, Guoqiang Lo, Christophe Galland, Tom Baehr Jones, and Michael Hochberg. A compact and low loss Y-junction for submicron silicon waveguide. Optics Express, 21(1):1310–1316, 2013.

[14] Zeqin Lu, Han Yun, Yun Wang, Zhitian Chen, Fan Zhang, Nicolas A. F. Jaeger, and Lukas Chrostowski. Broadband silicon photonic directional coupler using asymmetric-waveguide based phase control. Optics Express, 23(3):3795–3808, 2015.

[15] Zhitian Chen, Jonas Flueckiger, Xu Wang, Fan Zhang, Han Yun, Zeqin Lu, Michael Caverley, Yun Wang, Nicolas A. F. Jaeger, and Lukas Chrostowski. Spiral Bragg grating waveguides for TM mode silicon photonics. Optics Express, 23(19):25295–25307, 2015.

[16] Han Yun, Yun Wang, Fan Zhang, Zeqin Lu, Stephen Lin, Lukas Chrostowski, and Nicolas A. F. Jaeger. Broadband 2$\times$ 2 adiabatic 3 dB coupler using silicon-on-insulator sub-wavelength grating waveguides. Optics Letters, 41(13):3041–3044, 2016.

[17] Qianfan Xu, Bradley Schmidt, Sameer Pradhan, and Michal Lipson. Micrometre-scale silicon electro-optic modulator. Nature, 435(7040):325–327, 2005.

[18] Donghwan Ahn, Chingyin Hong, Jifeng Liu, Wojciech Giziewicz, Mark Beals, Lionel C. Kimerling, Jurgen Michel, Jian Chen, and Franz X. Kärtner. High performance, waveguide integrated Ge photodetectors. Optics Express, 15(7):3916–3921, 2007.

[19] Rodolfo E. Camacho Aguilera, Yan Cai, Neil Patel, Jonathan T. Bessette, Marco Romagnoli, Lionel C. Kimerling, and Jurgen Michel. An electrically pumped germanium laser. Optics Express, 20(10):11316–11320, 2012.

[20] Stefano Longhi, Davide Janner, Marcello Marano, and Paolo Laporta.

Quantum-mechanical analogy of beam propagation in waveguides with a bent axis: Dynamic-mode stabilization and radiation-loss suppression. Physical Review E, 67(3):036601, 2003.

[21] Stefano Longhi. Coherent destruction of tunneling in waveguide directional couplers. Physical Review A, 71(6):065801, 2005.

[22] Giuseppe Della Valle, Marco Ornigotti, Elena Cianci, Vittorio Foglietti, Paolo Laporta, and Stefano Longhi. Visualization of coherent destruction of tunneling in an optical double well system. Physical Review Letters, 98(26):263601, 2007.

[23] Nicolas Grossard, Jérôme Hauden, and Henri Porte. Periodic anticoupling structures for parallel optical waveguides on $LiNbO_3$. Journal of Lightwave Technology, 29(16):2489–2495, 2011.

[24] Valentina Donzella, Sahba Talebi Fard, and Lukas Chrostowski. Study of waveguide crosstalk in silicon photonics integrated circuits. In Photonics North 2013, pages 89150Z–89150Z. International Society for Optics and Photonics, 2013.

[25] Weiwei Song, Robert Gatdula, Siamak Abbaslou, Ming Lu, Aaron Stein, Warren Y. C. Lai, J. Provine, R. Fabian W. Pease, Demetrios N. Christodoulides, and Wei Jiang. High-density waveguide superlattices with low crosstalk. Nature Communications, 6, 2015.

[26] X. Sun, M. Z. Alam, J. S. Aitchison, and M. Mojahedi. Compact and broadband polarization beam splitter based on a silicon nitride augmented low-index guiding structure. Optics Letters, 41(1):163–166, 2016.

[27] Hiroshi Fukuda, Koji Yamada, Tai Tsuchizawa, Toshifumi Watanabe, Hiroyuki Shinojima, and Seiichi Itabashi. Ultrasmall polarization splitter based on silicon wire waveguides. Optics Express, 14(25):12401–12408, 2006.

[28] Winnie N. Ye, Danxia Xu, Siegfried Janz, Philip Waldron, Pavel Cheben, and N. Garry Tarr. Passive broadband silicon-on-insulator polarization splitter. Optics Letters, 32(11):1492–1494, 2007.

[29] Shiyun Lin, Juejun Hu, and Kenneth B. Crozier. Ultracompact, broadband slot waveguide polarization splitter. Applied Physics Letters, 98(15):151101, 2011.

[30] Isa Kiyat, Atilla Aydinli, and Nadir Dagli. A compact silicon-on-insulator polarization splitter. IEEE Photonics Technology Letters, 17(1):100–102, 2005.

[31] T. K. Liang and H. K. Tsang. Integrated polarization beam splitter in high index contrast silicon-on-insulator waveguides. IEEE Photonics Technology Letters, 17(2):393–395, 2005.

[32] Xianyu Ao, Liu Liu, Lech Wosinski, and Sailing He. Polarization beam splitter based on a two-dimensional photonic crystal of pillar type. Applied Physics Letters, 89(17):171115, 2006.

[33] Byungki Yang, Sangyung Shin, and Daming Zhang. Ultrashort polarization splitter using two-mode interference in silicon photonic wires. IEEE Photonics Technology Letters, 21(7):432–434, 2009.

[34] A. Hosseini, S. Rahimi, X. Xu, D. Kwong, J. Covey, and R. T. Chen.

Ultracompact and fabrication-tolerant integrated polarization splitter. Optics Letters, 36(20):4047–4049, 2011.

[35] Daoxin Dai, Zhi Wang, Jon Peters, and John E. Bowers. Compact polarization beam splitter using an asymmetrical Mach-Zehnder interferometer based on silicon-on-insulator waveguides. IEEE Photonics Technology Letters, 24(8):673–675, 2012.

[36] Jian Wang, Di Liang, Yongbo Tang, Daoxin Dai, and John E. Bowers. Realization of an ultra-short silicon polarization beam splitter with an asymmetrical bent directional coupler. Optics Letters, 38(1):4–6, 2013.

[37] Yawen Huang, Zhao Tu, Huaxiang Yi, Yanping Li, Xingjun Wang, and Weiwei Hu. High extinction ratio polarization beam splitter with multimode interference coupler on SOI. Optics Communications, 307:46–49, 2013.

[38] Mei Yin, Wei Yang, Yanping Li, Xingjun Wang, and Hongbin Li. CMOS-compatible and fabrication-tolerant MMI-based polarization beam splitter. Optics Communications, 335:48–52, 2015.

[39] Bing Shen, Peng Wang, Randy Polson, and Rajesh Menon. An integrated-nanophotonics polarization beamsplitter with 2.4× 2.4 μm^2 footprint. Nature Photonics, 9(6):378–382, 2015.

[40] Zeqin Lu, Yun Wang, Fan Zhang, Nicolas A. F. Jaeger, and Lukas Chrostowski. Wideband silicon photonic polarization beamsplitter based on point-symmetric cascaded broadband couplers. Optics Express, 23(23):29413–29422, 2015.

[41] Amnon Yariv. Coupled-mode theory for guided-wave optics. IEEE Journal of Quantum Electronics, 9(9):919–933, 1973.

[42] Emanuel Marom, O. Ramer, and S. Ruschin. Relation between normal-mode and coupled-mode analyses of parallel waveguides. IEEE Journal of Quantum Electronics, 20(12):1311–1319, 1984.

[43] Jose M. Gomez Llorente and Jesús Plata. Tunneling control in a two-level system. Physical Review A, 45(10):R6958, 1992.

[44] Zhaoming Zhu and Thomas G. Brown. Full-vectorial finite-difference analysis of microstructured optical fibers. Optics Express, 10(17):853–864, 2002.

[45] Kane Yee. Numerical solution of initial boundary value problems involving maxwell's equations in isotropic media. IEEE Transactions on Antennas and Propagation, 14(3):302–307, 1966.

[46] Yurii A. Vlasov and Sharee J. McNab. Losses in single-mode silicon-on-insulator strip waveguides and bends. Optics Express, 12(8):1622–1631, 2004.

[47] Yun Wang, Xu Wang, Jonas Flueckiger, Han Yun, Wei Shi, Richard J. Bojko, Nicolas A. F. Jaeger, and Lukas Chrostowski. Focusing sub-wavelength grating couplers with low back reflections for rapid prototyping of silicon photonic circuits. Optics Express, 22(17):20652–20662, 2014.

[48] Yun Wang, Han Yun, Zeqin Lu, Richard J. Bojko, Wei Shi, Xu Wang, Jonas Flueckiger, Fan Zhang, Michael Caverley, Nicolas A. F. Jaeger,

and Lukas Chrostowski. Apodized focusing fully etched subwavelength grating couplers. IEEE Photonics Journal, 7(3):1–10, 2015.

[49] L. Chrostowski and M. Hochberg. Silicon Photonics Design. Cambridge University Press, Cambridge , UK, 2015.

[50] Liu Liu, Yunhong Ding, Kresten Yvind, and Jørn M. Hvam. Efficient and compact TE–TM polarization converter built on silicon-on-insulator platform with a simple fabrication process. Optics Letters, 36(7):1059–1061, 2011.

[51] Yong Zhang, Yu He, Xinhong Jiang, Boyu Liu, Ciyuan Qiu, Yikai Su, and Richard A. Soref. Ultra-compact and highly efficient silicon polarization splitter and rotator. APL Photonics, 1(9):091304, 2016.

[52] Ivan L. Garanovich and Andrey A. Sukhorukov. Nonlinear directional coupler for polychromatic light. Optics Letters, 32(5):475–477, 2007.

[53] Pengxin Chen, Sitao Chen, Xiaowei Guan, Yaocheng Shi, and Daoxin Dai. High-order microring resonators with bent couplers for a box-like filter response. Optics Letters, 39(21):6304–6307, 2014.

[54] Mordehai Heiblum and Jay Harris. Analysis of curved optical waveguides by conformal transformation. IEEE Journal of Quantum Electronics, 11(2):75–83, 1975.

[55] S. J. Garth. Modes on a bent optical waveguide. IEE Proceedings J-Optoelectronics, 134(4):221–229, 1987.

[56] Kaixuan Chen, Siya Wang, Sitao Chen, Shipeng Wang, Chenzhao Zhang, Daoxin Dai, and Liu Liu. Experimental demonstration of si-

multaneous mode and polarization-division multiplexing based on silicon densely packed waveguide array. Optics Letters, 40(20):4655–4658, 2015.

[57] Hongnan Xu and Yaocheng Shi. Ultra-broadband 16-channel mode division (de) multiplexer utilizing densely packed bent waveguide arrays. Optics Letters, 41(20):4815–4818, 2016.

[58] Felix Dreisow, Matthias Heinrich, Alexander Szameit, Sven Döring, Stefan Nolte, Andreas Tünnermann, Stephan Fahr, and Falk Lederer. Spectral resolved dynamic localization in curved fs laser written waveguide arrays. Optics Express, 16(5):3474–3483, 2008.

[59] Alexander Szameit, Ivan L. Garanovich, Matthias Heinrich, Andrey A. Sukhorukov, Felix Dreisow, Thomas Pertsch, Stefan Nolte, Andreas Tünnermann, and Yuri S. Kivshar. Polychromatic dynamic localization in curved photonic lattices. Nature Physics, 5(4):271, 2009.

[60] Ivan L. Garanovich, Stefano Longhi, Andrey A. Sukhorukov, and Yuri S. Kivshar. Light propagation and localization in modulated photonic lattices and waveguides. Physics Reports, 518(1):1–79, 2012.

[61] Kyle Murray, Zeqin Lu, Hasitha Jayatilleka, and Lukas Chrostowski. Dense dissimilar waveguide routing for highly efficient thermo-optic switches on silicon. Optics Express, 23(15):19575–19585, 2015.

[62] Mee Koy Chin and Seng Tiong Ho. Design and modeling of waveguide-coupled single-mode microring resonators. Journal of Lightwave Technology, 16(8):1433, 1998.

[63] Nico M. Temme. Special functions: An introduction to the classical functions of mathematical physics. John Wiley & Sons, Hoboken, NJ, USA, 2011.

Appendix A

Derivation of the Propagation Constant Difference of a Sinusoidally-bent Symmetric DC

As discussed in Chapter 2, a symmetric DC consists of a pair of parallel strip waveguides that are separated by a gap of width, G, and have the same width, W, and height, H (see Fig. A.1). In a straight symmetric DC (see Fig. A.2), the 2-D electric field distribution for local normal mode of waveguide core $\boldsymbol{a}$, $\Psi_{a,straight}(x,z)$, can be given as:

$$\Psi_{a,straight}(x,z) = A_{a,straight}(z)\psi_a(x)e^{-j\beta_{wg}z}, \tag{A.1}$$

and the 2-D electric field distribution for local normal mode of waveguide core $\boldsymbol{b}$, $\Psi_{b,straight}(x,z)$, can also be given as:

$$\Psi_{b,straight}(x,z) = A_{b,straight}(z)\psi_b(x)e^{-j\beta_{wg}z}, \tag{A.2}$$

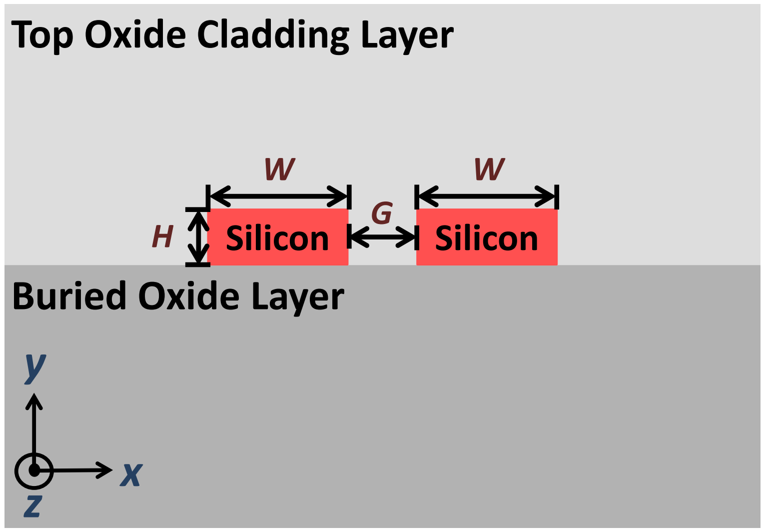

Figure A.1: Cross-sectional view of a symmetric DC on an SOI platform (also Fig. 2.1 in Chapter 2). Adapted with permission from Ref. [1], ©2017 Optical Society of America.

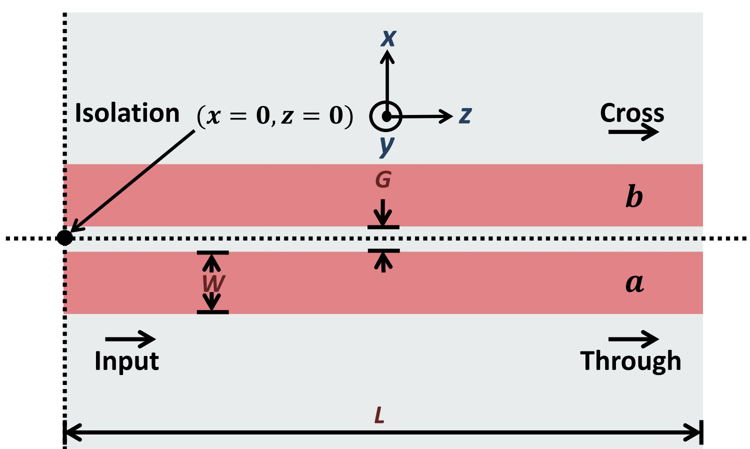

Figure A.2: Top view of a straight symmetric DC (also Fig. 2.3 in Chapter 2).

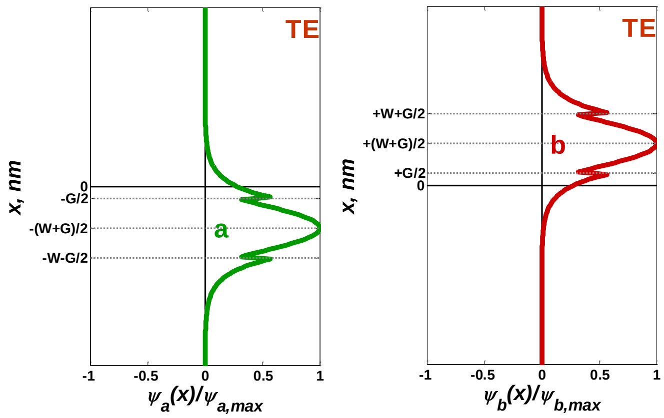

Figure A.3: 1-D normalized transverse field distributions for the TE local normal modes of waveguide cores ***a*** (left) and waveguide core ***b*** (right), $\psi_a(x)$ and $\psi_b(x)$, over their respective maximum values, $\psi_{a,max}$ and $\psi_{b,max}$ (also Fig. 2.6 in Chapter 2).

where $A_{a,straight}(z)$ and $A_{b,straight}(z)$ are their respective z-dependent transverse field amplitudes, $\psi_a(x)$ and $\psi_b(x)$ are their respective 1-D normalized transverse field distributions (see Figs. A.3 and A.4), and β_{wg} is the propagation constant of a straight strip waveguide core with cross-sectional dimensions (W and H). Since $A_{a,straight}(z)$ can be given as:

$$A_{a,straight}(z) = A_M \cos\left(\frac{\Delta\beta_{straight}}{2} z\right), \tag{A.3}$$

and $A_{b,straight}(z)$ can also be given as:

$$A_{b,straight}(z) = -jA_M \sin\left(\frac{\Delta\beta_{straight}}{2} z\right), \tag{A.4}$$

where A_M is the maximum magnitude of both $A_{a,straight}(z)$ and $A_{b,straight}(z)$ along the z-axis, and $\Delta\beta_{straight}$ is the difference in the propagation constants for the even (symmetric) and odd (anti-symmetric) supermodes of

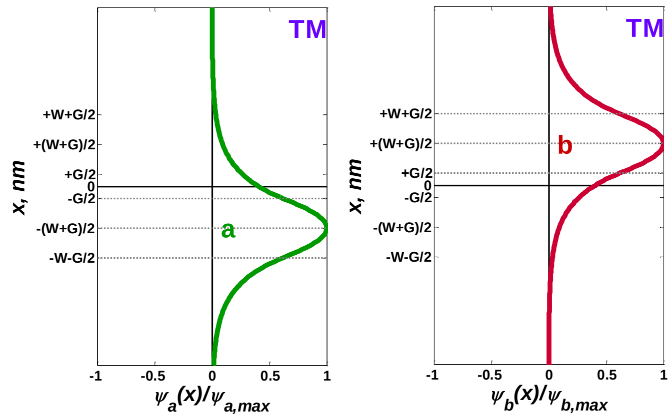

Figure A.4: 1-D normalized transverse field distributions for the TM local normal modes of waveguide core ***a*** (left) and waveguide core ***b*** (right), $\psi_a(x)$ and $\psi_b(x)$, over their respective maximum values, $\psi_{a,max}$ and $\psi_{b,max}$ (also Fig. 2.7 in Chapter 2).

the straight DC. Then, referring to Eqs. A.3 and A.4, the first derivative of $A_{a,straight}(z)$ with respect to z can be solved and represented, in terms of $A_{b,straight}(z)$, as:

$$\frac{\partial A_{a,straight}(z)}{\partial z} = -j\frac{\Delta\beta_{straight}}{2}\left[-jA_M \sin\left(\frac{\Delta\beta_{straight}}{2}z\right)\right] = -j\frac{\Delta\beta_{straight}}{2}A_{b,straight}(z), \tag{A.5}$$

and, also referring to Eqs. A.3 and A.4, the first derivative of $A_{b,straight}(z)$ with respect to z can be solved and represented, in terms of $A_{a,straight}(z)$, as:

$$\frac{\partial A_{b,straight}(z)}{\partial z} = -j\frac{\Delta\beta_{straight}}{2}\left[A_M \cos\left(\frac{\Delta\beta_{straight}}{2}z\right)\right] = -j\frac{\Delta\beta_{straight}}{2}A_{a,straight}(z), \tag{A.6}$$

where both of them show the relations between individual local normal modes of the DC.

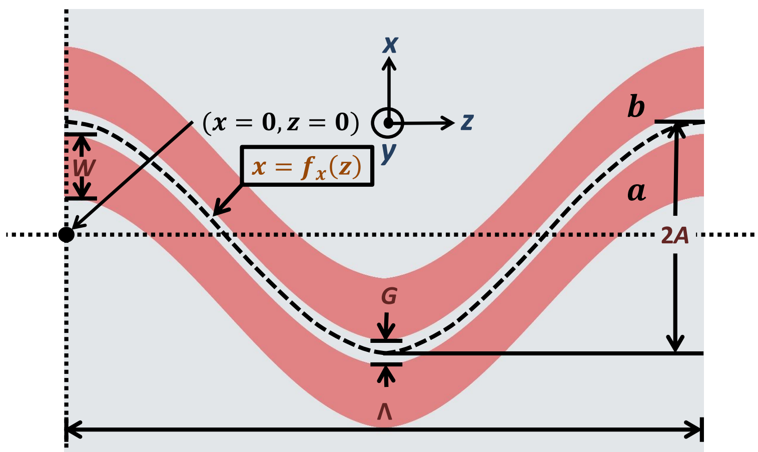

Figure A.5: Top view of a full period of a sinusoidally-bent symmetric DC (also Fig. 2.2 in Chapter 2). Adapted with permission from Ref. [1], ©2017 Optical Society of America.

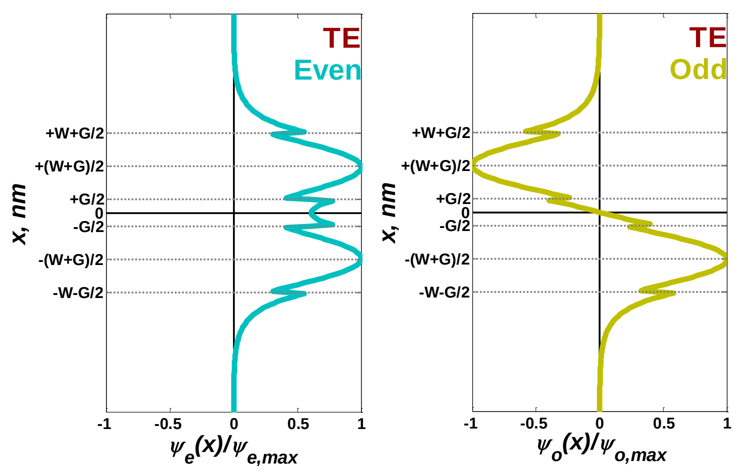

Figure A.6: 1-D normalized transverse field distributions for the even TE supermode (right) and odd TE supermode (right), $\psi_e(x)$ and $\psi_o(x)$, over their respective maximum values, $\psi_{e,max}$ and $\psi_{o,max}$ (also Fig. 2.4 in Chapter 2).

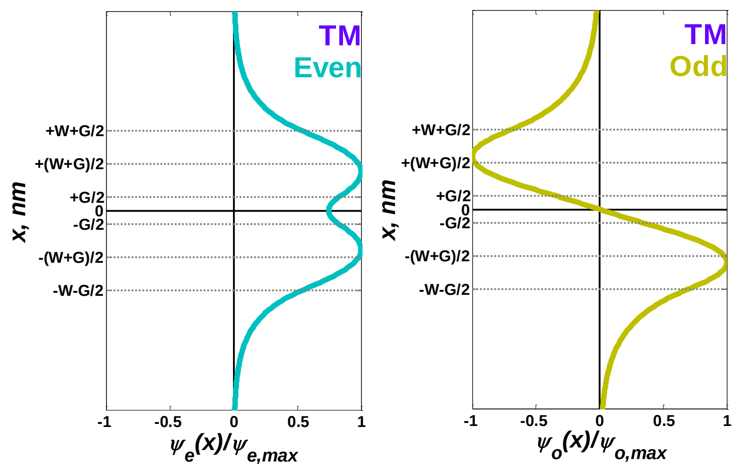

Figure A.7: 1-D normalized transverse field distributions for the even TM supermode (left) and odd TM supermode (right), $\psi_e(x)$ and $\psi_o(x)$, over their respective maximum values, $\psi_{e,max}$ and $\psi_{o,max}$ (also Fig. 2.5 in Chapter 2).

Again, as discussed in Chapter 2, a sinusoidally-bent symmetric DC has the same cross-sectional dimensions, W, H, and G, (see Fig. A.1) and has the same device length as an equivalent straight symmetric DC. Each of the bends is defined as a function of z, $f_x(z)$ (see Fig. A.5), as in Ref. [1]:

$$f_x(z) = A\cos\left(\frac{2\pi}{\Lambda}z\right), \tag{A.7}$$

where A and Λ are the amplitude and period of a sinusoid. According to Refs. [54, 55, 62], the refractive index profiles and electromagnetic field distributions of a bent waveguide are skewed as compared to the ones of a straight waveguide, and, according to Refs. [20, 21, 43], in a symmetric DC with sinusoidal bends, the effects of the sinusoidal bends on the local normal mode of waveguide core $\boldsymbol{a}$ can be approximated using an envelope function,

$F_a(z)$:

$$F_a(z) = e^{+j\beta_{wg}u\frac{\partial f_x(z)}{\partial z}}, \tag{A.8}$$

and the effects of the sinusoidal bends on the local normal mode of waveguide core $\boldsymbol{b}$ can also be approximated using an envelope function, $F_b(z)$:

$$F_b(z) = e^{-j\beta_{wg}u\frac{\partial f_x(z)}{\partial z}}, \tag{A.9}$$

where $u = \frac{\int_{-\infty}^{+\infty} x\psi_e(x)\psi_o(x)dx}{\sqrt{\int_{-\infty}^{+\infty}\psi_e^2(x)dx\int_{-\infty}^{+\infty}\psi_o^2(x)dx}}$, $\frac{\partial f_x(z)}{\partial z} = -\frac{2\pi}{\Lambda}A\sin\left(\frac{2\pi}{\Lambda}z\right)$, $\psi_e(x)$ and $\psi_o(x)$ are the 1-D normalized transverse field distributions for the even and odd supermodes (see Figs. A.6 and A.7).

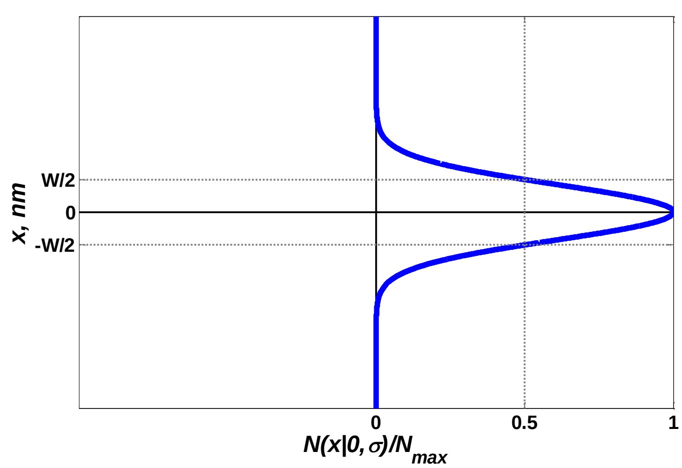

Figure A.8: Probability density function of the 1-D normal distribution, $N(x|0,\sigma)$, which is centered at $x = 0$, over its maximum value, N_{max}.

Here, I will use the 1-D normal distributions to approximate $\psi_a(x)$ and $\psi_b(x)$, and each of the distributions is defined by a probability density function, $N(x|\mu_{lnm},\sigma)$:

$$N(x|\mu_{lnm},\sigma) = \frac{e^{\frac{-(x-\mu_{lnm})^2}{2\sigma^2}}}{\sqrt{2\pi\sigma^2}}, \tag{A.10}$$

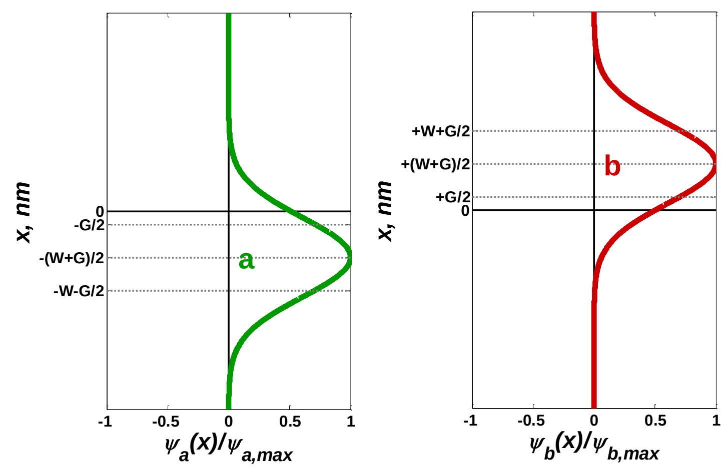

Figure A.9: 1-D normalized transverse field distributions for the approximated $\psi_a(x)$ and $\psi_b(x)$, which are centered at $x = \mu_a = -\frac{W+G}{2}$ and at $x = \mu_b = +\frac{W+G}{2}$, over their $\psi_{a,max}$ and $\psi_{b,max}$, respectively.

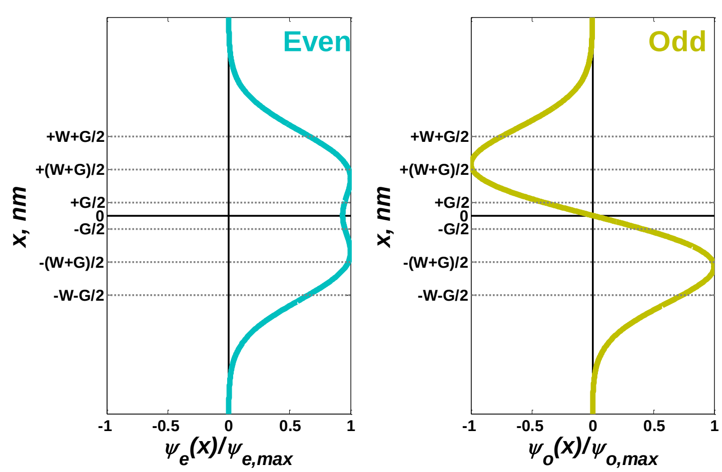

Figure A.10: 1-D normalized transverse field distributions for the approximated $\psi_e(x)$ and $\psi_o(x)$, over their $\psi_{e,max}$ and $\psi_{o,max}$, respetively.

where its mean, μ_{lnm}, determines the location of its center in the x-axis, and its standard deviation, σ, determines its shape. I can set $\sigma = \frac{W}{2\sqrt{2\ln(2)}}$ such that $N(x|\mu_{lnm}, \sigma)$ has a maximum value, N_{max}, and $N(-\frac{W}{2}|0,\sigma) = N(+\frac{W}{2}|0,\sigma) = \frac{N_{max}}{2}$ (see Fig. A.8). Thus, $\psi_a(x)$ can be approximated as:

$$\psi_a(x) \approx \sqrt{N(x|\mu_a, \sigma)} = \frac{e^{\frac{(x-\mu_a)^2}{\sigma^2}}}{\sqrt[4]{2\pi\sigma^2}}, \tag{A.11}$$

and $\psi_b(x)$ can also be approximated as:

$$\psi_b(x) \approx \sqrt{N(x|\mu_b, \sigma)} = \frac{e^{\frac{(x-\mu_b)^2}{\sigma^2}}}{\sqrt[4]{2\pi\sigma^2}}, \tag{A.12}$$

where $\psi_a(x)$ is centered at $x = \mu_a = -\frac{W+G}{2}$, and $\psi_b(x)$ is centered at $x = \mu_b = +\frac{W+G}{2}$ (see Fig. A.9). Since $\mu_a = -\mu_b = -\frac{W+G}{2} = -\mu$, $\psi_e(x)$ can be approximated, in terms of $\psi_a(x)$ and $\psi_b(x)$, as:

$$\psi_e(x) \approx \frac{A_M}{2A_e}[\psi_a(x) + \psi_b(x)] = \frac{A_M}{2A_e}\left[\frac{e^{\frac{(x-\mu)^2}{\sigma^2}} + e^{\frac{(x+\mu)^2}{\sigma^2}}}{\sqrt[4]{2\pi\sigma^2}}\right], \tag{A.13}$$

$\psi_o(x)$ can also be approximated, in terms of $\psi_a(x)$ and $\psi_b(x)$, as:

$$\psi_o(x) \approx \frac{A_M}{2A_o}[\psi_a(x) - \psi_b(x)] = \frac{A_M}{2A_o}\left[\frac{e^{\frac{(x-\mu)^2}{\sigma^2}} - e^{\frac{(x+\mu)^2}{\sigma^2}}}{\sqrt[4]{2\pi\sigma^2}}\right], \tag{A.14}$$

where both of them are shown in Fig. A.10. Subsequently, I can estimate $u \approx -\frac{W+G}{2} = -\mu$.

Therefore, in the sinusoidally-bent symmetric DC, referring to Eqs. A.1, A.3, and A.8, the 2-D electric field distribution for local normal mode of waveguide core $\boldsymbol{a}$, $\Psi_{a,bent}(x,z)$, can be obtained as:

$$\Psi_{a,bent}(x,z) = \Psi_{a,straight}(x,z)F_a(z) \cong \left[A_M \cos\left(\frac{\Delta\beta_{straight}}{2}z\right)e^{-j\beta_{wg}\mu\frac{\partial f_x(z)}{\partial z}}\right]\psi_a(x)e^{-j\beta_{wg}z}, \tag{A.15}$$

and, referring to Eqs. A.2, A.4, and A.9, the 2-D electric field distribution for local normal mode of waveguide core $\boldsymbol{b}$, $\Psi_{b,bent}(x,z)$, can also be obtained as:

$$\Psi_{b,bent}(x,z) = \Psi_{b,straight}(x,z)F_b(z) \cong \left[-jA_M \sin\left(\frac{\Delta\beta_{straight}}{2}z\right)e^{+j\beta_{wg}\mu\frac{\partial f_x(z)}{\partial z}}\right]\psi_b(x)e^{-j\beta_{wg}z}. \tag{A.16}$$

Then, referring to Eq. A.15, the z-dependent transverse field amplitude for local normal mode of waveguide core $\boldsymbol{a}$ of the bent DC, $A_{a,bent}(z)$, can be given, in terms of $A_{a,straight}(z)$, as:

$$A_{a,bent}(z) = \left[A_M \cos\left(\frac{\Delta\beta_{straight}}{2}z\right)\right]e^{-j\beta_{wg}\mu\frac{\partial f_x(z)}{\partial z}} = A_{a,straight}(z)e^{-j\beta_{wg}\mu\frac{\partial f_x(z)}{\partial z}}, \tag{A.17}$$

and, referring to Eq. A.16, the z-dependent transverse field amplitude for local normal mode of waveguide core $\boldsymbol{b}$ of the bent DC, $A_{b,bent}(z)$, can be given, in terms of $A_{b,straight}(z)$, as:

$$A_{b,bent}(z) = \left[-jA_M \sin\left(\frac{\Delta\beta_{straight}}{2}z\right)\right]e^{+j\beta_{wg}\mu\frac{\partial f_x(z)}{\partial z}} = A_{b,straight}(z)e^{+j\beta_{wg}\mu\frac{\partial f_x(z)}{\partial z}}. \tag{A.18}$$

Alternatively, referring to Eq. A.17, $A_{a,straight}(z)$, can be expressed, in terms of $A_{a,bent}(z)$, as:

$$A_{a,straight}(z) = A_{a,bent}(z)e^{+j\beta_{wg}\mu\frac{\partial f_x(z)}{\partial z}}, \tag{A.19}$$

and, referring to Eq. A.18, $A_{b,straight}(z)$ can be expressed, in terms of $A_{b,bent}(z)$, as:

$$A_{b,straight}(z) = A_{b,bent}(z)e^{-j\beta_{wg}\mu\frac{\partial f_x(z)}{\partial z}}. \tag{A.20}$$

Thus, referring to Eq. A.17, the first derivative of $A_{a,bent}(z)$ with respect to z can be solved and represented, in terms of $A_{a,straight}(z)$, as:

$$\frac{\partial A_{a,bent}(z)}{\partial z} = \left[\frac{\partial A_{a,straight}(z)}{\partial z} - j\mu\beta_{wg}C(z)A_{a,straight}(z)\right]e^{-j\mu\beta_{wg}\frac{\partial f_x(z)}{\partial z}}, \tag{A.21}$$

and, referring to Eq. A.18, the first derivative of $A_{b,bent}(z)$ with respect to z can be solved and represented, in terms of $A_{b,straight}(z)$, as:

$$\frac{\partial A_{b,bent}(z)}{\partial z} = \left[\frac{\partial A_{b,straight}(z)}{\partial z} + j\mu\beta_{wg}C(z)A_{b,straight}(z)\right]e^{+j\mu\beta_{wg}\frac{\partial f_x(z)}{\partial z}}, \tag{A.22}$$

where $C(z) = \frac{\partial^2 f_x(z)}{\partial z^2} = \frac{4\pi^2}{\Lambda^2}A\cos\left(\frac{2\pi}{\Lambda}z\right)$ is the curvature of $f_x(z)$.

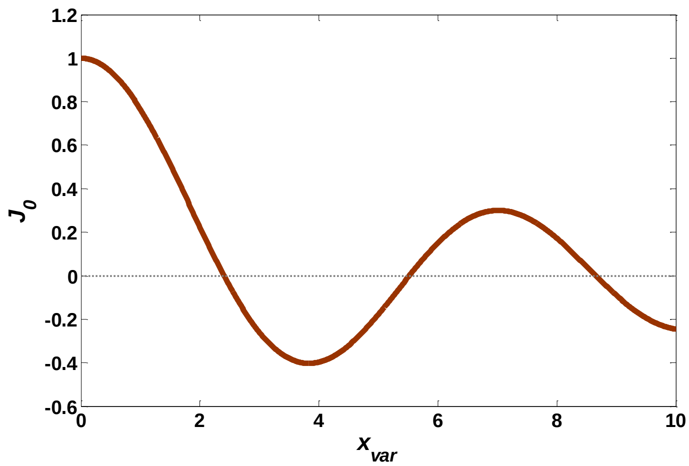

Figure A.11: Bessel function of the first kind of order 0 with respect to a variable, x_{var}, ranging from 0 to 10.

Since $C(z) \approx 0$ over a Λ that is much larger than the A of the sinusoidal bends, referring to Eq. A.21, $\frac{\partial A_{a,bent}(z)}{\partial z}$ can be approximated as:

$$\frac{\partial A_{a,bent}(z)}{\partial z} \cong \frac{\partial A_{a,straight}(z)}{\partial z}e^{-j\mu\beta_{wg}\frac{\partial f_x(z)}{\partial z}}, \tag{A.23}$$

and, referring to Eq. A.22, $\frac{\partial A_{b,bent}(z)}{\partial z}$ can also be approximated as:

$$\frac{\partial A_{b,bent}(z)}{\partial z} \cong \frac{\partial A_{b,straight}(z)}{\partial z}e^{+j\mu\beta_{wg}\frac{\partial f_x(z)}{\partial z}}. \tag{A.24}$$

Then, substituting Eqs. A.5 and A.20 into Eq. A.23, $\frac{\partial A_{a,bent}(z)}{\partial z}$ becomes:

$$\frac{\partial A_{a,bent}(z)}{\partial z} \cong -j\frac{\Delta\beta_{straight}}{2}A_{b,straight}(z)e^{-j\mu\beta_{wg}\frac{\partial f_x(z)}{\partial z}} = -j\frac{\left[\Delta\beta_{straight}e^{-2j\mu\beta_{wg}\frac{\partial f_x(z)}{\partial z}}\right]}{2}A_{b,bent}(z), \tag{A.25}$$

and, substituting Eqs. A.6 and A.19 into Eq. A.24, $\frac{\partial A_{b,bent}(z)}{\partial z}$ becomes:

$$\frac{\partial A_{b,bent}(z)}{\partial z} \cong -j\frac{\Delta\beta_{straight}}{2}A_{a,straight}(z)e^{+j\mu\beta_{wg}\frac{\partial f_x(z)}{\partial z}} = -j\frac{\left[\Delta\beta_{straight}e^{+2j\mu\beta_{wg}\frac{\partial f_x(z)}{\partial z}}\right]}{2}A_{a,bent}(z). \tag{A.26}$$

Hence, referring to Eqs. A.25 and A.26, I can find the complex z-dependent $\Delta\beta$ of the bent DC, $\Delta\tilde{\beta}_{bent}(z)$, as:

$$\Delta\tilde{\beta}_{bent}(z) = \Delta\beta_{straight}e^{-j2\mu\beta_{wg}\frac{\partial f_x(z)}{\partial z}} = \Delta\beta_{straight}e^{j\frac{2\pi A(W+G)}{\Lambda}\beta_{wg}\sin(\frac{2\pi}{\Lambda}z)}. \tag{A.27}$$

Subsequently, calculating a running average of $\Delta\tilde{\beta}_{bent}(z)$ over one Λ along the z-axis according to Ref. [63], the effective $\Delta\beta$ of the bent DC, $\Delta\beta_{bent}$, can be estimated as:

$$\Delta\beta_{bent} \cong \frac{1}{\Lambda}\int_0^\Lambda \Delta\tilde{\beta}_{bent}(z)dz = \Delta\beta_{straight}J_0\left[\frac{2\pi A(W+G)}{\Lambda}\beta_{wg}\right], \tag{A.28}$$

where J_0 is the Bessel function of the first kind of order 0 (see Fig. A.11). I will use Eq. A.28 to design and analyze sinusoidal AC symmetric strip waveguide pairs and a PBS using a symmetric DC with sinusoidal bends.

Appendix B

Additional Publications

I am one of the co-authors of the following publications:

1. Han Yun, Yun Wang, Fan Zhang, Zeqin Lu, Stephen Lin, Lukas Chrostowski, and Nicolas A. F. Jaeger. Broadband 2×2 adiabatic 3 dB coupler using silicon-on-insulator sub-wavelength grating waveguides. Optics Letters, 41(13):3041-3044, 2016.

2. Matthew J. Collins, Fan Zhang, Richard J. Bojko, Lukas Chrostowski, and Mikael C. Rechtsman. Integrated optical Dirac physics via inversion symmetry breaking. Physical Review A, 94(6):063827, 2016.

3. Hamed Pishvai Bazargani, Maurizio Burla, Zhitian Chen, Fan Zhang, Lukas Chrostowski, and José Azaña. Long-duration optical pulse shaping and complex coding on SOI. IEEE Photonics Journal, 8(4):1-7, 2016.

4. Yun Wang, Zeqin Lu, Minglei Ma, Han Yun, Fan Zhang, Nicolas A. F. Jaeger, and Lukas Chrostowski. Compact broadband directional couplers using subwavelength gratings. IEEE Photonics Journal, 8(3):1-8, 2016.

5. Matthew Collins, Jack Zhang, Richard J. Bojko, Lukas Chrostowski, and Mikael C. Rechtsman. Dirac physics in silicon via photonic boron nitride. In CLEO: QELS-Fundamental Science, pages FM3A.4. Optical Society of America, 2016.

6. Zeqin Lu, Yun Wang, Fan Zhang, Nicolas A. F. Jaeger, and Lukas Chrostowski. Wideband silicon photonic polarization beamsplitter based on

point-symmetric cascaded broadband couplers. Optics Express, 23(23):29413-29422, 2015.

7. Zhitian Chen, Jonas Flueckiger, Xu Wang, Fan Zhang, Han Yun, Zeqin Lu, Michael Caverley, Yun Wang, Nicolas A. F. Jaeger, and Lukas Chrostowski. Spiral Bragg grating waveguides for TM mode silicon photonics. Optics Express, 23(19):25295-25307, 2015.

8. Zeqin Lu, Han Yun, Yun Wang, Zhitian Chen, Fan Zhang, Nicolas A. F. Jaeger, and Lukas Chrostowski. Asymmetric-waveguide-assisted 3-dB broadband directional coupler. In CLEO: Science and Innovations, pages SM1I.8. Optical Society of America, 2015.

9. Yun Wang, Han Yun, Zeqin Lu, Richard J. Bojko, Fan Zhang, Michael Caverley, Nicolas A. F. Jaeger, and Lukas Chrostowski. Apodized focusing fully etched sub-wavelength grating couplers with ultra-low reflections. In CLEO: Science and Innovations, pages SM1I.6. Optical Society of America, 2015.

10. Zhitian Chen, Jonas Flueckiger, Xu Wang, Han Yun, Yun Wang, Zeqin Lu, Fan Zhang, Nicolas A. F. Jaeger, and Lukas Chrostowski. Bragg grating spiral strip waveguide filters for TM modes. In CLEO: Science and Innovations, pages SM3I.7. Optical Society of America, 2015.

11. Yun Wang, Han Yun, Zeqin Lu, Richard J. Bojko, Wei Shi, Xu Wang, Jonas Flueckiger, Fan Zhang, Michael Caverley, Nicolas A. F. Jaeger, and Lukas Chrostowski. Apodized focusing fully etched subwavelength grating couplers. IEEE Photonics Journal, 7(3):1-10, 2015.

12. Zeqin Lu, Han Yun, Yun Wang, Zhitian Chen, Fan Zhang, Nicolas A. F. Jaeger, and Lukas Chrostowski. Broadband silicon photonic directional coupler using asymmetric-waveguide based phase control. Optics Express, 23(3):3795-3808, 2015.